XRD Structural Assessment of Peridotitic Garnet with Anomalous REE Distribution

By

Kirk Campbell Ross

Thesis submitted in partial fulfilment
of the requirements for the degree of
Doctor of Philosophy (PhD) in Mineral Deposits
and Precambrian Geology

School of Graduate Studies
Laurentian University
Sudbury, Ontario

Abstract

This thesis explored, as its major aim, the crystallographic and compositional characteristics of a particular type of peridotitic garnet associated with kimberlite. This garnet has a highly sinusoidal rare-earth element (REE) pattern as its distinguishing feature. Before the main research question could be addressed, a technique had to be developed that enabled the rapid and straight-forward acquisition of a full profile digital X-ray diffractogram from a single sub-milligram crystal fragment. After extensive experimentation and testing, successful development and realization of a method that is capable of producing such data was achieved. The next step of this research project was to empirically investigate and assess the crystal lattice strain model (CLSM) of Blundy and Wood (1994). Careful analyses of the REE present in a suite of clinopyroxenes were compared to the crystal structure data given from the XRD technique outlined above. Clinopyroxene is particularly useful for such an assessment because the radius of the M2 site in this mineral is between the largest and smallest REE, making the distribution of REE particularly sensitive to variation of the M2 site, which in turn is a direct consequence of the overall pyroxene structure. Subsequent to illustrating that XRD data could be collected on such small material and the XRD data and structural data given from the CLSM correlate strongly, peridotitic garnets with sinusoidal REE patters were investigated. The conclusions drawn in the first two contributions – namely that it was possible to collect accurate and precise XRD data from sub-milligram specimens and that the crystal structure and REE distribution were directly related – were imperative for the deduction of conclusions in the final, major research question. The XRD analysis of many garnets with and without sinusoidal REE patterns showed the presence of a small amount of an additional phase in some of these garnets. While this phase (2 out of 3 peaks indexed as possibly orthorhombic perovskite) is not present in sufficient quantities to give rise to such a strong sinusoidal segment in the garnet REE pattern, it prompted the critical step forward in formulating a working hypothesis for the otherwise inexplicable REE patterns. Specifically, I posit that many of the sinusoidal garnets may originally have precipitated as a very high pressure phase (in the mantle transition zone or deeper) that subsequently underwent a subsolidus isochemical transformation to garnet. Possible original precursor mineralogy is a combination of two perovskites or a perovskite +

garnet assemblage. Theoretical calculation using experimental partition coefficients demonstrated that a mixture of Ca-perovskite (CaPv) and Mg-perovskite (MgPv) REE patterns in the approximate proportions of 10% CaPv and 90% MgPv produce a REE diagram that is strikingly similar to those observed in sinusoidal single phase garnet. It has been shown experimentally that with increasing depth in the mantle, garnet plus a progressively increasing CaPv component is the stable mineral assemblage. Initial precipitation of two perovskites or CaPv + garnet as cumulates from a deep magma ocean would preserve the REE distribution of these minerals. Subsequent exhumation of such an assemblage would result in the retrogressive subsolidus phase transformation to a mineral stable at conditions of T and P of the shallow mantle environment, i.e. garnet, while retaining the REE pattern of the initial precipitate mineral assemblage. While this working hypothesis will require many more tests, its proposal may have significant implications for the mantle structure.

Acknowledgements

First I would like to express my gratitude to my supervisor, Balz Kamber, for giving me the opportunity to undertake this PhD project and providing insight crucial for the logical connections reached herein. My co-supervisor, Andy McDonald, provided access to all XRD equipment and also provided valuable insight, particularly with respect to XRD experiments. My third committee member, Pedro Jugo, is thanked for reading and evaluating my thesis cover to cover. Other faculty members that deserve recognition include Doug Tinkham, Dan Kontak, Darrel Long and Elizabeth Turner.

Dr. Thomas Ulrich is thanked for not only demonstrating a “hands-on” introduction the LA equipment but also imparted a thorough understanding of the data reduction procedure and software. Dr. William Zhe is thanked for assisting with the acquisition of quality XRD data.

Additionally, I would like to thank Dave Crabtree and Sandra Clarke for helpful discussions and the acquisition and reduction of microprobe major element data. I had many useful discussions regarding trace element behavior with the entire chemical fingerprinting crew: Annette Gladu, Mike Babechuk, Geoff Baldwin, Joe Petrus. Jen deRocher, Gaelen McNamara, Nik T. and Claire Sommers and I engaged in many curious conversations. I would also like to acknowledge Sandra Wood for loving me and remaining beside me despite my insufferable behavior during the course of my PhD.

This thesis is dedicated to my loving parents.

TABLE OF CONTENTS

List of Figures

Chapter 1

Chapter 2

Chapter 3

List of Tables

Chapter 1
No tables

Chapter 2

Chapter 3

Electronic supplement to chapter 3

Chapter 3 appendix

Chapter 4

Chapter 4 appendix

Chapter 5

No tables

List of appendices

Chapter 1

1. Thesis Introduction

As the main constituents of rocks, and a significant supply of inorganic resources, minerals have a long tradition of being studied from a variety of angles. Defined as naturally occurring crystalline solids of known structure and chemistry, minerals and their crystallo-chemical properties have contributed fundamentally to our understanding of silicate Earth differentiation. Physical and chemical properties of mineral phases are important parameters used to estimate the structure and composition of the inaccessible, interior parts of the Earth. For example, mineral phase transformations are a key source of information regarding the seismic behaviour of the upper and lower mantle composition, their mineral assemblages, and the dynamics of material exchange between the principal mantle domains. Along with the study of mineral major element chemistry, which assists in naming and classifying minerals, the concentration of trace (<1 part in 10,000) elements, including the rare-earth elements (REE) can lead to significant advances in our understanding of the tectono-magmatic environment from which the minerals were derived.

The REE (lanthanides, Y, Sc, and Ga) are, for the most part, isovalent (3^{+}, with the exception of Eu^{2+}, giving rise to the well known Eu anomaly) and their geochemical behaviour varies systematically with ionic radius (e.g. Bau, 1995). The REE span a considerable range of ionic radius (La, 1.16 Å – Lu, 0.977 Å; Sc, 0.754 Å and Ga, 0.62 Å; Shannon, 1976) making these elements sensitive tracers of petrological processes and mechanisms that decouple isovalent ions. The most common process affecting the REE

during silicate Earth differentiation is the fractionation into minerals and melts during partial melting and fractional crystallization.

The original principles governing the distribution of substituent elements in minerals were formalized by V. M. Goldschmidt (1937) in what are commonly referred to as Goldschmidt's rules. Put briefly, the rules governing elemental substitution into minerals state: (1) The radius of the substituent cation must vary from that of the host cation by no more than 15%; (2) If electrical neutrality is maintained by coupled substitution, charge can differ by 1 charge unit. For example, Ca and Al can substitute for Na and Si in plagioclase. If ions differ in charge by more than 1 charge unit, substitution is significantly less; (3) The electrostatic nature of the bond between two atoms has an effect on REE substitution. The charge to radius ratio is a measure of the density of electrical charge on the surface of ions, and determines the strength of the electrostatic bond that will form. When different cations occupy a specific site in a crystal, the ion with higher ionic potential forms a stronger bond with surrounding anions (O in the case of silicates) and therefore undergoes preferential substitution; (4) When the competing ions have different electro-negativities and form bonds of different character, substitution may be limited even when the charge and radius criteria are satisfied. For example, Mg^{+} (ionic) and Cu^{+} (covalent/ metallic) show little substitution despite similar ionic radii (Mg 0.72 Å, Cu 0.73 Å). These "rules" have provided the foundation of modern geochemistry.

With regards to REE distribution in minerals, description of the mineral/melt distribution of element (i) is quantified as the distribution coefficient (D) of i (Di) given as: mineral concentration of i / melt concentration of i. The REE distribution in a mineral is conveniently presented graphically in a plot of LnD vs. atomic number (figure 1). In

cases where the LnD is unknown, the concentration of the REE in a mineral is divided (normalized) by that in the whole rocks from which the mineral was extracted. The resulting plot of empirical distribution coefficients is commonly referred to as a normalized REE pattern and provides valuable information regarding the substitution of trace elements in general into a particular mineral.

The research behind the present thesis was conducted with the aim of better understanding unusual and unexpected REE distribution patterns in mantle garnets. Figure 1a shows a rare-earth element (REE) pattern of a typical garnet with preferential incorporation of the heaviest REE (HREE, Tm – Lu) followed by a smooth, sub-parabolic decrease of apparent LnD's to a minimum at La. By contrast, figure 1b illustrates the unusual MREE enriched garnets that constitute the focus of this study. The REE pattern of these garnets shows a sinusoidal shape with a positive slope among the light REE (LREE, La – Sm) to an apex around Nd followed by negative slope in middle REEs (MREE, Eu – Er) to a trough around Er. At Er, the LnD's for the HREE begin to increase very strongly, giving rise to a very steep positive slope for Tm, Yb and Lu.

The unusual incorporation of MREE into some mantle garnet has been known for decades. Richardson et al. (1984) were the first to infer relative enrichment of the MREE into peridotitic garnets sampled by kimberlite because of unradiogenic Nd isotope ratios, which run contrary to the expectations for a high time-integrated Sm/Nd ratio. Shimizu and Richardson (1987) were the first to report direct observations of such MREE enriched garnets. They performed a secondary ion mass spectrometry (SIMS) study of peridotite suite garnets found in the Finsch, Kimberly and Bultfontein kimberlite pipes in Siberia and southern Africa. Since this initial discovery, many other researcher have

noted this unique REE distribution in a portion of peridotitic garnets associated with kimberlites (e.g. Nixon et al., 1987; Hoal et al., 1994; Griffin et al., 1999; Stachel et al., 2004).

The most widely published explanation of these unusual garnet REE patterns is that their source rocks interacted with metasomatic fluids/melts in the deep mantle (Stachel et al., 1998; Griffin et al., 1999; Wang et al., 2000; Burgess and Harte, 2004). These fluids/melts are inferred to have left a "metasomatic overprint" giving rise to the sinusoidal garnet REE pattern. However, to the best of the author's knowledge, the unusual garnet REE patterns haven never before attempted to be rationalized by the crystal lattice strain model (CLSM) and first-principle mantle dynamics.

1.1. The crystal lattice strain model (CLSM)

The discovery of the CLSM arose from the pioneering empirical observations by Nagasawa (1966) and Onuma et al. (1968). The latter measured selected REE concentrations of othopyroxene (opx), clinopyroxene (cpx) and the alkaline basalt lava from which they were extracted as phenocrysts in the hope of representing equilibrium crystallization. Nagasawa, Onuma and co-workers noted that when the REE effective ionic radius is plotted against the natural logarithm (Ln) of D, a smooth concave downward near-parabolic pattern emerged. This pattern was considered by Onuma et al. (1968) to be an artefact of the crystal structure of the mineral. Figure 2a shows what is commonly referred to as an Onuma diagram. The downward sloping limbs either side of the apex represent the propensity of a single lattice site to incorporate misfit REE while the apex represents a fictitious cation of ideal radius (Ro) such that it has strain-free

admittance into the lattice site and therefore the maximum D (Do). Thus, isovalent cations both larger and smaller than Ro will invariably have Ds less than Do.

The curvature of the Onuma diagram was first parameterized by Nagasawa (1966) and later by Brice (1975), who formalized the curve as a thermodynamic variable derived from the difference in radius between the lattice site (Ro) and the radius of the substituent cation (Ri). Termed as the radius parameter, it increases in positive value with deviation of Ri from Ro, regardless of whether the substituent cation is larger or smaller than Ro. The radius parameter is defined as:

Equation 1 $\quad$ Radius Parameter (RP) $= Ro/2 \times (Ri - Ro)^2 + 1/3 \times (Ri - Ro)^3$

In an ideal example, where trace element incorporation was in equilibrium and where only substitution into one crystallographic site is dominant, a least squares regression of Ro for a line of best fit between the radius parameter and LnD, will yield a straight line with a negative slope. This plot (shown in figure 2b) is here informally referred to as a Brice diagram, and illustrates how Ro can be derived empirically for a lattice site from the measured trace element concentrations. The slope in the diagram on figure 2b is directly related to the tightness of the limbs of the Onuma curve in figure 2a such that with increasing stiffness (rigidity) of the lattice site the limbs on the Onuma curve become tighter, which is reflected by an increase in slope in figure 2b. The y-intercept in the Brice diagram corresponds to the apex of the Onuma parabola and represents LnDo.

The Onuma diagram for the represented garnet suggests that the ideal radius for substitution is ca. 0.88 Å. A best-fit iterative solution to the Brice diagram confirms this

visual estimate with a more quantitative number of 0.877 Å ±0.001 Å. The crystallographic rationale for this finding can be understood when inspecting an illustration of the $X_3^{XII}Y_2^{VI}Z_3^{IV}O_{12}$ garnet structure (where Roman numerals indicate number of coordinating O). A view along [100] is shown in Figure 2c. The 12-coordinated dodecahedral X-site is typically occupied by Ca, Mg, Fe or Mn, which in turn provide the nomenclature for most rock-forming garnets (i.e. grossular, pyrope, almandine and spessartine respectively). For clarity, only a single X-site polyhedron is shown in figure 2c (light grey), while the remaining X-site cations are drawn as spheres. X-ray absorption fine-structure spectroscopy (XAFS) has independently confirmed that the REE substitute into the X-site in the garnet structure, rather than in ill-defined lattice defects or interstices (Quartieri et al., 2002). The 6-coordinated octahedral Y-site (intermediate grey) and 4-coordinated tetrahedral Z-site (dark grey) are typically occupied by Al and Si, respectively, in rock forming garnets and are too small to accommodate the REE.

Expanding on the radius parameter formalization of Brice (1975), Blundy and Wood (1994) incorporated P, T, and elastic modulus of the lattice site into which the trace cations substitute to provide an equation (the basis of the CLSM) that predicts the trace element distribution in a mineral. Since its first publication, the Blundy and Wood (1994) equation (equation 2) has been successfully applied to many empirical and experimental datasets, for example for plagioclase (e.g. Hattori and Sato, (1996); Bindeman et al., (1998)), cpx (e.g. Fedelle and Zanetti, (2009); Hill et al., (2000); Hill et al., (2011)) and garnet (e.g. van Westrenen et al., (1999); van Westrenen et al., (2001); van Westrenen and Draper, (2007)).

$$D_i = D_{0(\mathrm{M})}^{n+} \times \exp\left\{\frac{-4\pi \mathrm{N_A} \mathrm{E_M^{n+}}\left[\frac{1}{2} r_{0(\mathrm{M})}^{n+}\left(r_i - r_{0(\mathrm{M})}^{n+}\right)^2 + \frac{1}{3}\left(r_i - r_{0(\mathrm{M})}^{n+}\right)^3\right]}{\mathrm{R}T}\right\}$$

Equation 2

Where D_i is the predicted D for element i, $D_0^{n+}{}_{(M)}$ is the maximum D in lattice site M for an element of charge n+, $E^{n+}{}_{(M)}$ is the elastic response of site M as given by Young's modulus. N_A is Avogadro's number, T is temperature in K and R is the universal gas constant (8.3123×10^{23} GPaÅ^{3}mol^{-1}).

Of particular relevance to this study are the experimental investigations regarding REE incorporation into garnet. The utility of the Blundy and Wood formalization becomes apparent when the D's for a set of isovalent trace cations in a mineral are measured and fitted with equation 2, which is then solved for P (E) and T. Thus, the CLSM given in equation 2 can be employed to reveal important information regarding to the PT conditions at the time of formation. For experimental and most natural garnets the CLSM functions very well at predicting the observed trace element D's. Indeed, such a strong relationship between crystallography, major element chemistry and Ro was observed that attempts have been made to predict Ro solely based on major element chemistry (van Westrenen and Draper, 2007). There remains, however, the one group of naturally occurring garnets, those with sinusoidal REE patterns, whose REE incorporation is widely divergent from that predicted by the CLSM.

Figure 3 shows an Onuma diagram for such a garnet compared with an experimental garnet that displays the expected REE pattern. The majority of sinusoidal garnets is associated with kimberlite deposits and is found either as inclusions in diamonds or in

heavy mineral concentrates that form above weathered kimberlite or man-made, processed concentrates. As noted above, ever since the original discovery of sinusoidal garnets by Shimizu and Richardson (1987) partial equilibration with, or metasomatic alteration by mantle fluids/melts has been invoked to explain the sinusoidal REE patterns (Stachel et al., 1998; Griffin et al., 1999; Wang et al., 2000; Burgess and Harte, 2004). For example, Stachel and co-workers suggest these garnets develop a sinuous REE pattern as a result of a three stage process. First, the mantle source is melted and depleted in the more incompatible LREE, leaving the garnets with a steep, HREE-enriched REE pattern. Next, the mantle source experienced metasomatic re-enrichment by a highly fractionated incompatible-element enriched fluid/melt (i.e. La/Lu >> 1), such as carbonatite or another type of alkaline melt. The garnet at this intermediate stage would then have had a U-shaped REE pattern, being most enriched in the HREE but also re-enriched in the LREE and MREE. The final sinusoidal garnet REE pattern is obtained by maturing the garnet and allowing the MREE to preferentially diffuse into the garnet, while LREE were being lost. However, the experimental diffusion studies of van Orman et al. (2002) and Tirone et al. (2005) have shown that the diffusivity of REE in garnet are in no way related to the DREE and that differences among the REE diffusivities in garnet are quite imperceptible.

The state of the art at the outset of the research performed for this thesis was thus that there was no convincing explanation for the sinusoidal REE patterns in these mantle garnets. It was hypothesized that the CLSM could provide a useful instrument to inspect these garnets. In most petrological and experimental dataset, the CLSM effectively predicts the relative REE distribution in a mineral based solely on its crystallography.

1.2. Mantle dynamics

Until the pioneering work of A.E. (Ted) Ringwood, most geologists considered olivine and pyroxene, minerals that are stable at the Earth's surface, to be of sufficient density to constitute the majority of the bulk silicate Earth (BSE, i.e. non-iron/nickel core), and that phase transformations with depth were unlikely. Inspired by the visionary work of Birch (1952), who suggested that the recently observed variations in seismic velocity within the Earth's mantle could not be solely due to compression of a homogenous material, but rather, were likely the result of phase-transition of olivine and pyroxene to material of increased density thereby increasing the seismic conductivity, Ringwood, under the supervision of Birch, proceeded to develop a device capable of achieving pressures never before attained from an experimental apparatus. With experimental equipment capable of 150,000 atm (roughly 15 GPa), they not only realized the olivine – spinel transition, but many other important pressure (P), temperature (T), and compositionally dependent phase transitions in the Earth's mantle. Combined with seismic data, the experimental mantle petrology data of Ringwood (e.g. Ringwood, 1956; Ringwood, 1959; Ringwood and Liu, 1975) has provided the basis for the understanding of the internal structure of the Earth.

Comprised of three concentric spheres, the Earth is composed of an outer thin brittle silicate crust (5-75 km thick) underlain by the mantle (2800 km thick) followed by a core, approximately 3,500 km in diameter. Seismic data show that the mantle constitutes the majority of the BSE and is divided into an upper mantle extending to depth of about 440 km followed by a zone of mineralogical transition extending from 440 to 660 km depth underlain by a lower mantle extending from 660 km to the core-mantle boundary. The high-pressure phase transformations that take place throughout the transition zone are key

to this thesis. In particular, minerals stable at the upper boundary of the transition zone (i.e. garnet) undergo solid state phase transformation to phases stable at higher pressures (i.e. perovskite).

Recent high pressure experiments on Ca- (Greaux at al., 2011) and Mg-rich garnets (Irifune et al., 1996; Oguri et al., 2000; Wood, 2000) show that at pressures corresponding to the transition zone and uppermost lower mantle, garnet progressively ex solves a cubic Ca-rich perovskitic phase (CaPv) followed by CaPv with orthorhombic Mg perovskite (MgPv) ± stishovite. These data imply that garnet can undergo an isochemical transformation to perovskite without developing a majoritic component (i.e. a garnet with > 3 Si atoms per formula unit). The important detail is that in a normal peridotitic bulk composition, garnet become more majoritic with increasing pressure. However, if the bulk composition of the transition zone is not peridotitic, but dominated by garnet, it is apparently possible to react the cubic Ca-rich perovskitic phase and orthorhombic Mg perovskite to garnet and vice versa. Significantly, the experiments of Oguri et al. (2000) show that these transformations are not restricted to pure end-members. These authors used natural garnet ($(Mg_{0.733}\ Fe_{0.173}\ Ca_{0.110}\ Mn_{0.004})_3(Al_{0.924}\ Cr_{0.030}\ Ti_{0.015})_2\ Si_{3.011}\ O_{12}$) not dissimilar in composition to those studied here and showed complete regressive transformation from the high pressure and temperature phases back to garnet. This latest insight from high pressure experiments opens a new dimension for explaining sinusoidal garnet REE patterns from very deep mantle sources, such as might be sampled by kimberlite. The key hypothesis derived in this thesis is that many of the sinusoidal garnets originally precipitated as a garnet + perovskite or 2 perovskite (CaPv + MgPv)

assemblage. Upon exhumation to a lower P – T regime, such assemblages retrogressively transformed to the single phase garnets observed today.

1.3. Analytical developments

Investigation of both trace element concentrations and structural characteristics required novel approaches pushing existing analytical techniques (e.g. solution and LA-ICPMS and XRD) to the edges of detection. As an example, with respect to in situ trace element analysis, LA –ICPMS analysis was conducted on a duel volume cell Resonetics EXIMER laser described in chapter 3. Trace element traverses were conducted with only a 5 μm laser beam diameter. To facilitate detection and improve counting statistics, only isotopes of those elements among the REE with a positive Otto-Harkins effect (i.e. even atomic number) were measured. XRD experiments were enhanced by using an image plate (IP) with increased sensitivity and by evacuating the camera cylinder. For the interpretation of 2-dimensional curved IP diffraction data, a new software package was developed to enable fast and precise data reduction. Developed in-house, the DIIS software package is fully described in the appendix of chapter 2.

1.4. Thesis layout

The thesis is comprised of three manuscripts (chapters 2, 3, and 4) that by the time of defence will be submitted to peer reviewed scientific journals. Following from this present introductory Chapter (1), Chapter (2) presents **An empirical assessment of the accuracy and precision of 2D Debye-Scherrer-type data collapsed into a 1D diffractogram.** This chapter is a manuscript that provides a systematic assessment of errors introduced throughout the reduction procedure and impact of such errors on the output diffractogram. Supplementary data for this paper includes: a copy of the DIIS

software, a copy of the Si diffraction pattern (10-070) given from SRM640c and a copy of the Al_2O_3 SRM676a, which are d-spacing and intensity standards respectively. Following from this critical test of accuracy and precision, on which the entire thesis hinges, Chapter (3) presents: **An empirical test of the crystal lattice strain model for rare-earth element partitioning into clinopyroxene.** This chapter is also a manuscript, which outlines a direct correlation between the mean M-O bond length given from the XRD technique outlined above and that given from the CLSM and provides additional evidence for crystallographic control of trace element concentrations in minerals. Supplementary data for this manuscript includes a petrologic description of each locality from which the grains studied were derived. To the author's knowledge, this is the first comprehensive empirical test of the CLSM on clinopyroxene (cpx) that combines crystallographic and geochemical data from the very same mineral grains. After successful empirical verification of the CLSM, Chapter (4) documents the attempt of rationalizing the sinusoidal REE patterns: **Sinusoidal REE patterns in peridotitic garnets explained using the lattice strain model.** The chapter is also presented in manuscript form and involves a detailed crystal structure and trace element analysis of garnet grains that exhibit a sinusoidal REE pattern. It provides an alternative rationale to metasomatic alteration for these patterns. It is important to note that the manuscripts presented herein have been submitted to different journals and therefore are formatted slightly differently from one another. Supplementary data for this manuscript includes trace element maps of the surface of a sinusoidal garnet. The final Chapter (5) contains a summary and outlook.

1.5. Contributions

Chapter (2): The PhD candidate performed all experiments and data reduction for the study presented in this chapter. J.A. Petrus wrote the software used in the data reduction. Andy McDonald provided valuable input regarding the software functionality requirements in addition to providing access to the necessary XRD generation and experiment equipment.

Chapter (3): The PhD candidate performed all LA-ICPMS experiments under the watchful eye of Dr. Thomas Ulrich in addition to acquiring and interpreting all XRD data. Balz Kamber provided valuable insight and performed the solution ICPMS measurements on the exceedingly small mineral fragments. The third author provided access to all XRD generation and experimental equipment in addition to advising on the finer details of single crystal refinement.

Chapter (4): The PhD candidate collected, processed, and interpreted all LA-ICPMS and XRD data presented. He was also responsible for formulating the hypothesis that the studied garnets might have originated as multi-phase (perovskite-bearing) assemblages. Balz Kamber conducted the hydrofluoric acid leaching experiments and first formulated the (unconfirmed) hypothesis that the garnet might contain MREE-rich inclusions. Andy McDonald provided valuable revisions to the manuscript in addition to access to XRD generation and experimental equipment.

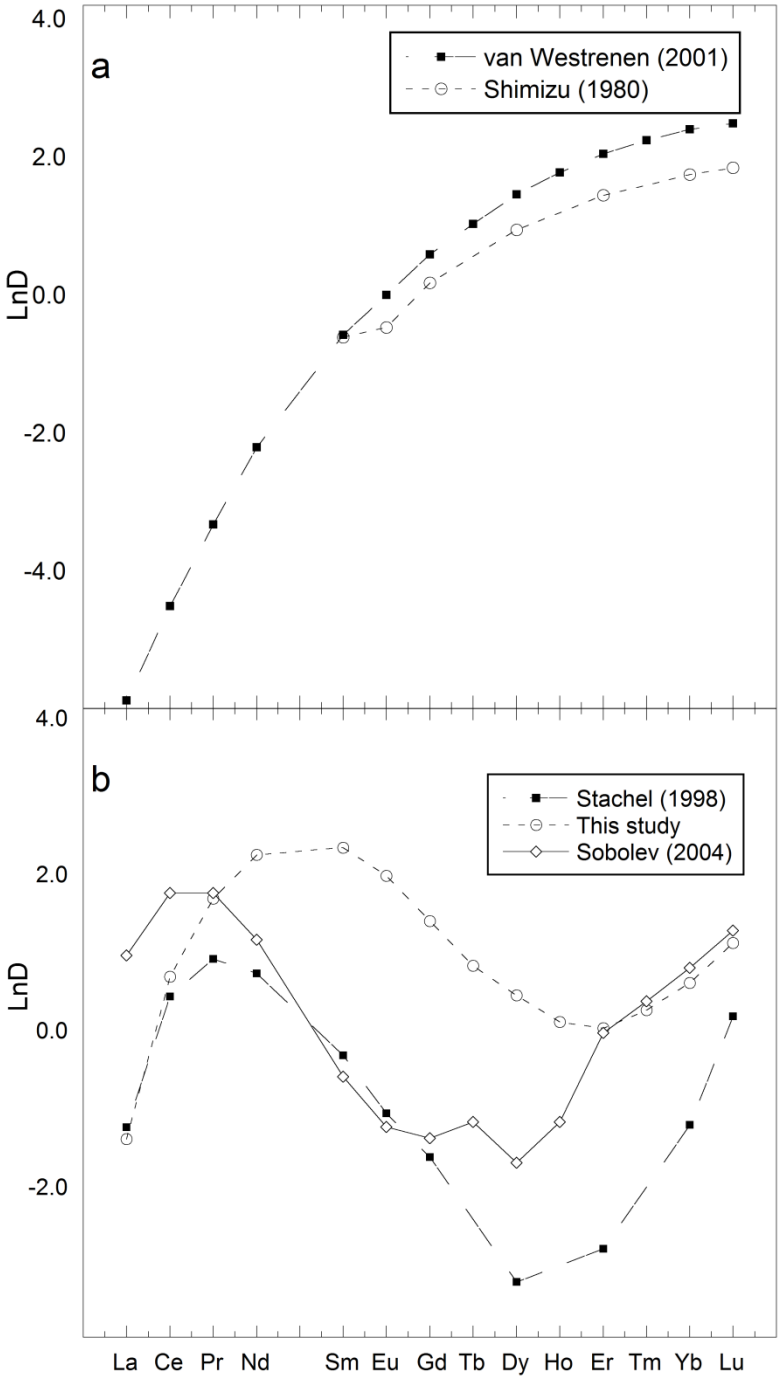

Figure 1 shows two plots of LnD vs. atomic number. Panel A shows literature data for natural and experimentally produced garnets with a normal REE pattern. Panel B shows sinusoidal garnets from this study and the literature. LnD was calculated by normalizing the concentration by CI carbonaceous chondrite (McDonough and Sun, 1995)

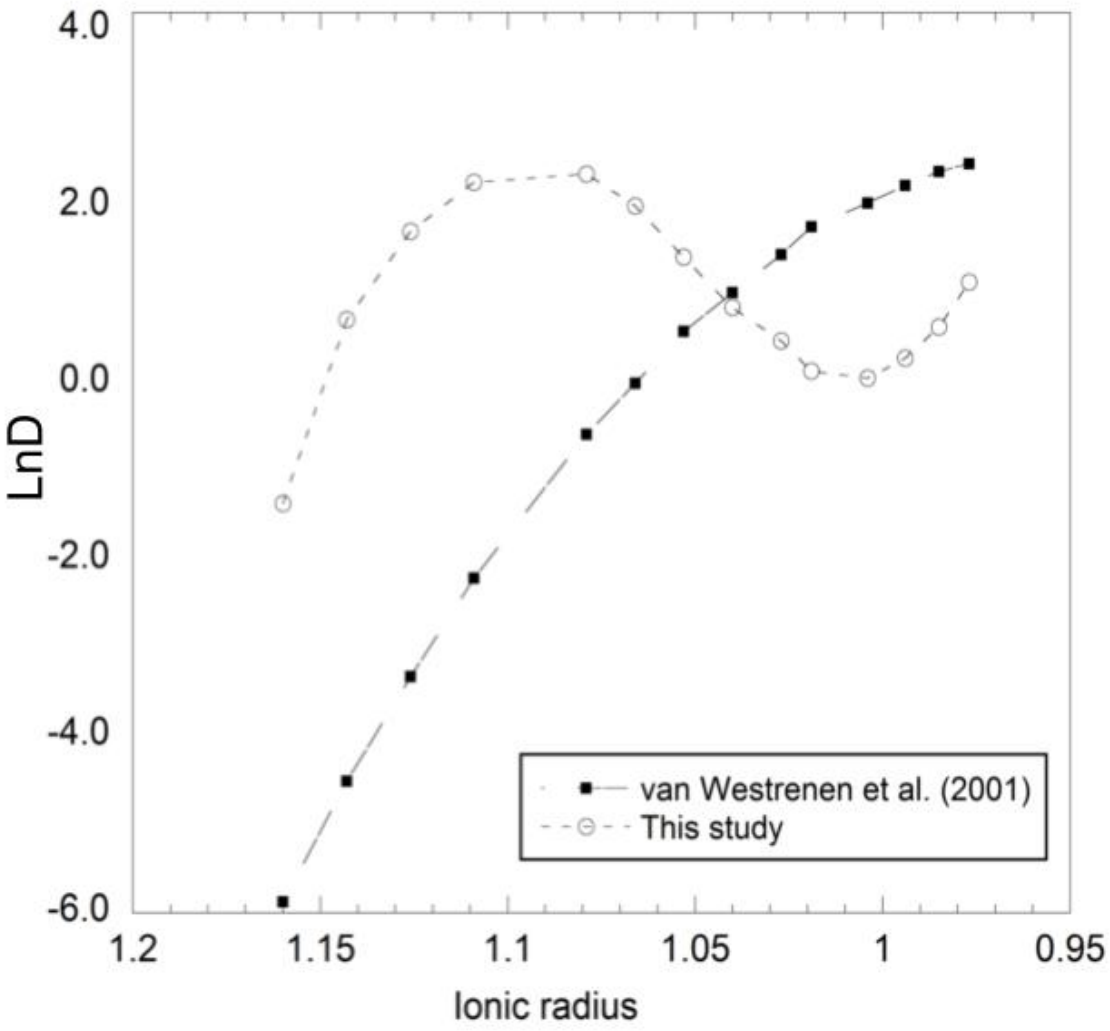

Figure 2 shows Onuma diagrams for a normal garnet (solid squares) and a sinusoidal garnet (open circles). Note that in the normal garnet the HREE tend to flatten out while in the sinusoidal garnet they show a steep positive slope.

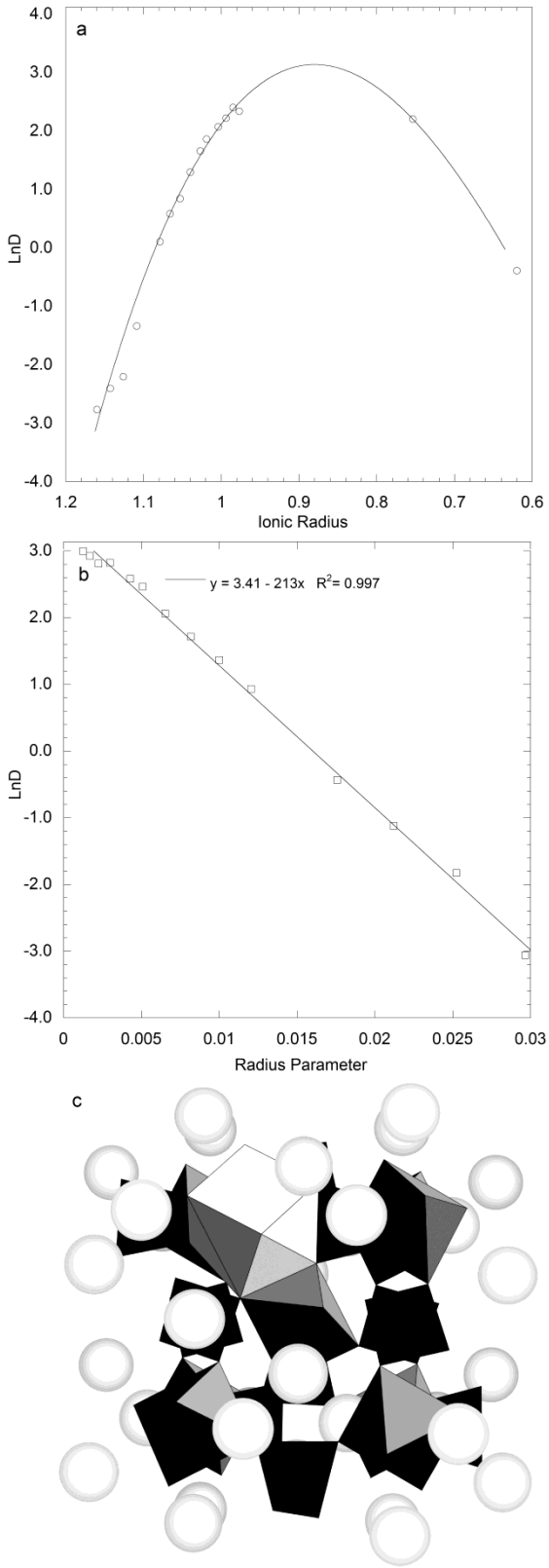

Figure 3: Panel a shows an Onuma diagram for a normal garnet. Not until Sc (0.745 Å) and Ga (0.62 Å) are included does the appearance of an Onuma diagram become apparent.

3b shows a Brice diagram for the same garnet as in 2a. Note LnD for trace cations either side of the apex in 3a fall on the same line in 3b

3c shows the garnet structure and the lattice site on which REE substitute, (X-site, a single polyhedral is shown in upper left).

Chapter 2

An empirical assessment of the accuracy and precision of 2D Debye-Scherrer-type data collapsed into a 1D diffractogram

Kirk C. Ross[a]* Joseph A. Petrus[a] Andrew M. M[c]Donald[a]

[a]Earth Sciences, Sudbury, Ontario, P3B3C6, Canada

Correspondence email: kross@laurentian.ca

Keywords: X-ray diffraction; Gandolfi; image-plate; integration; standard;

Abstract:

X-ray diffraction has been routinely employed in the Earth sciences to characterize the crystallography of rocks and minerals. Routine characterization of samples too small for analysis by classic automated powder diffraction methods becomes challenging without access to single crystal or micro-diffraction equipment. Here, we show that a traditional Gandolfi camera lined with an image plate as the detection medium can return a fully quantitative diffraction pattern from a sub-milligram single grain specimen in a simple and straightforward manner. Peak positions (d-spacing) were assessed using certified values of Standard Reference Material (SRM) 640c Si powder while intensity data were compared to the certified values for SRM676a alumina powder. The refined unit cell dimension of Si powder differed from the certified value of 5.4312 Å by no more than 0.0007 Å with a standard deviation (1σ) of 0.0005 Å for three experiments. For intensity, the σ and disparity from certified values of triplicate experiments on SRM676a were both less than 2%. Comparison of crystallographic parameters for a naturally occurring garnet and cpx given from refinement of single crystal diffraction data and data produced by the

Gandolfi-IP method outlined herein shows that both accurate and precise XRD data can be produced in a timely and cost effective manner using only an IP, Gandolfi camera and software freely available on the internet.

1. Introduction

X-ray diffraction (XRD) has long been one of the most important tools used for the identification and analysis of minerals (Buerger, 1946; Bloss, 1971). For samples greater than roughly 1 g, the automated powder diffractometer has been the principal instrument used for XRD data collection. These data can be applied not only for routine phase identifications but, when combined with powerful peak-deconvolution approaches (e.g., the Rietveld method; Rietveld, 1969), they are also capable of revealing detailed crystal-structure information, including related crystal symmetry, unit-cell dimensions, fractional coordinates, thermal-displacement factors, etc. (Young and Wiles, 1991). In situations where far less material is available for analysis (e.g., < 0.1 g), XRD studies have relied upon powder X-ray diffraction (PXRD) cameras, including those employing the geometry of a Debye-Scherrer camera (DS) with a single-axis and Gandolfi camera with two-axes of rotation. Cameras with such a design routinely employed direct-exposure film (DEF) as the recording medium. Use of these cameras has however declined recently owing to the discontinued manufacture of DEF. This combined with the need for chemicals and space to process and store diffraction data obtained has made prolonged use of a DEF X-ray detection system inefficient and impractical. Since traditional PXRD cameras are primarily restricted by the DEF recording medium, a great deal of research has gone into developing alternative technologies. One such technology is photo-stimulable phosphor, allowing reusable image plates (IP) to replace DEF (Lee et al.,

2000; Gales and Bentley, 2004). Since the deployment of IP-technology into the X-ray diffraction community, a re-emergence of film-based techniques (e.g. Norby, 1997; Zhukhlistov et al., 2004) is beginning to become apparent.

Two procedures are used to convert a 2D diffraction image collected on a curved IP into a 1D digital diffractogram. While both consist of the summation and normalization of pixel intensities (referred to herein as integration) they differ greatly in integration geometry. Of these two integration types, one method consists of orthogonal integration (OI) which provides the normalized intensity of pixels strictly orthogonal to the central mirror plane of the diffraction image (parallel to the length of the IP). The second integration type consists of the integration of pixels coincident with the 2θ dependant curvature of the Debye ring on the diffraction image.

Several software packages exist in the literature and are available for download from the internet that collapse a 2D image into a 1D diffactogram via the two integration methods described above. Orthogonal integration is championed by an image reduction procedure outlined by Barwood (1997) which uses the public domain software Image J. Similar to Image J is MAUD (Lutterotti, 1996) which uses an Image J based integration routine. However, orthogonal integration disregards the 2θ-dependent curvature of the Debye-ring. Thus, masking an area wider than 1 or 2 mm along central mirror plane of the image results in a 2θ-dependant asymmetric peak-shape from the inclusion of pixels on the "tails" of the Debye ring that do not strictly correspond to the diffraction angle to which they are attributed. Nonetheless, OI methods have proven very successful for the experiments of Norby (1997) who used a 3 mm-wide mask on the flat-plate diffraction data of α-quartz, given the implementation of proper corrections for the non-linear nature

of the FWHM, step-size and zero correction. In DS-type geometry, at low (< 60) or high (> 120) angles 2θ the radius of the Debye-ring is reduced to such an extent that the pixels tangential to the Debye-ring along the central mirror plane of the image that truly represent the peak position are significantly reduced in number. Such a reduction in contributing pixels increases the influence of single crystal diffraction spots, scratches, blemishes or discontinuous diffraction lines and will severely affect the quality of the output diffractogram given from the OI method. While a plethora of software for the conversion of flat plate diffraction data is available to perform a least-squares full-profile structural refinement, (e.g. Datasqueeze, Two2One (Vogel et al., 2007), Powder3D IP (Rajiv et al., 2007), XRD2DScan (Rodriguez-Navarro, 2006) DIIS (Petrus et al., 2010) and the popular Fit2D (Hammersley, 1996),) only DIIS – a relatively new package presented in Petrus et al. (2010), and XRD2DScan are capable of a fully quantitative 2θ-dependent integration of curved image-plate (CIP) diffraction data.

The primary thrust of the present contribution is to discuss the accuracy and precision of collapsing 2D curved IP diffraction data into a 1D digital diffractogram suitable for Rietveld structural refinement. We used the DIIS program (Petrus et al., 2010) to convert diffraction data given from standard reference materials (SRM) 640c and 676a in addition to XRD data given from a clinopyroxene and garnet for which we had previously acquired single-crystal diffraction data. For the d-spacing and intensity standards (SRM640c and SRM676a respectively) we compared data given from the output diffractograms to the certified values. We then compared the crystallographic parameters obtained from refinement of single-crystal XRD (SXRD) and powder XRD (PXRD) data given from naturally occurring garnet and clinopyroxene (cpx).

2. Materials and Method

2.1. The IP and IP scanner

The experiments described herein were carried out using a FUJI BAS-SR 2400 imaging plate (SRIP) and scanned with a BAS 2500 scanner. The construct, dynamic quantum efficiency, dynamic range and principles upon which the image plate operates have been discussed in detail by Amemiya and Miyahara (1988), Amemiya (1995), Lee et al. (2000), Otto et al. (2001) among others. For a comprehensive review of current IP models and their point spread function within the photo-sensitive phosphor layer of the IP combined with the effects of different IP scanners see Bourgeois et al. (1994). The non-automated nature of the procedure outlined herein allows for the introduction of human error by misalignment of the IP in the camera of on the IP scanner. These effects are unavoidable and are

2.2. X-ray diffraction

Single-crystal XRD data were collected on a Bruker Apex II three-circle diffractometer operated at 50 kV and 30 mA using Mo Kα radiation (graphite filter) and a detector-to-sample distance of 5.95 cm. Diffraction data were collected with ω scans at different φ settings using the program SAINT (Bruker, 1999). An empirical absorption correction calculated using SADABS (Sheldrick, 1996) was applied.

Powder diffraction data were acquired with a Gandolfi camera of radius 114.6 mm mounted on a Phillips PW 1870 X-ray generator operating at 40 kV and 30 mA, employing Ni-filtered Cu $K\alpha_{avg}$ radiation (λ = 1.5418 Å). IPs were exposed for 4 to 6 hours. To reduce the scatter of X-rays caused by air (thus improving the measured peak-to-background ratio), the Gandolfi camera chamber was evacuated to an absolute

pressure of 4 kPa (i.e. 0.04 atm) via an Edwards 5 CFM rotary vein pump. The incident X-ray beam was collimated using either a 300 or 500 µm pin-hole collimator. The IP was placed in the Gandolfi camera in a Straumanis-type configuration, where the longitudinal ends of the IP meet approximately at the 12 o'clock position inside the camera cylinder.

The combination of an evacuated Gandolfi camera and highly sensitive IP presented an unexpected set of issues that needed to be considered and resolved. First, the medium used to position the material to be analyzed in the X-ray beam (a glass fibre) was itself to contribute diffraction lines at 1.62, 1.84 and 2.55 Å. This may seem surprising to many as these types of fibres have long been used by crystallographers to collect XRD crystallographic data; however, the phenomena of both the fibre and adhesive contributing to the diffraction pattern has been noted in several cases (e.g. Palmer, 1997; Matsuzaki and Shinoda, 2004). After extensive testing of assorted drawn glass, fibre optic cable, along with natural and synthetic brush fibres, none were found to be completely X-ray amorphous. This is likely due to the sensitivity of the IP which is further enhanced by the presence of an evacuated camera cylinder. In the end, glass fibres from a conservator's brush were found to contribute the fewest and weakest X-ray diffraction lines. These fibres are composed of silica glass and measure approximately 70 µm in diameter and are typically cut to ~0.5 cm in length. The crystal structure of the fibres is consistent with a hexagonal (P63mc) wurtzite (ZnS) corner linked tetrahedral structure. These particular fibres have a very high degree of consistency in terms of fibre shape and diameter enabling them to be drawn further under heat reducing the diameter to as little as ~15 µm. The pronounced reduction in mass of the drawn glass fibre present

in the incident X-ray beam reduces the presence of reflections arising from the fibre to the extent that they are virtually invisible in the output diffractogram.

During assessment of fibre material several different adhesive materials used to fasten the grain to the fibre were also investigated. All were found to produce a gradual, low-angle (~ 10-20 °2θ CuKα) elevated background that is typical of a genuinely X-ray amorphous material. In light of this, a quick drying (working time ~15 s), acetone-soluble, fingernail hardener was used. Five-minute epoxy was also tested and found to work well, providing for a longer working time (~5 min), although no dissolution material is currently known that is non-toxic to the user and non-destructive to the material being analyzed.

2.3. Integration and digitization of IP data

The mathematical rationale for 2θ-D integration and digitization of diffraction data collected with a CIP has been adequately described by O'Neil et al. (1993) as the intersection of a cone (of diffraction) with a cylinder (camera chamber). A succinct historical review of digitization and integration of CIP diffraction data has been given by Palmer (1997). Although the methodology has evolved with time, the fundamental objectives have remained unchanged; namely that the digitization procedure should maintain the spatial precision and resolution of the film or IP data. Since the grain size of the BaFBr: Eu^{2+} in the PSP layer of the IP is on the order of 10 μm, a potential step-size of 0.01 °2θ in a 114.6 mm radius camera is theoretically achievable. The BAS-2500 scanner used here, however, was capable of only 508 DPI giving a step-size of 0.05 °2θ or 50 μm image resolution. Currently, FUJI-film manufactures a BAS-5000 capable of 25 μm resolution or a 0.025 °2θ step-size in a 114.6 mm camera.

Gales and Bentley (2004) have shown that the dynamic range of the IP is linear over 5 orders of magnitude; far exceeding that of DEF (< 2 orders of magnitude). The wide dynamic range of the IP permits the detection of very weak diffraction lines simultaneously with the detection but non-saturation of very intense diffraction lines. Most IP scanners allow the user to choose between 8- or 16-bit colour depths. For a black and white image, an 8-bit image results in 2^8 (256) shades of grey digitizing a continuum of grey-scale shades into only black, white, and 254 discreet shades or intensity levels. A similar process takes place when scanning an image with 16-bit colour depth, except now the grey scale continuum is digitized into 2^{16} (65536) discreet shades resulting in a dramatic increase in intensity resolution.

2.4. Peak position, intensity and shape measurement

The accuracy and precision of position, intensity and shape for selected peaks given from integrated X-ray diffraction data were assessed using the software package X'pert Highscore Plus Version 3.0.5 (Panalytical 2012). The background for all patterns was determined and subtracted using a flat background setting plus a fifth-order polynomial routine given by Sonnerfeld and Visser (1975). To obtain d-spacing data, preliminary peak positions were first visually estimated and manually inserted, then refined using the pseudo-Voigt peak-fit routine available in X'Pert Highscore Plus.

To evaluate the accuracy of relative intensities (I/I_0), peak search parameters were restricted to a minimum significance of 80%, cycled until all calculated shifts were less than 0.5 times the estimated standard deviation, converging with an average peak-fit error of 2.8%. Overlapping $K\alpha_1$ - $K\alpha_2$ (resulting from the use of non-monochromatic X-ray radiation) peaks present below ~ 40 °2θ (Cu radiation) are not resolvable and as such,

corresponding intensities for diffraction peaks below this angle are considered to be weighted combinations (weight of 2/3: 1/3) of both these wavelengths. In light of this, the $K\alpha_2$ contributions were mathematically subtracted assuming a ratio of 2/3: 1/3 using the method of Ladeel et al. (1975).

Through Rietveld refinement, the pseudo-Voigt (pV) function was found to adequately describe peak shape. The pV function describes peaks as a mixture of the Lorentzian (L) and Gaussian (G) peak functions (e.g. Young and Wiles, 1982) given as:

$$pV = nL + (1 - n)\, G, \qquad (1)$$

Where n is a mixing parameter that describes the amount of Lorentzian component. Errors reported by the Highscore Plus software for the peak shape and position refinements were less than 0.00005 Å and are therefore not reported.

2.5. Materials analyzed

National institute of standards and technology (NIST) standard reference material SRM640c (Si) and SRM676a (Al_2O_3) were evaluated for line-positions and relative-intensities, respectively. These standards were chosen due to their well-established crystallographic properties, strongly diffracting character and absence of preferred orientation effects. Following assessment of the IP digitization of diffraction data given from SRM640c and 676a, we preformed diffraction analysis of a garnet and cpx mineral fragments for which we had previously acquired single crystal diffraction data. Both the garnet and cpx were derived from a heavy mineral concentrate used for kimberlite exploration.

3. Results and Discussion

3.1. NIST SRM640c

The Si standard, SRM640c, is cubic (space group Fd-3m) with Si as the one and only symmetrically unique atom (Kaiser, 2005). Since Si occupies the symmetrically constrained 8a Wyckoff special position (0.125, 0.125, 0.125), the unit-cell dimension is the only variable crystallographic parameter. Given that the chemistry and fractional atomic coordinates of SRM640c are fixed, variation in diffraction-peak positions must necessarily be a function of the unit-cell edge. To avoid such geometrically imposed crystallographic restriction of relative peak positions by the unit cell edge dimension, all peaks were individually located and refined with respect to position and shape according to the procedure outlined in section 2.4. Because the unit-cell edge for SRM640c is reported with femtometer precision at 5.431195(1) Å, well beyond the resolution of this technique (~ ±0.001 Å) all certified SRM640c peak positions have an effective error of zero. Consequently, the IP resolution is the limiting factor.

Table 1 shows the certified positions for the 11 peaks in SRM640c followed by the measured positions given from three experiments in Å. Comparison of the mean of three experiments to the certified values shows that the largest discrepancy is for the lowest angle (111) peak of only 0.0012 Å. This peak also shows the largest standard deviation (σ) similar in magnitude (0.0015 Å). With decreasing d-spacing the errors and σ decrease dramatically becoming significant in the 4^{th} decimal place only (i.e. error = 0.0004 Å or less, σ = 0.0005 or less) for a d-spacing on the order of 2 Å. For d-spacing smaller than 2 Å, the discrepancy and σ approach 0. Full profile refinement of three SRM640c IP experiments gave unit cell dimensions comparable to the certified value. One experiment (10-020) gave a unit cell dimension 0.0007 Å smaller than the certified value of 5.4312 Å

while the two remaining experiments gave unit cell dimensions that differ by no more than 0.0003 Å. Errors reported below the unit cell dimensions are those given by the refinement software for the unit cell.

Below the crystallographic parameters, table 1 also gives agreement and instrumentation parameters given from the refinements such as the *u*, *v*, and *w* Cagliotti parameters (Caglioti et al., 1958) and the peak shape parameter (*n*). According to equation 1, low values of *n* indicate a dominant Lorentzian component in the pV function describing the peak profile.

3.2. NIST SRM676a

Table 2 shows the intensities measured from three image plate runs of intensity SRM676a compared to values given for the seven certified peaks (excluding the 100% peak). For five of the seven peaks the σ among the three measurements is greater than the absolute difference between the measured and certified values, particularly when the error reposted by NIST is considered. Good reproducibility among the intensity measurements is particularly sensitive to the background subtraction routine used. For this reason, we used a consistent set background subtraction parameters applied to all measurements. Excellent reproducibility for intensity measurements is shown in table 2 by the small σ among individual experiments while adequate accuracy is shown by the small difference in relative intensity between the measured values and those certified by NIST (less than 2% relative intensity in both cases). Table 2 also shows the mean FWHM for all eight certified peaks for each experiment. Data from experiment 10-156 shows a slightly larger FWHM owing to the use of a larger 500 μm collimator. A consistent

FWHM for all measured peaks is indicated by the low σ of the FWHM measurements (less than 0.008% in all cases).

3.3. Natural specimens

To show the unique applicability of the IP digitization technique to produce a quality powder diffraction pattern from a single minute grain, a natural clinopyroxene and garnet. These grains were analyzed by single crystal diffraction analysis followed by the method considered herein. Tables 3 and 4 give a comparison between the refined SXRD and PXRD data.

3.3.1. Garnet

A specimen of garnet approximately 0.04 x 0.04 x 0.16 mm was measured by PXRD and SXRD techniques. Refinement of the PXRD data between 17-164 °2θ converged with an RBragg of 4.25%. There are 29 peaks greater than 5% relative intensity within the refined interval of an average FWHM of 0.35 °2θ (σ = 0.06). The Caglioti parameters along with *n* both indicate a strongly Lorentzian peak shape.

The SXRD data were collected using the apparatus outlined above in §2.2 over a period of approximately 4 hrs. yielding a total of 434 frames. The frames were integrated with the Bruker SAINT software package using a narrow-frame algorithm. The integration of the data using a cubic unit cell yielded a total of 2389 reflections to a maximum θ angle of 28.26° (0.75 Å resolution), of which 164 were independent (average redundancy 14.567, completeness = 100.0%, R_{int} = 1.84%, R_{sig} = 0.76%) and 150 (91.46%) were greater than $2\sigma(F^2)$.

The crystal symmetry of cubic garnet permits variation of only the unit cell and the fractional atomic coordinates of the O atom. Table 3 shows the crystallographic and agreement parameters given from the refinement of SXRD and PXRD data. The unit cell dimension differed by less than 0.005 Å while the *x*, *y*, and *z* coordinates of O gave a difference of -0.0008, 0.0000, and 0.0006 Å respectively. Although the atomic coordinates for the X-site (Ca, Mg, Fe), Y-site (Al and Cr) and Z-site (Si) are fixed in special positions, the thermal isotropic parameters (Biso) can still be refined. Shown in table 3, the Biso parameters given from refinement of the two XRD data sets are in good agreement. The significant zero-shift correction in the garnet refinement (0.0135 °2θ) is owing to the 50 μm resolution of the IP image (equal to a step-size of 0.05 °2θ), which, in a worst case scenario where the true pattern centre is displaced from the origin in the integration software by one half pixel, could require a zero-shift correction of 0.025 °2θ. Regardless, the refined garnet crystallographic parameters given from the SXRD and PXRD data are in good agreement.

3.3.2. Clinopyroxene

To compare data from a lower symmetry more complex phase, a natural chrome diopside (cpx) was analyzed by the SXRD and PXRD methods. The SXRD analysis yielded a total of 2110 frames over 35.17 hours. The frames were integrated with the Bruker SAINT software package using a narrow-frame algorithm. The integration of the data using a monoclinic unit cell yielded a total of 3447 reflections to a maximum θ angle of 31.82° (0.67 Å resolution), of which 706 were independent (average redundancy 4.882, completeness = 94.4%, R_{int} = 2.87%, R_{sig} = 3.26%) and 570 (80.74%) were greater than $2\sigma(F^2)$. The PXRD data were refined over the interval 25-165 °2θ which included 32

peaks above 5% intensity with a mean FWHM of 0.32 °2θ (σ = 0.004) and an *n* value of nearly 34% Gaussian. The greater Gaussian component gives peaks that are short and wide when compared to a Lorentzian distribution and is attributed to disordering among cations on the M1 and M2 site in the cpx. Table 4 compares the crystallographic parameters of the cpx obtained from the two refined XRD data sets. In general, the crystallographic parameters agree to within error. Notable exceptions include the unit-cell beta angle and the *z* coordinate of the three O atoms. The thermal parameters were refined both as a B overall (Bov, 0.75) and individually for each atom in the powder refinements (see table 4).

4. Conclusion

Presented here is a technique to acquire fully quantitative XRD data from a single minute grain using a Gandolfi camera, IP and integration software such as DIIS or XRD2DScan. Where there is insufficient material to analyze by powder diffractometer, this method can provide valuable crystallographic information such as unit cell dimensions, fractional atomic coordinates and in many cases, the Bov parameters. Analysis of d-spacing standard SRM640c in triplicate gave only 0.0005 Å standard deviation in the unit cell dimension with an accuracy of ± 0.0001 Å. Similarly, triplicate measurements of intensity standard SRM676a gave a standard deviation among three measurements of less than 2% relative intensity for any certified peak. With such promising results given from the analysis of these standards, we endeavoured to analyze minute natural single crystals of a high symmetry garnet (cubic, Ia-3d) and a lower symmetry cpx (monoclinic, C2/c) for which we had single crystal diffraction data as part of another study (Ross et al., 2012). Given in table 3 (garnet) and table 4 (cpx), the results from refinement of the two

XRD data sets agree very well. For garnet, not only did the unit cell dimension and fractional atomic coordinates for O agree very well but also the Biso parameters were similar. Likewise for cpx, the unit cell dimensions returned from the two methods compare well with the largest discrepancy in the *c* unit cell dimension of only 0.0007 Å and 0.02° in the beta angle. Although effective at retrieving crystallographic parameters from very small crystalline phases, this technique is also ideally suited for cursory phase identification and investigation into the presence any included material within the grain analyzed.

References

Amemiya Y (1995) Imaging plates for use with synchrotron-radiation. Journal of Synchrotron Radiation 2:13-21

Amemiya Y, Miyahara J (1988) Imaging plate illuminates many fields. Nature 336(6194):89-90 doi:10.1038/336089a0

Barwood HL (1997) Using NIH-Image to convert powder X-ray diffraction camera films to digital diffractograms. Geological Society of America Abstracts with program A-402

Bloss DF (1971) Crystallography and Crystal Chemistry. Mineralogical of America, Blacksburg Virginia

Bourgeois D, Moy JP, Svensson SO, Kvick A (1994) The Point-Spread Function of X-Ray Image-Intensifiers CCD-Camera and Imaging-Plate Systems in Crystallography - Assessment and Consequences for the Dynamic-Range. Journal of Applied Crystallography 27:868-877 doi:10.1107/s0021889894004048

Buerger MJ (1942) X-Ray Crystallography. John Wiley and Sons,

Caglioti G, Paoletti A, Ricci FP (1958) Choice of Collimators for a Crystal Spectrometer for Neutron Diffraction. Nuclear Instruments & Methods 3(4):223-228

Gales SG, Bentley CD (2004) Image plates as x-ray detectors in plasma physics experiments. Review of Scientific Instruments 75(10):4001-4003 doi:10.1063/1.1789256

Hammersley AP, Svensson SO, Hanfland M, Fitch AN, Hausermann D (1996) Two-dimensional detector software: From real detector to idealised image or two-theta scan. High Pressure Research 14(4-6):235-248 doi:10.1080/08957959608201408

Ladell J, Zagofsky A, Pearlman S (1975) Cu K-alpha-2 elimination algorithm. Journal of Applied Crystallography 8(OCT1):499-506

Lee SL, Windover D, Doxbeck M, Nielsen M, Kumar A, Lu TM (2000) Image plate X-ray diffraction and X-ray reflectivity characterization of protective coatings and thin films. Thin Solid Films 377:447-454 doi:10.1016/s0040-6090(00)01366-3

Lutterotti L, Gualtieri A, Aldrighetti S (1996) Rietveld refinement using Debye-Scherrer film techniques. In: Cernik RJ, Delhez R, Mittemeijer EJ (eds) European Powder Diffraction: Epdic Iv, Pts 1 and 2, vol 228. pp 29-34

Matsuzaki T, Shinoda K A method for digitizing the X-ray diraction pattern on X-ray film by gandolfi camera. Journal of Geosciences 47:1-8

Norby P (1997) Synchrotron powder diffraction using imaging plates: Crystal structure determination and Rietveld refinement. Journal of Applied Crystallography 30:21-30 doi:10.1107/s0021889896009995

Oneill B, Nguyen JH, Jeanloz R (1993) Rapid Computer-Analysis Of X-Ray-Diffraction Films. American Mineralogist 78(11-12):1332-1335

Otto HH, Hofmann W, Schroder K (2002) A Double-Radius Gandolfi X-Ray Camera for the Generation of Powder-Like Diffractograms of Small Single Crystals, Using an Imaging Plate Detector. Journal of Applied Crystallography 35:13-16 doi:10.1107/s0021889801016594

Palmer DC (1997) Digital analysis of X-ray films. Mineralogical Magazine 61(3):453-461

Petrus JA, Ross KC, A.M. M (2011) DIIS: A Cross-Platform Program for the Reduction of X-Ray Diffraction Data from a Cylindrical Area Detector. Computers and Geosciences 1(1):1 - 2

Piltz RO, McMahon MI, Crain J, Hatton PD, Nelmes RJ, Cernik RJ, Bushnellwye G (1992) An Imaging Plate System For High-Pressure Powder Diffraction - the Data-Processing Side. Review of Scientific Instruments 63(1):700-703 doi:10.1063/1.1142641

Rajiv P, Hinrichsen B, Dinnebier R, Jansen M, Joswig M (2007) Automatic calibration of powder diffraction experiments using two-dimensional detectors. Powder Diffraction 22(1):3-19 doi:10.1154/1.2486434

Rietveld HM (1969) A profile refinement method for nuclear and magnetic structures. Journal of Applied Crystallography 2:65-&

Rodriguez-Navarro AB (2006) XRD2DScan: new software for polycrystalline materials characterization using two-dimensional X-ray diffraction. Journal of Applied Crystallography 39:905-909 doi:10.1107/s0021889806042485

Sonneveld EJ, Visser JW (1975) Automatic collection of powder data from photographs. Journal of Applied Crystallography 8(FEB1):1-7

The Rietvelt Method, (1991). Oxford Press

Vogel SC (2010) Reduction and analysis of two-dimensional diffraction data including texture analysis. High-Pressure Crystallography: from Fundamental Phenomena to Technological Applications:123-133 doi:10.1007/978-90-481-9258-8_11

Young RA, Wiles DB (1982) Profile shape functions in Rietveld refinements. Journal of Applied Crystallography 15(AUG):430-438 doi:10.1107/s002188988201231x

Zhukhlistov AP, Nickolsky MS, Zvyagin BB, Avilov AS, Kulygin AK, Nicolopoulos S, Ochs R (2004) Imaging plates - a new life for electron diffraction structure analysis. Zeitschrift Fur Kristallographie 219(4):224-226 doi:10.1524/zkri.219.4.224.30437

Figure captions

Figure 1 Figure 1 shows the integration vectors (yellow lines) for orthogonal integration (a) perpendicular to the central mirror plane of the diffraction image (green vertical line) and 2θ dependant integration (b). 2θ dependant integration avoids the assymetrical peak-shape that arises from orthogonal integration.

Figure 1

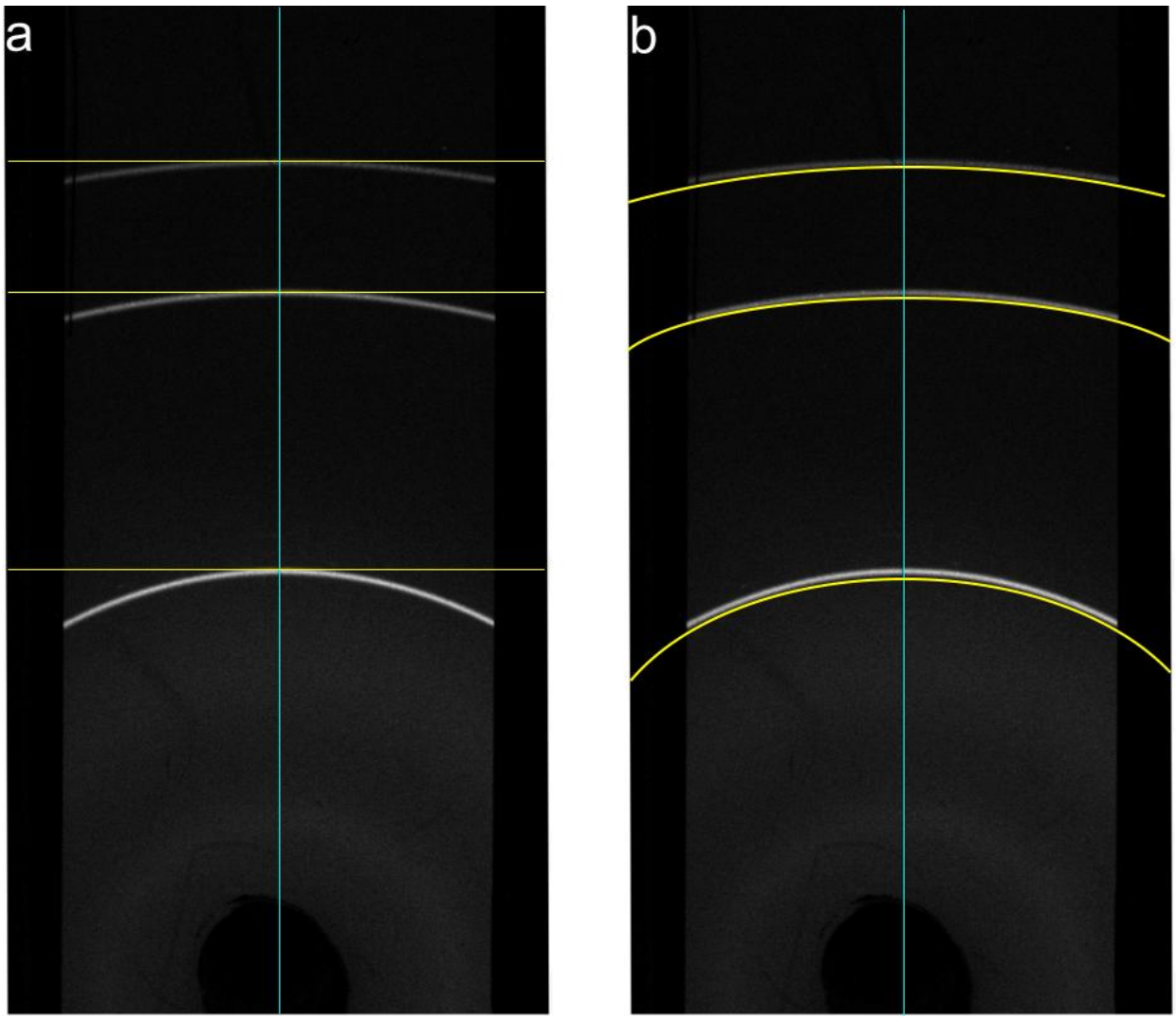

Table 1

Comparison of NIST and measured IP d-spacing for SRM640c

		Image Plate run					
	640C certified	10-020	10-168	10-145	MEAN IP	STDEV IPs (°2θ)	SRM640C-IP
		d-spacing [Å]					
(111)	3.1357	3.1330	3.1346	3.1360	3.1345	0.0015	0.0012
(220)	1.9202	1.9196	1.9195	1.9204	1.9198	0.0005	0.0004
(311)	1.6376	1.6371	1.6371	1.6378	1.6373	0.0004	0.0002
(400)	1.3578	1.3571	1.3575	1.3580	1.3575	0.0004	0.0003
(331)	1.2460	1.2454	1.2459	1.2461	1.2458	0.0004	0.0002
(422)	1.1086	1.1082	1.1087	1.1087	1.1085	0.0003	0.0001
(511)	1.0452	1.0448	1.0452	1.0453	1.0451	0.0002	0.0001
(440)	0.9601	0.9599	0.96	0.9603	0.9601	0.0002	0.0000
(531)	0.9180	0.9178	0.918	0.9181	0.9180	0.0002	0.0001
(620)	0.8588	0.8585	0.8587	0.8588	0.8587	0.0002	0.0001
(533)	0.8283	0.8280	0.8282	0.8284	0.8282	0.0002	0.0000
	a unit cell dimension [Å]						
	5.4312	5.4305	5.4313	5.4315	5.4311	0.0005	0.0001
Error	(<<1)	(1)	(1)	(2)			
	Agreement Indices						
Re		10.80	2.47	2.90			
Rp		4.10	1.23	1.50			
Rwp		6.50	1.61	1.97			
D		0.20	0.31	0.63			
GoF		0.35	0.42	0.46			
Zero shift (°2θ)		0.031	0.014	-0.009			
FWHM (°2θ ave)		0.33	0.24	0.35			
σ (n=11)		0.01	0.01	0.02			
u		0	0.005	0.002			
v		-0.003	-0.030	-0.004			
w		0.12	0.05	0.135			
n		0.06	0.2	0.03			
R-Bragg (%)		5.12	5.05	1.5			

Table 2

Comparison of NIST and measured IP intensities for SRM676a

	SRM 676		Image Plate run					
(hkl)	I/Io (%)	(error)	10-156	10-163	10-178	mean	STDEV IPs	SRM676a-IP
(012)	57.96	(1.8)	57.08	59.42	57.31	57.94	1.29	0.02
(104)	87.4	(0.65)	87.31	89.57	87.95	88.28	1.16	-0.88
(110)	36.32	(0.19)	37.16	37.09	37.51	37.25	0.23	-0.93
(113)	100		100	100	100	100	0.00	0.00
(024)	47.18	(0.41)	46.21	45.38	44.55	45.38	0.83	1.80
(116)	95.59	(1.21)	94.93	94.78	87.89	94.86	0.11	0.73
(124)	36.02	(0.78)	37.16	36.54	33.79	35.83	1.79	0.19
(030)	55.75	(1.26)	55.9	55.13	53.07	54.70	1.46	1.05
mean FWHM			0.3120	0.2125	0.2753			
σ (n=8)			0.0068	0.0071	0.0055			

Table 3

Cr-pyrope (space group Ia-3d)

Crystallographic parameters						
PXRD			SXRD			Δ (PXRD-SXRD)Å
a [Å]	11.5367	(1)	*a* [Å]	11.532	(2)	0.0047
Thermal isotropic parameter (Biso)						
X-site	0.66			0.89		
Y-site	0.52			0.49		
Z-site	0.47			0.51		
O1			O1			Δ (PXRD-SXRD)Å
x	0.0959	(3)	*x*	0.0967	(1)	-0.0008
y	0.2005	(2)	*y*	0.2005	(1)	0.0000
z	0.2843	(2)	*z*	0.2837	(1)	0.0006
	0.41			0.82		
Agreement parameters						
Rbragg (%)	4.25		R1 (%)	3.19		
Rwp	10.19			8.5		
GoF	0.61			1.12		
Re	13.09					
Rp	8.48					
D	0.30					

Instrument parameters	
Zero Shift (°2θ)	0.014
u	0.006
v	-0.005
w	0.092
n	0.152

Table 4

Cr-diopside (space group C2/c)

Crystallographic parameters

PXRD			SXRD			Δ (PXRD-SXRD)
a [Å]	9.7197	(3)	9.7203	(2)	-0.0006
b [Å]	8.8942	(4)	8.8941	(2)	0.0001
c [Å]	5.2536	(2)	5.2543	(1)	-0.0007
beta [°]	106.11	(2)	106.084		0.0240
B*ov.*	0.7500				
M1					
x	*0.0000*		*0.0000*		
y	0.5946	(2)	0.5927	(1)	0.0019
z	*0.2500*		*0.2500*		
Biso (Å^2)	2.46		0.89		
M2					
x	*0.0000*		*0.0000*		
y	0.1987	(2)	0.1990	(1)	-0.0003
z	*0.2500*		*0.2500*		
Biso (Å^2)	0.18		1.19		
SI					
x	0.2864	(3)	0.2869	(1)	-0.0005
y	0.4073	(4)	0.4070	(1)	0.0003
z	0.2292	(6)	0.2298	(1)	-0.0006
Biso (Å^2)	0.46		0.86		
O1					
x	0.1136	(6)	0.1153	(2)	-0.0017
y	0.4138	(9)	0.4137	(2)	0.0001
z	0.1442	(12)	0.1410	(4)	0.0032
Biso (Å^2)	0.34		1.10		
O2					
x	0.1476	(9)	0.1490	(2)	-0.0014
y	0.0182	(6)	0.0171	(2)	0.0011
z	0.0070	(17)	0.0031	(4)	0.0039
Biso (Å^2)	0.34		1.10		
O3					
x	0.3595	(7)	0.3614	(2)	-0.0019
y	0.2490	(6)	0.2490	(2)	0.0000
z	0.3234	(13)	0.3180	(4)	0.0054
Biso (Å^2)	0.34		1.10		

Agreement parameters			
	PXRD		SXRD
Rbragg (%)	3.44	R factor (%)	5.31
Rwp	5.96		9.38
GoF	0.44		1.08
Re	8.95		
Rp	5.20		
D	0.21		

Instrument parameters	
Zero Shift (°2θ)	-0.0029
u	0.016331
v	-0.032955
w	0.115312
n	0.336084

Table 4 continued

Chapter 3

An empirical test of the crystal lattice strain model for rare-earth element partitioning into clinopyroxene

Kirk Ross[a,$], Balz S. Kamber[b], Andrew M. McDonald[a]

[a]Department of Earth Sciences, Laurentian University, Sudbury, Ontario, Canada

[b]School of Natural Sciences, Trinity College Dublin, Ireland

[$]corresponding author mailing address: Department of Earth Sciences, Laurentian University, 935 Ramsey Lake Road, Sudbury, P3E 2C6, Ontario, Canada; (telephone: ++1 707 675-1151; fax: ++1 705 675-4898; email: kross@laurentian.ca)

Abstract

The significance of crystallographic control over trace element incorporation into minerals is now widely recognized. Its most accepted parameterization - the crystal lattice strain model – is increasingly being applied with success in experimental and empirical petrology. The fundamental premise of the crystal lattice strain model is that isovalent trace element incorporation is governed mainly by two factors, the radius of the substituent cation and the elastic modulus of the substituent lattice site.

This paper presents an empirical study that tests the premise of the crystal lattice strain model with a combination of high precision crystallographic and lanthanide data for the mineral clinopyroxene. Multiple aliquots of very small subgrains (ca. 50 μm diameter) were exposed to repeat XRD analysis (Gandolfi camera) and subsequently chemically analyzed by low-blank miniaturized solution ICP-MS procedure. Additional in situ chemical analyses were also obtained by laser ablation ICP-MS. Using Rietveld analysis, the XRD data define the structural parameters of the crystal, including the exact geometry of the M2 and M1 sites. The lanthanide data, when normalized to an appropriate bulk rock composition, yield a normalized concentration with similar effectiveness to the distribution coefficient. The apex of the resulting Onuma diagram is centered over the ideal radius, which can be quantified using a plot of radius parameter versus the natural logarithm of the apparent distribution coefficient. The combined dataset thus yields two completely independent estimates for the effective radius of the M2 cation (and for two samples also the M1 cation), for which the lanthanides substitute.

Comparison of the two independent estimates for the ideal radius yielded a robust positive correlation (r^2 = 0.879) with a slope of 0.911 for 4 of the 5 studied specimens and even stronger agreement, when M1 data are included. This study thus provides very strong empirical evidence that adds to a growing database of experiments showing the validity of the crystal lattice strain model.

1. Introduction

The crystal lattice strain model (CLSM) successfully describes trace element distribution in many experimental and empirical geochemical datasets, including the rare-earth elements (REE) in common rock-forming minerals such as clinopyroxene (cpx, e.g. Hill et al., (2000); Fedelle and Zanetti (2009); Hill et al., (2011)), plagioclase (e.g. Hattori and Sato (1996); Bindeman et al., (1998), and garnet (e.g. van Westrenen et al., (1999); van Westrenen et al., (2001); van Westrenen and Draper, (2007)). Thus, the CLSM provides a convenient crystal-chemical rationalization for trace element distribution (Brice, 1975; Blundy and Wood, 1994; LaTourrette et al., 1995). At the very heart of the CLSM is the concept that the apparent polyhedral elastic modulus combined with the effective ionic radius of a host site exerts control over the relative partition coefficients of isovalent cations that may occupy that site. Since the much-cited paper by Blundy and Wood (1994), the CLSM has gained very wide acceptance in the geochemical and petrological communities and a great number of trace element datasets have been successfully interpreted with this approach (e.g. Blundy and Dalton, 2000; Adam and Green, 2003; Lee et al., 2007).

In view of the wide acceptance of the CLSM, it is somewhat surprising that the fundamental crystallo-chemical premise of the model has not yet been scrutinized more

thoroughly. One of the few such tests was performed by Bottazzi et al. (1999), who successfully compared structural parameters obtained from single crystal X-ray diffraction (XRD) with chemical data for amphiboles collected using laser ablation inductively coupled plasma mass spectrometry (LA-ICP-MS). However, in view of its structural and chemical complexity, amphibole is not an ideal mineral for such comparison. Owing to advances in XRD, specifically single crystal XRD and image plate technology, it is possible to calculate (via Rietveld refinement) both accurate and precise structural parameters (i.e. unit cell dimensions, fractional atomic coordinates and thermo-isotropic parameters) from crystals or crystal fragments of 25 μm diameter or smaller. These datasets can be compared with the normalized concentrations of element i (NC = i concentration in mineral/ i concentration in presumed whole rock, discussed further below) for trace elements to test the fundamental assumptions behind the CLSM.

The objective of this study was to perform such a comparison for natural cpx, which was chosen because of its ability to incorporate the full range of REE and because the M2-O bond length minus the radius of O is typically between the largest (La 1.16 Å) and smallest (Lu 0.977 Å) REE. In other words, the apex of an Onuma diagram for the M2 site of cpx is within the range of observation, unlike in many other rock forming minerals. For example, in garnet the crystallographic site of REE substitution is smaller than Lu (X-site $\leq$ 0.97 Å) and in plagioclase it is larger than La (A-site $\geq$ 1.17 Å) as illustrated in figure 1. For these minerals, it is more difficult to constrain the size of the substitution site with adequate precision from REE information.

The structure of cpx is characterized by three crystallographically unique polyhedra coordinated by O. These are the 6-coordinated metal-site (M1), the 8-coordinated metal-

site (M2), and the 4-coordinated tetrahedral or T-site. Rare-earth elements mainly occupy the eight coordinated M2 site, while the four coordinated T-site is too small to accommodate the REE. In low- alumina cpx, the heavy REE (HREE) have also been reported to substitute into the six coordinated M1 site (Fedele et al., 2009; Olin and Wolff, 2010; Hill et al., 2011). The main question behind this study thus was whether the chemical and crystallographic data for REE substitution were mutually consistent.

2. Materials and methods

Where possible, an effort was made to study high quality crystals. The represented occurrences fall into four groups: a gem quality diopside from a potassic alkaline ultramafic complex (Inagli Cr-diopside); a further gem quality diopside from a carbonatite (Deeti Al-diopside); one omphacitic clinopyroxene from an eclogite; and two Cr-diopsides (grains #39 and #56) from kimberlite heavy mineral concentrates interpreted to have been derived from refractory garnet peridotite. These specimens were chosen to provide a range in crystal chemistries and formed in distinctive geological environments. Individual descriptions of specimens and their preparation for the various analyses are found in the electronic supplement.

Trace element data were produced in duplicate by two independent analytical techniques. In situ LA-ICP-MS was performed on polished grain mounts and very small crystal fragments (ranging in mass from 1.60 to 0.133 mg) were analyzed by solution ICP-MS to minimize the risk of systematic calibration bias. The crystal structural parameters were obtained using a Gandolfi based ‘powder’ diffractometry technique (Petrus et al., 2011; Ross and Petrus, submitted).

2.1. Chemical analysis

2.1.1. In situ geochemical analysis

Major element data were obtained from carefully polished grain mounts and thin sections. The grains were analyzed by wavelength dispersive spectrometry on a Cameca SX-100 electron microprobe (EMP) at the Ontario Geological Survey Geolabs. The instrument was operated with an acceleration voltage of 20 kV and a beam current of 20 nA. One specimen (Deeti) was analyzed by energy DS (EDS). Well characterized natural and synthetic standards were used for calibration.

In situ trace element data were obtained by ultra violet (UV) LA-ICP-MS using a Supercell^{TM} equipped NewWave^{TM} Nd: YAG 213 nm laser coupled to a ThermoFisher^{TM} X SeriesII quadrupole ICP-MS. Grain mounts and polished sections were ablated in 99.9995% pure He carrier gas (ca. 0.5 l min^{-1}), which was mixed immediately down-stream with Ar (0.8 l min^{-1}) to ensure efficient aerosol transfer to the plasma (e.g. Kamber, 2009). Where possible, a 100 µm spot size was used and the laser was fired with a repetition rate of 10 Hz. Fluence was kept constant at 11 $J \cdot cm^{-2}$. Total analysis time was typically 70 s, consisting of 30 s background acquisition, 25 s of ablation, and the remainder being washout. The synthetic glass standard NIST612 was used for calibration with Ca (as determined from the electron microprobe analyses) as the internal standard (e.g. Heinrich et al., 2003). Data quantification was performed with the Iolite software (Hellstrom et al., 2008).

2.1.2. Solution ICP-MS data

A very small fragment (ranging from 1.6 to 0.133 mg) of each studied cpx was also analyzed for extended trace element compositions using solution ICP-MS; except for the

Bakersville eclogite omphacite, where insufficient material remained after LA-ICP-MS and XRD analysis. Fragments were digested in 6 mL Teflon^{TM} vials using a mixture of 0.4 and 0.1 ml double and triple, respectively, sub-boiling distilled HF and HNO_3 for 72 h at 160°C on a hotplate. After conversion with HNO_3, the solutions were diluted with 6 ml 2% HNO_3 and spiked with 4.4 ppb ^{6}Li, Rh, Re, Bi and ^{235}U. Instrument response was calibrated with two independent digestions of USGS dolerite standard W-2 (Kamber, 2009). Even at the exceedingly low concentrations given from such small samples, this technique has produced REE data with internal errors and accuracy better than 4% (Babechuk et al., 2010).

2.2. Crystal structural data

2.2.1. Powder XRD

Powder X-ray diffraction data were obtained with a 114.59 mm Gandolfi camera, employing a Ni filtered CuKα radiation (average wavelength 1.1564) and operating conditions of 40 mA and 30 kV. The camera was equipped with a 0.3 mm pin-hole collimator and rotary vacuum pump capable of achieving an absolute pressure of 0.03 atm. The exposure times ranged between 4-10 h. For X-ray detection a BaFBr: Eu^{2+} FUJI^{TM} SR-type image plate (IP) was used. Individual grain fragments were gently crushed in an agate mortar then affixed to the end of a tapered glass fibre (100 drawn to 15 micron diameter) using fingernail hardener. The grain cluster had a total volume of ≈ 200 μm^3 consisting of at least 20 grains. A sufficient number of differently oriented grains with respect to the incident X-ray beam reduced the likelihood of reflection absences caused by preferred orientation.

The principal steps of data integration to achieve conversion of image plate data to a fully quantitative digital diffractogram were outlined in Matsuzaki and Shinoda (2004). The software used for the conversion of an IP diffraction image to a full-profile digital diffractogram was developed in house (DIIS Petrus et al., 2011). For this study, the accuracy of the data given from Rietveld refinement of integrated diffraction pattern was assessed by analysis of two cpx by the more widely used single crystal XRD technique. As will become evident, there is excellent agreement between the datasets.

Mean metal-oxygen (M-O) interatomic distances were determined from coordination analysis using structural parameters given from Rietveld refinement of the diffraction data. The M2 cation is neither centrally located nor isometrically coordinated by O within the polyhedron – giving rise to a variability of 0.2 Å in M-O bond lengths. The asymmetry of the M2 polyhedron prevents direct estimates of internal error. To obtain a measure of precision, multiple XRD analyses coupled with multiple Rietveld analyses were preformed on multiple aliquots of crystal fragments from which standard deviations for the estimated M-O interatomic distances were calculated.

2.2.2. Single crystal XRD

Single-crystal XRD (SXRD) data were collected with a Bruker Apex II three-circle diffractometer operated at 50 kV and 30 mA using MoKα radiation (graphite filter) and a detector-to-sample distance of 5.95 cm. Diffraction data were collected with ω scans at different φ settings using the program SAINT (Bruker, 1999). Bruker (1999) software was used to collect (SAINT) correct for absorption (SADABS) and refine (SHELXTL) was used to interpret the SXRD data. An empirical absorption correction calculated using

SADABS was applied. Reflection statistics and systematic absences were consistent with the space group C2/c.

3. Results

3.1. XRD data

3.1.1. Verification of powder XRD data

We tested and verified the powder XRD film integration technique proposed by Matsuzaki and Shinoda (2004) in the following manner. First, fragments from Cr-diopside grains #39 and #56, both with approximate dimensions of 30 μm x 40 μm x 40 μm, were used for single crystal XRD analysis. Separate fragments for powder diffraction analysis were extracted immediately adjacent to the region from where the single crystal specimen was taken. Adjacent material was obtained with a UV-laser milling device. Unit cell parameters, fractional atomic coordinates and selected interatomic bond lengths given from structural refinement of the single crystal and powder diffraction data are given in table 1. The exposed image plates from the powder diffraction experiments of grains #39 and #56 were each reduced and integrated in triplicate. The reported errors are the standard deviations of the three data reductions, or the averages of the errors given from three Rietveld structural refinements, whichever was greater.

For Cr-diopside grain #39, unit cell dimensions between the two methods agree to within better than ±0.008 Å (and 0.05^{o} beta) while differences in fractional atomic coordinates vary from +0.0039 to -0.0053 Å with most in agreement to better than ±0.0009 Å. Unit cell dimensions for Cr-diopside grain #56 agree markedly better than #39, with

approximately half the error and, in many cases, an order of magnitude better agreement for fractional atomic coordinates and unit-cell dimensions (table 1).

Structural parameters for the omphacite, Inagli Cr-diopside and Deeti Al-diopside were initially acquired by performing a search-match analysis of the digitized diffraction image and selecting the *.cif (crystallographic information file) from the highest ranked candidate. A Rietveld refinement of the crystallographic structural parameters was then performed using PANalytical X'Pert HighScore Plus (version 2.2.0) with the correct atomic proportions given from major element EMP analysis (EMPA). For Cr-diopside grains #39 and #56 the structure given from refinement of the single crystal data was used.

3.1.2. X-ray diffractogram changes in response to chemistry

A brief summary is provided here regarding the significance of details of cpx diffractograms. Based on the variability in major element composition of the minerals studied here (table 2), the three-dimensional space-filling arrangement of atoms in the various samples is expected to differ. In other words, these major element variations are above the threshold of Henry's Law (Prowatke and Klemme, 2006). Non-Henrian behaviour is characterized by changes in composition having a direct impact on crystallography. Within a mineral group such as the cpx, these changes are expressed as quantifiable differences in diffractograms. In addition to the unique scattering factor associated with each major constituent element, the atomic arrangement gives rise to diffractions at unique inter-planar spacing (d-spacing) that are collectively unique to each sample analyzed. This is illustrated in figure 2, where diffraction patterns for a diopside and an aegirine are contrasted. In these patterns, scattering contributions to individual

reflections were determined using the Crystal Maker software suite. The figure shows a detail of the diffractogram with clearly attributable differences in reflection intensity and d-spacing. A good example is the 310 reflection, which arises from X-ray scattering of the M1 and O3 atoms. The interplanar spacing, or d-spacing, is related directly to the *a* and *c* unit cell dimensions and fractional atomic coordinates of these atoms while contributions to the reflection intensity arise from both the O and the major element cation(s) in the M1 site, which is considered to be predominantly Mg in diopside. The unique diffractogram and major element chemistry of each crystal can be used to calculate size and geometry of the sites into which trace elements substitute. The resulting data can therefore be compared with the independent information from the apparent trace element distribution coefficients.

3.2. REE data

Based on experimental studies of REE partitioning into cpx (e.g. Hill et al., 2000) which show a direct correlation between HREE compatibility and Al occupancy of the T-site, or the Tschermak component, and the differences in M2 atomic coordination that cause the variability in diffractograms discussed above, it was anticipated that the REE patterns of the studied, chemically diverse cpx should show significant variation among the apices in each Onuma diagram. The REE data are reported in table 2 and graphically displayed as normalized patterns in figure 3. Their features are briefly discussed qualitatively for each of the studied grains.

To accurately describe the distribution coefficient of element i (Di) defined as the i concentration in the mineral/ i concentration in the melt, we need to know the concentration of i in both the mineral and the melt. Where the melt composition is

unknown, a proxy is provided by normalizing the REE concentration (NC) to an appropriate whole rock composition. In a closed system, the whole rock represents an aggregation of minerals that have precipitated from the melt and is therefore representative of the initial composition of the melt. Silicate melt inclusions (SMI) represent melt fractions entrapped in a mineral at the time of crystallization and are used to reveal the compositional evolution of a melt as it freezes (Zajacz and Halter, 2007). Zajacz and Halter (2007) have show that for most elements, the bulk rock does in fact provide an adequate approximation of the melt composition. Exceptions rarely include Fe, P and Ti, which have been shown to have concentrations lower in the SMI than the bulk rock (Danyushevsky et al., 2002; Michael et al., 2002). Such depletion of HFSE, P, and Fe has been attributed to post entrapment modification of the SMI rather than a melt that was truly different in composition. Importantly, the maximum D (Do) for REE3+ in the M2 site of clinopyroxene has been shown to be within one log unit of unity for many empirical (Onuma et al., 1968; Matsui et al., 1977; Zajacz and Halter, 2007; Severs et al., 2009; Fedele et al., 2009; Olin and Wolf, 2010) and experimental (Blundy and Dalton, 2000; Hill et al., 2000; Adam and Green, 2003; Law et al., 2000; Hill et al., 2011; LaTourrette et al., 1995) datasets. Shown in figure 3a are the REE concentrations measured in the Bakersville omphacitic cpx normalized to several different rock types including whole rock chemical data. The 6 numbered curves in 3a correspond to the omphacite REE data normalization by: (1) Chondrite (McDonough and Sun, 1995), (2) Depleted MORB mantle (DMM, Workman and Hart, 2005), (3) and (4) Primitive mantle (PRIMA) after Hoffman (1988) and McDonough and Sun (1989) respectively, (5) Whole rock data for the eclogite from which this omphacite was extracted. (6) n-MORB data

given by Hoffman (1988). While the height of the maxima in the REE pattern is quite variable (ranging over 4 orders of magnitude), the radius over which the apex is located does not show such variation. Figure 3b shows the same patterns as 3a with all the apices normalized to their maximum. Two observations are immediately apparent. First, most apices are located over similar ionic radii regardless of the maximum. Aside from the DMM normalization (curve 2), 4 of the 5 remaining normalizations show an apex located at about 1.0855 Å with a standard deviation of no more than 0.0002 Å despite showing greater than 3 orders of variation in maximum NC. Second, the downward sloping limbs of the REE pattern show the same degree of tightness regardless of the normalization chosen. Only a choice of a DMM for normalization causes significant skew in the apex of the REE diagram while no choice of normalization significantly impacts the limbs and overall shape of the REE diagram. Described below are the cpx grains studied and the corresponding choice of melt composition.

Bakersville eclogitic omphacite

The REE concentrations in this omphacite were normalized to host whole rock data (labeled WR in table 2) and the pattern (figure 3c) should thus be considered to reflect empirical distribution coefficients for the REE. The curve is smooth and bell-shaped (except Eu, which is not shown) with a maximum centred around Sm.

Inagli Cr- diopside

The REE concentrations were normalized with the abundances of a phlogopite-clinopyroxenite reported by Mues-Schumacher (1996). They show the expected smooth bell-shaped maximum (figure 3d), in this case centred on Sm. Both laser and solution data agree well within 1 sigma errors. The pattern shows conspicuous HREE enrichment

which, discussed further below, has been previously documented by Olin and Wolf (2010) and Fedele et al. (2009) to be a consequence of substitution into the M1 site.

Peridotitic Cr-diopsides

Comparative patterns from laser and solution ICP-MS data are shown in figures 3e and 3f for grains #56 and #39 respectively. In both cases, the datasets produced identical patterns, although the solution ICP-MS returned higher total REEs. This could be the product of heterogeneity in concentration (e.g. Francis and Minarik, 2008) or an analytical bias either from internal standardization of the LA-ICP-MS data (i.e. Ca concentration measured by another technique) and/or weigh-in error for the very small fragments (0.02 mg) for the solution ICP-MS analysis. Regardless, for the following discussion and quantification, it is the shape of the REE pattern rather than the absolute REE concentrations that is directly relevant. The pattern of grain #56 is somewhat irregular, showing an asymmetry in the middle REE (MREE)-portion. This is reproduced well in the both the laser and solution data and cannot, therefore, be a calibration issue. Regardless, the apex of the bell is clearly centred on Nd and not on Sm as in the previous two patterns. Conversely, the REE pattern for grain #39 is very smooth and compared to grain #56, the apex is clearly centred on Ce, with only a slight positive slope on the light REE (LREE) side of the curve

Deeti diopside

For this cm-sized specimen, no whole rock was available for normalization. Instead, the REE pattern was normalized with a whole rock composition of a related combeite-wollastonite nephelinite melilite (Klaudius and Keller, 2006), which does not represent the exact locality of the Deeti diopside. The CI-normalized whole rock pattern (3f) has

slight irregularities (e.g. in the monoisotopic HREE), which are propagated into the melilite-normalized cpx patterns of both the solution ICP-MS and LA-ICP-MS datasets. We regard this as an analytical artifact of the whole rock analysis. Illustrated in figure 3f, both analytical approaches for this cpx yields a clear apex on Sm, even though the patterns are not strictly parallel. The LA-ICP-MS pattern reflects fifty-one analyses along two traverses, which did not show heterogeneity. The XRD pattern was obtained from material closest to the aliquot used for solution ICP-MS. Therefore, the solution ICP-MS REE dataset was used for comparison with the crystallographic data.

In summary, the REE patterns obtained for all five cpx show approximate bell shaped curves, the apices of which are centred from Ce to Sm. It is postulated that these curves represent REE substitution into M2 sites of slightly different size. The Inagli diopside also shows conspicuous enrichment in the HREE, which is believed to indicate additional substitution of HREE into the M1 site. The different radii at which the apices of the Onuma diagrams are located are considered to reflect differing polyhedral volumes and hence, differing mean M-O bond distances.

4. Discussion

4.1. Constraints on M2 site from REE patterns

A brief review of the Onuma and 'Brice' diagrams

To better appreciate how the variations in REE trends exhibited by the cpx studied here can be quantified, it may be beneficial to remind unfamiliar readers of the principles behind the CLSM. Onuma et al. (1967) empirically documented the inverse parabolic distribution that emerges when the natural logarithm of the distribution coefficient is

plotted against the effective ionic radius (taken here from Shannon, 1976) for cations of identical charge but with systematically varying radii, as is the case for the lanthanides (figure 4a). Following Onuma's work, Brice (1975) formulated the parameterization of an Onuma-type inverse parabola with the now well-established radius parameter, given as:

Equation 1 $$\text{Radius parameter} = Ro/2 \times (Ri - Ro)^2 + 1/3 \times (Ri - Ro)^3$$

This parameter is used to quantify the strain energy induced by incorporation of a misfit cation of radius Ri, into a lattice site of ideal radius, Ro (where $Ri \neq Ro$).

The strain energy penalty on the lattice for admission of a misfit cation is reflected in the convex downward sloping parabola, whose apex is centrally positioned over Ro. In this parameterized fit to data in the Onuma diagram (figure 4a), the slight asymmetry given from the moderate slope right limb (cations smaller than Ro) arises from the 2^{nd} term in equation 1, which increases in importance for large differences between Ri and Ro. Although not readily appreciable from fig. 4a, cations 0.1 Å smaller than Ro have nearly 10% greater admittance than those 0.1 Å larger.

In order to accurately locate Ro, advantage is taken of the fact that the exponential nature of the radius parameter and the natural logarithm of the distribution coefficient yield a Ln-linear relationship. In this diagram (figure 4b), here informally referred to as a 'Brice diagram' (after Brice 1975), the entire information from all REE that follow the distribution behaviour parameterized by Brice (1975) are used to determine Ro. Care

must be taken to ensure that the elements chosen for a given lattice site do not also partition into other polyhedra in the mineral, or polytypic phase inclusions. Anomalous polyhedral contributions become evident in the Onuma diagram when LnD vs. ionic radius do not conform to a smooth concave downward parabolic distribution or, in the Brice diagram, by poorly-convergent data.

The y-intercept on the Brice diagram reflects the precise apex of the Onuma diagram and represents the natural logarithm of the maximum distribution coefficient (Do). This value of Do corresponds to a fictional cation of radius Ro with a radius parameter of zero and therefore strain-free admittance into the lattice site. The slope defined by data in the Brice diagram corresponds to both limbs of the Onuma diagram, reflecting the propensity of the lattice site to incorporate misfit cations. The slope is therefore directly proportional to the elastic modulus (E) of the lattice site (Brice, 1975; Blundy and Wood, 1994; LaTourrette et al., 1995).

By way of example, these systematics are illustrated in figure 4 for the omphacite from the Bakersville eclogite. Identical calculations were performed for all samples and the resulting parameters are listed in the electronic appendix.

4.2. Discussion of REE constraints on ideal radius of the M2 site

Chrome diopside from the Inagli complex showed a high degree of homogeneity in terms of both major and trace element compositions as well as in paucity of foreign mineral inclusions. Similar to the Deeti Al-diopside, the Inagli Cr-diopside is considered to have precipitated from an incompatible element enriched, late stage, highly evolved melt. The overall elevated concentrations of REE are a clear advantage for distribution coefficient determination but a difficulty arises in correctly choosing an appropriate melt

composition because of the very coarse-grained nature of the host rock. The very strongly LREE-enriched (La/Lu ≈ 200) phlogopite-clinopyroxenite composition given by Mues-Schumacher (1996) was used as this is thought to most closely approximate the host melt composition. The resulting Ro and slope are 1.089 Å and 292.

Bakersville eclogite omphacite

Omphacite from the Bakersville eclogite showed the greatest chemical variation of all the material studied here. In terms of major elements it forms a bimodal distribution of cpx consisting of Al-rich (>9 wt.%) and Al-poor (<3 wt.%) grains. Material from the latter population was interpreted to represent prograde metamorphic cpx (Page et al., 2003) whereas material from the former are considered prograde metamorphic material and show a bimodal apex in the REE Onuma diagram. This suggests that the REE are distributed over more than one M2 site. This may at first seem unexpected in light of the fact that the standard cpx structure possesses only one unique M2 site into which all REE are considered to partition. However, the crystal structure of omphacite differs from most other cpx in that it possesses a doubled unit cell (Green et al., 2007) giving rise to the possibility of REE being partitioned into two crystallographically distinct 'M2' sites. This feature is the most likely explanation for the Onuma diagram for this mineral, which resembles a composite of two slightly transposed parabolae. If true, the observation could reflect that in ordered omphacitic pyroxene Al in the M1 site must undergo coupled substitution with Na in the M2 site to maintain charge neutrality. The high-Al omphacite is essentially composed of two crystallographically unique pyroxene lattices intimately intermixed on an atomic level, e.g. doubled unit cell each with a unique M1 and M2 site. The low-Al cpx did not show such complexities and it was therefore chosen for analysis.

The omphacite REE trend for the Brice diagram is illustrated in fig. 4b and the resulting Ro and slope are 1.086 Å and 389.

Peridotitic chrome diopsides

The two peridotitic Cr-diopsides represent mantle xenocrysts but their host rock compositions are not known. According to the major element criteria proposed Nimis and Taylor (2000) they are expected to have crystallized in the garnet stability field from a depleted protolith. Therefore, both minerals were normalized to primitive mantle (McDonough and Sun, 1995) and the resulting apparent distribution coefficients give tight regressions in the Brice diagram. Grain #56 yielded an Ro of 1.081(1) Å, while grain #39 returned a notably larger ideal radius of 1.166(1) Å. As the solution and LA-ICP-MS data are identical, the derivation of Ro and slope are not are not strongly dependent on which dataset is used, but for the data obtained via LA-ICP-MS, Do is closer to unity.

Deeti aluminous diopside

It has been shown experimentally that HREE appear to be more strongly enriched in aluminous cpx, particularly those with a high Tschermak component (e.g. Hill et al., 2000). Such HREE enriched cpx necessarily produce systematically smaller Ro values for the M2 site. The natural Al-rich cpx from the Deeti melilitite provides an empirical test of these experimental findings. Using the PX-NOM program of Sturm (2002) and the major element compositional obtained from EMPA, it was estimated that the T-site is occupied by 0.081 Al and 0.027 Ti apfu. In agreement with the experimental trend shown by Hill et al. (2000), this cpx yielded the smallest Ro, 1.065(1), of all cpx studied here.

4.3. Discussion of structural constraints on ideal radius

4.3.1. Factors affecting the 'size' of the M2 site

Unlike in the chemical approach, from which a unique 'ideal' radius is estimated for substituting isovalent cations that differ slightly in radii (ca. 0.1 Å), structural data yield information about the atomic arrangement of the site into which trace metals substitute. In other words, structural data are sensitive to the exact coordination of the metal cation. A feature common to all cpx are chains of edge-sharing $M1O_6$ octahedral groups parallel with corner-sharing SiO_4 tetrahedral groups. Differences among cpx arise with respect to bonding that involves the M2 atom. In every cpx the M2 atom is bonded to four O atoms (two each of O1 and O2). The M2 atoms may, however, have up to four additional bonds with the O3 atoms, such as in the samples studied here. While the O1 and O2 atoms are confined to edge sharing octahedral and octahedral-tetrahedral linkages respectively, the O3 atoms represent the bridging O between the corner sharing SiO_4 groups. Thus, the proximity of the O3 atoms to the M2-site determines the coordination characteristics of the surrounding O. X-ray diffraction data acquired from all cpx studied here exhibit *C2/c* symmetry. Considering that *C2/c* is centrosymmetric and the M2 cation resides on the 2-fold within the unit cell, the M2 cation must be coordinated by an even number of oxygen atoms (i.e. 4, 6 or 8). A further complication is that despite the physical geometric arrangement of O atoms surrounding the M2 site, not all of the geometrically coordinating O contribute to a charge balancing interaction with the central cation. Namely, the central atom is not necessarily bonded to all nearest-neighbour O atoms. Downs (2003) showed that in some *C2/c* pyroxenes (e.g. ferrosilite and jadeite) the M2 cation is bonded to only two of the four bridging O3 atoms that coordinate the M2-site.

However, all pyroxene studied here is dominated by Ca in the M2 site and is therefore both geometrically and electrostatically coordinated by 8 O atoms. Because four O3 atoms coordinate the M2 site, derivation of the ideal radius from a mean M2-O bond length by XRD is necessarily sensitive to the positioning of the O3 atoms in the crystal structure. Results from studies on polyhedral variation in synthetic pyroxenes (Nestola et al., 2007; Thompson and Downs, 2008 and references therein) show the M2 polyhedral coordination is a consequence of the M1 and T polyhedral rotations and changes in the M1 polyhedral volume, rather than a direct result of the M2 cation. This implies that to a large degree, the M2 is occupied primarily by a locally-available energetically-favourable cation, rather than an M2 cation that causes significant structural modification. These observations are consistent with the T site having the highest elastic modulus, followed by the M1 and M2 sites.

For the tetrahedral site, coordination analysis resulted in an average T-O bond length of 1.635 Å (± 0.005) for each cpx studied here. Considering the T-O bond length does not change significantly for cpx that differ greatly in composition, a contributing mechanism by which the M2-O3 distance can vary is via tetrahedral rotation. As shown experimentally by Hill et al. (2000) and Nestola et al. (2007), in cpx with the *C2/c* structure type the M2 Ro is primarily a consequence of the T and M1 site polyhedral rotations and change in the M1 volume. This is exemplified by the Deeti Al-diopside, which has an appreciable Tschermak component. Increases in the observed T-O bond distances are necessary to accommodate the larger Al ion ($Si^{4+}_{[IV]}$ 0.26 Å, $Al^{3+}_{[IV]}$ 0.39 Å). Tetrahedral expansion combined with M1-O bond shortening are also both required

to accommodate the required M1 Al for charge neutrality, results in an overall decrease of M2 Ro as indicated by the XRD data.

It should be noted that Deeti Al-diopside, grain #56 and to a lesser degree, the eclogitic omphacite, all contain an appreciable jadeite component (Na + Al, table 2). The incorporation of monovalent Na in the M2 must be charge balanced by a trivalent cation (in these cases Al) in the M1 ($Ca^{2+} + Mg^{2+} \Leftrightarrow Na^{1+} + Al^{3+}$). With increasing jadeite component, Henry's Law will become dissatisfied giving rise to a symmetry reduction from *C2/c* to the $P2_1/n$, a change that corresponds to a doubled unit cell. The doubled unit cells permits the formation of two crystallographically distinct M2-sites where each site may differ in ideal radius. The REE data for these three cpx do in fact indicate that this may be the case as an irregular broadening near the Onuma apex is observed.

4.3.2. Estimating the length of the metal bond in M2

Regardless of these complications, for comparison of the CLSM and structural data it was reasonable to consider the M2 atoms in all cpx studied here to be in 8-fold coordination. Therefore, to a first approximation, we took the mean M2-O bond distance minus the radius of O to represent Ro. Bond valence analysis showed that the three crystallographically unique O are not themselves all in either 3- or 4-fold cation coordination in each mineral. For this reason, it was considered that a mean O radius would be most suitable.

The effective ionic radius of O in the M2 site of cpx cannot simply be equated with Shannon's (1976) nominal ionic radius for O in 3- (1.36 Å) or 4-fold coordination (1.38 Å). For example, Wood and Blundy (1997) estimated an effective ionic radius for O (1.38 Å) corresponding to that of O in tetrahedral coordination. In reality, in the cpx

structure the O1 atom is in 4-fold coordination while the O2 and O3 atoms are in 3-fold coordination giving a mean O radius of 1.367 Å. For the purpose of consistency with Wood and Blundy (1997), however, the nominal O radius of 1.38 Å (Shannon, 1976) was chosen and subtracted from the mean M-O bond length to estimate Ro. All the calculated values for M2 Ro are listed in table 3. For two samples where sufficient data for smaller trivalent cations were also available, the M1 Ro was also calculated.

Even in this simplified approach, the Ro given from the CLSM is not directly comparable to Ro given from XRD as the XRD data will give Ro based on the valence of the host cation. In all cases, the host cation is divalent. It has been shown that Ro for a given site decreases with increasing valence of the substituent cation (Blundy and Dalton, 2000; Law et al., 2000). Thus the Ro given from analysis and interpretation of the CLSM based on tri-valent ions is not directly comparable to Ro given from XRD as the latter provides the average crystallographic properties dominated by the divalent host cations, rather than the trivalent trace-cations used in the CLSM. Therefore M2 Ro for each mineral will systematically differ because of the difference in valence of the cations for each method used to determine Ro.

4.4. Comparison of CLSM and structural estimates for Ro

For the cpx studied here, the absolute range of observed Ro for M2 is very small (0.028 Å by XRD and 0.065 Å by CLSM) and a quantitative comparison of the obtained Ro is difficult. From a qualitative perspective it was found that the order of Ro from largest to smallest was within error the same for both methods, except for Cr-diopside grain #39. Rietveld refinement of the XRD data indicates that the Cr- diopside grain #39 exhibits the largest Ro for the M2 site (1.124 Å) followed by omphacite and Inagli Cr-diopside at

1.122 and 1.116 Å and finally Deeti Al-diopside at 1.096 Å. The values of M2 Ro determined from XRD are compared with those determined from the CLSM in figure 6. When Cr-diopside grain #39 is excepted, a linear regression line ($r^2 = 0.879$) with a slope of 0.911 is obtained. This indicates strong agreement between these two independent methods of deriving M2 Ro.

Chromian diopside grain #39 returned a smaller Ro based on triplicate XRD analyses (1.1240 ± 0.002 Å) than that obtained by CLSM (1.166 ± 0.001 Å) performed on duplicate separate solution ICP-MS REE analyses of separate aliquots. This discrepancy is clearly outside analytical error and may result from several possible factors, three of which are discussed here. First, in this particular sample, the CLSM could have failed and REE incorporation was governed by additional parameters (e.g. mantle metasomatism by a fluid). Second, after initial REE incorporation at the time of crystallization, this particular cpx may have experienced crystallographic modification at temperatures too low to allow for diffusive trace element equilibration. Third, the apparent distribution coefficients obtained by normalizing to primitive mantle are grossly in error. This final possibility is illustrated on figure 5, where the REE concentrations are normalized to a very strongly enriched melt (e.g. to simulate a proto-kimberlite) producing a very steeply negative CI-normalized slope. This results in a different Onuma parabola with an apex significantly shifted towards a smaller Ro, similar to that obtained from XRD. As this sample is from a kimberlite, derivation of the cpx from a metasomatically enriched mantle domain appears as most likely reason for the discrepancy between XRD and CLSM derived Ro.

As discussed earlier, the M2 polyhedral coordination is influenced largely by the M1 and T polyhedral rotations and changes in the M1 polyhedral volume, which in itself is less variable than that of M2. For the two samples where enough trace element data was available for a reliable M1 Ro estimate (grain #56 and Inagli diopside), an excellent agreement was found between the CLSM and XRD approaches, in both cases returning Ro between 0.680 to 0.690 Å, reflecting the higher Young's modulus compared to M2. When the comparison of CLSM and XRD is extended to include estimates for Ro for both M1 and M2, all cpx samples fall on a tight correlation line that is parallel to the fit of the M2 data (figure 6).

4.5. Implications for petrogenetic problems relating to clinopyroxene

The most important conclusion to be derived from the empirical study presented here is that high-precision crystallographic data support the validity of the now widely used CLSM in geochemistry and petrology. The dimension and exact shape of the M2 polyhedron exerts dominant control over incorporation of the full REE spectrum for the majority of cpx, but for some, substitution into M1 also needs to be considered, as is increasingly appreciated (Fedele et al., 2009; Olin and Wolff, 2010).

When faced with the task of quantitatively modelling the influence of cpx on REE partitioning, be it in questions relating to melting or fractional crystallization, appropriate partition coefficients need to be chosen for the cpx most likely involved in the process. In cases where the cpx is preserved and available for analysis, it does not suffice to estimate partition behaviour from chemical composition alone. Table 3 shows an unexpected feature of the data presented here in that all values of Ro determined here are

systematically larger than the values predicted by equation 15 given in Wood and Blundy (1997). Their expression is:

$$Ro = 0.974 + 0.067\ XCa(M2) - 0.051\ XAl(M1)$$

This equation was calibrated strictly for Ca in the M2-site and Al in the M1-site without consideration given to any other structurally modifying component. For example, the kosmochlor ($NaCrSi_2O_6$) component, which is crystallo-chemically similar to aegirine, may have a significant effect. This is because trivalent Cr in the M1 site charge balanced by monovalent Na in the M2 may shift the apex of the Onuma parabola to larger radii. The presence of even a small Tschermak component, whether it be charge balanced by Al in the M1 and Ca in the M2 (CaTs) or an alternative compositional configuration, has a profound effect on M1 polyhedral rotation and ultimately the M2 site coordination and volume.

In the present dataset, the issue of incorrect choice of M2 Ro based on major element chemistry is well illustrated by the Inagli Cr-diopside and the Bakersville omphacite which differ significantly in major element compositions (see table 2). The equation of Wood and Blundy (1997) predicts an M2 Ro for the Cr-diopside that is larger than that for omphacite by 0.014 Å. However, both XRD and CLSM data (see electronic supplement) give Ro for both minerals that are nearly identical (Inagli Ro 1.089, omphacite Ro 1.086), with that of the Inagli only 0.003 Å larger. The reverse is observed for peridotitic Cr-diopside grain #56 and the Inagli Cr-diopside, having similar composition yet differing in Ro. Grain #56 shows greater Al and Na by 1.86 and 1.07 wt.% respectively while the Inagli Cr-diopside shows an increase in Ca concentration of

1.95 wt.%, confirming that Al and Na exert major influence on exact M2 dimension and coordination.

Alternate explanations for the deviation between Ro given here and that given by equation 15 of wood and Blundy (1997) include the incorrect choice of melt composition used to determine the apparent D values. Figure 7 shows a chondrite normalised plot of the measured whole rock and the calculated melt composition necessary to give an Ro from the method presented here and equation 15.

Petrologic investigations concerning themselves with melting of cpx-bearing sources need to consider the effect of pyroxene crystallography on partition coefficients. In an experimental study, Hill et al. (2000) documented how aluminous cpx can preferentially incorporate the HREE. Residual Al-rich cpx can thus impose a REE pattern on a melt that is easily mistaken to imply a garnet-bearing source. The effect of cpx chemical variability, and hence M2 site dimension, is also discussed by Green and Pearson (1985). These authors present diagrams of LnD REE vs. atomic number for twelve cpx of different petrogeneses. Although not strictly an Onuma diagram, each cpx differing in major element chemistry and lithology shows a unique REE pattern. The most extreme deviations from the norm are seen for cpx with an elevated aegirine or CaTs components, illustrating the need to choose proper D values for the exact cpx in question.

Enrichment in the heaviest REE apparent distribution coefficients exhibited by some cpx also needs to be taken into consideration. Regardless of the nature by which charge balance enhances or facilitates heaviest REE incorporation into the M1 site, the removal of such cpx from a melt cannot be adequately modelled with partitioning data obtained

from experiments that produced cpx into which REE substitution was strictly confined to the M2 site.

In situations where the equilibrium bulk (melt) REE composition can reliably be estimated from whole rock or melt inclusion analysis, Ro can be accurately constrained using the REE pattern of the cpx. This is achieved by least squares regression of the Brice diagram to yield an apex of the Onuma diagram over a fictional cation. The natural logarithm of the distribution coefficient for a cation of ideal radius should be near unity for elements isovalent with the host cation. Using silicate melt inclusions, Zajacz and Halter (2007) have shown this to be true while cations that differ from the ideal site valence or effective ionic radius invariably have a Do of less than one.

Empirical tests of the CLSM, such as those performed here on cpx, should naturally strive to obtain data from specimens of a mineral group that span maximum chemical complexity. This will extend the range of observable Ro and hence result in the most precise test of the model. However, if the chemical variability introduces too much structural complexity (e.g. conversion from one space group to another; or change in coordination) or charge balance requirements that may favour trace element incorporation, interpretation of the crystallography from trace element data alone is currently unreliable at best. Within these limitations imposed by crystallography, the results reported in this study can be considered fully compatible with predictions by the CLSM.

Acknowledgments: Roger Mitchell, Douglas Tinkham and Michael Seller are thanked for providing samples. Thomas Armbruster is thanked for single crystal analysis. Thomas Ulrich and David Crabtree provided expert analytical advice. Joe Petrus improved the

XRD data reduction software. Andrew McDonald contributed with many helpful suggestions and discussions. The facilities and research at Laurentian University were supported by an NSERC Discovery grant to the second author and by the Canada Foundation of Innovation.

References

Adam J, Green T (2003) The Influence of Pressure, Mineral Composition and Water on Trace Element Partitioning between Clinopyroxene, Amphibole and Basanitic Melts. European Journal of Mineralogy 15(5): 831-841

Babechuk MG, Kamber BS, Greig A, Canil D, Kodolanyi J (2010) The behaviour of tungsten during mantle melting revisited with implications for planetary differentiation time scales. Geochimica et Cosmochimica Acta 74(4): 1448-1470

Blundy J, Dalton J (2000) Experimental comparison of trace element partitioning between clinopyroxene and melt in carbonate and silicate systems, and implications for mantle metasomatism. Contributions to Mineralogy and Petrology 139(3): 356-371

Blundy J, Wood B (1994) Prediction of crystal-melt partition-coefficients from elastic-moduli. Nature 372(6505): 452-454

Bottazzi P, Tiepolo M, Vannucci R, Zanetti A, Brumm R, Foley SF, Oberti R (1999) Distinct site preferences for heavy and light REE in amphibole and the prediction of D-Amph/L(REE). Contributions to Mineralogy and Petrology 137(1-2): 36-45

Brice JC (1975) Some thermodynamic aspects of the growth of strained crystals. Journal of Crystal Growth 28(2): 249-253

Danyushevsky LV, Sokolov S, Falloon TJ (2002) Melt inclusions in olivine phenocrysts: Using diffusive re-equilibration to determine the cooling history of a crystal, with implications for the origin of olivine-phyric volcanic rocks. Journal of Petrology 43(9): 1651-1671 doi: 10.1093/petrology/43.9

Downs RT (2003) Topology of the pyroxenes as a function of temperature, pressure, and composition as determined from the procrystal electron density. American Mineralogist 88(4): 556-566

Fedele L, Zanetti A, Morra V, Lustrino M, Melluso L, Vannucci R (2000) Clinopyroxene/liquid trace element partitioning in natural trachyte-trachyphonolite systems: insights from Campi Flegrei (southern Italy). Contributions to Mineralogy and Petrology 158(3): 337-356

Francis D, Minarik W (2008) Aluminum-dependent trace element partitioning in clinopyroxene. Contributions to Mineralogy and Petrology 156(4): 439-451

Green E, Holland T, Powell R (2007) An order-disorder model for omphacitic pyroxenes in the system jadeite-diopside-hedenbergite-acmite, with applications to eclogitic rocks. American Mineralogist 92(7) 1181-1189

Green TH, Pearson NJ (1985) Rare-earth element partitioning between clinopyroxene and silicate liquid at moderate to high pressure. Contributions to Mineralogy and Petrology 91(1): 24-36

Heinrich CA, Pettke T, Halter WE, Aigner-Torres M, Audétat A, Günther D, Hattendorf B, Bleiner D, Guillong M, Horn I (2003) Quantitative multi-element analysis of minerals, fluid and melt inclusions by laser-ablation inductively-coupled-plasma mass-spectrometry. Geochimica et Cosmochimica Acta 67(18): 3473-3497

Hellstrom J, Paton C, Woodhead J, Hergt J (2008) Iolite: software for spatially resolved LA-(quad and MC) ICPMS analysis, Mineralogical Association of Canada short course series 40: 343-348

Hill E, Wood BJ, Blundy J D (2000) The effect of Ca-Tschermaks component on trace element partitioning between clinopyroxene and silicate melt. Lithos, 53(3-4): 203-215

Hofmann AW (1988) Chemical differentiation of the Earth: the relationship between mantle, continental-crust, and oceanic-crust. Earth and Planetary Science Letters 90: 297-314

Kamber BS (2009) Geochemical fingerprinting: 40 years of analytical development and real world applications. Applied Geochemistry 24(6): 1074-1086

Klaudius J, Keller J (2006) Peralkaline silicate lavas at Oldoinyo Lengai, Tanzania. Lithos 91(1-4): 173-190

Latourrette T, Hervig RL, Holloway JR (1995) Trace-element partitioning between amphibole, phlogopite, and a basanite melt. Earth and Planetary Science Letters 135(1-4): 13-30

Law KM, Blundy JD, Wood BJ, Ragnarsdottir KV (2000) Trace element partitioning between wollastonite and silicate-carbonate melt. Mineralogical Magazine 64(4): 651-661

Lee, C-TA, Harbert A, Leeman WP (2007) Extension of lattice strain theory to mineral/mineral rare-earth element partitioning: An approach for assessing disequilibrium and developing internally consistent partition coefficients between olivine, orthopyroxene, clinopyroxene and basaltic melt. Geochimica et Cosmochimica Acta 71(2): 481-496

Matsuzaki T, Shinoda K A method for digitizing the X-ray diraction pattern on X-ray film by Gandolfi camera. Journal of Geosciences 47: 1-8

McDonough WF, Sun SS (1995) The composition of the Earth. Chemical Geology 120(3-4): 223-253

Michael PJ, McDonough WF, Nielsen RL, Cornell WC (2002) Depleted melt inclusions in MORB plagioclase: messages from the mantle or mirages from the magma chamber? Chemical Geology 183(1-4): 43-61 doi: 10.1016/s0009-2541(01)00371-0

Mues-Schumacher U, Keller J, Kononova VA, Suddaby PJ (1996) Mineral chemistry and geochronology of the potassic alkaline ultramafic Inagli complex, Aldan Shield, eastern Siberia. Mineralogical Magazine 60(402): 711-730

Nagasawa H (1966) Trace element partition coefficient in ionic crystals. Science 152(3723):767-769 doi:10.1126/science.152.3723.767

Nestola F, Tribaudino M, Ballaran TB, Liebske C, Bruno M (2007) The crystal structure of pyroxenes along the jadeite-hedenbergite and jadeite-aegirine joins. American Mineralogist 92(8-9): 1492-1501

Nimis P, Taylor WR (2000) Single clinopyroxene thermobarometry for garnet peridotites. Part I. Calibration and testing of a Cr-in-Cpx barometer and an enstatite-in-Cpx thermometer. Contributions to Mineralogy and Petrology 139(5): 541-554

Olin PH, Wolff JA (2010) Rare earth and high field strength element partitioning between iron-rich clinopyroxenes and felsic liquids. Contributions to Mineralogy and Petrology 160(5): 761-775

Onuma N, Higuchi H, Wakita H, Nagasawa H (1968) Trace element partitioning between 2 pyroxenes and host lava. Earth and Planetary Science Letters 5(1): 47-51

Page FZ, Essene EJ, Mukasa SB (2003) Prograde and retrograde history of eclogites from the Eastern Blue Ridge, North Carolina, USA. Journal of Metamorphic Geology 21(7): 685-698

Petrus JA, Ross KC (2011) DIIS: A cross-platform program for the reduction of X-ray diffraction data from a cylindrical area detector. Computers and Geosciences 1(1): 1 - 2

Prowatke S, Klemme S (2006) Rare earth element partitioning between titanite and silicate melts: Henry's law revisited. Geochimica et Cosmochimica Acta 70(19): 4997-5012

Ross KC, Petrus JA (2012) submitted. Empirical assessment of the accuracy and precision of 2D Debye-Scherrer-type data collapsed onto a 1D diffractogram, Journal of Applied Crystallography

Severs MJ, Beard JS, Fedele L, Hanchar JM, Mutchler SR, Bodnar RJ (2009) Partitioning behaviour of trace elements between dacitic melt and plagioclase, orthopyroxene, and clinopyroxene based on laser ablation ICPMS analysis of silicate melt inclusions. Geochimica et Cosmochimica Acta 73(7): 2123-2141 doi: 10.1016/j. gca. 2009.01.009

Sturm R (2002) PX-NOM - an interactive spreadsheet program for the computation of pyroxene analyses derived from the electron microprobe. Computers and Geosciences 28(4): 473-483

Sun S –S, McDonough WF (1989) Chemical and isotopic systematics of oceanic basalts: Implications for mantle composition and processes. In: A. D. Saunders and M. J. Norry (Editors), Magmatism in ocean basins. Geol. Soc. Spec. Publ, London, 313-345.

Thompson RM, Downs RT (2008) The crystal structure of diopside at pressure to 10 GPa. American Mineralogist 93(1): 177-186

Wood BJ, Blundy JD (1997) A predictive model for rare earth element partitioning between clinopyroxene and anhydrous silicate melt. Contributions to Mineralogy and Petrology 129(2-3): 166-181

Workman RK, Hart SR (2005) Major and trace element composition of the depleted MORB mantle (DMM). Earth and Planetary Science Letters 231(1-2): 53-72 doi: 10.1016/j. epsl. 2004.12.005

Zajacz Z, Halter W (2007) LA-ICPMS analyses of silicate melt inclusions in co-precipitated minerals: Quantification, data analysis and mineral/melt partitioning. Geochimica et Cosmochimica Acta 71(4): 1021-1040

Figure captions

Figure 1: Ideal Onuma REE diagrams for garnet, with an ideal radius smaller than Lu, plagioclase, with an ideal radius greater than La and clinopyroxene, with ideal substitution in the middle REE.

Figure 2: XRD patterns of a diopside and an aegirine. (a) Selected region of the calculated XRD pattern from diopside single crystal data (blue) compared to calculated XRD pattern from powder diffraction data (red). Panel (b) illustrates the quality of agreement between the two calculated patterns. The largest error (approximately 5% RSD) is between the calculated intensities for the 100% diffraction indexed as the (22-1). (c) Calculated XRD patterns for diopside (blue) and aegirine (red) illustrating the observable difference in d-spacing and relative intensity for selected reflections indexed on a similar unit cell.

Figure 3: Normalized lanthanide diagrams for the studied clinopyroxenes. (a) Bakersville eclogitic omphacite normalized to: (1) Chondrite (McDonough and Sun, 1995), (2) Depleted MORB mantle (DMM, Workman and Hart, 2005), (3) and (4) Primitive mantle (PRIMA) after Hoffman (1988) and McDonough and Sun (1996) respectively, (5) Whole rock data for the eclogite from which this omphacite was extracted. (6) n-MORB data given by Hoffman (1988) (b) same normalizations as (a) shown with a common maximum. (c) Bakersville omphacite normalized to the whole rock composition. (d) Inagli chromian diopside normalized to Inagli Complex phlogopite-clinopyroxenite from Mues-Schuhmacher et al. (1996). The average of 31 LA-ICP-MS data shown. Error bars represent 1 standard deviation. Solution ICP-MS data (n=1) errors represent long-term reproducibility of USGS BIR-1 (Kamber, 2009). The apex of the curve is at Sm, highlighted with grey bar. (e) Peridotitic chromian diopside grain #56 normalized to CI chondrite of Sun and McDonough (1995). (f) Peridotitic chromian diopside grain #39 normalized to CI chondrite of Sun and McDonough (1995).

Figure 4: Effect of normalization on apparent ideal radius. Solution ICP data of peridotitic chromian diopside grain #39 normalized to CI chondrite (open circles connected with dotted curve) of Sun and McDonough (1995) and to an alkaline melt (solid circles connect with solid curve) with a very steep CI-normalized REE pattern (for

simplicity same as in fig. 3a; Inagli Complex phlogopite-clinopyroxenite). Note that panel plot shows effective ionic radius in reverse order along x axis.

Figure 5: (a) Onuma diagram of REE data for omphacite with apparent distribution coefficients obtained by normalizing with whole rock analysis. (b) Same data as in panel (a) but x-axis as radius parameter rather than ionic radius (informally referred to as 'Brice diagram', see text for discussion). Solid symbols are observed data (with their linear regression), open symbols represent modeled distribution coefficients.

Figure 6: Comparison of estimates for ideal radius from Rietveld analysis (x-axis) and REE-based CLSM (y-axis). Apart from peridotitic chromian diopside grain #39 (shown as crossed box) all analyzed samples define a very strong positive correlation. Error bars are smaller than symbol sizes. Two separate linear regressions are shown. The solid line combines data for M2 (solid circles) and M1 (open circles) and returns a very strong correlation coefficients. The stippled line shows regression of M2 data only. Note that slope and intercept are near-identical to the fit that includes M1 data.

Figure 7: Chondrite normalised Bakersville eclogite whole rock analysis *solid circles*. *Open circles* show a calculated melt composition required to give an Ro closer to that predicted by equation 15 of Wood and Blundy. Such an enriched source is not consistent with a rock of basaltic origin.

Figure 1

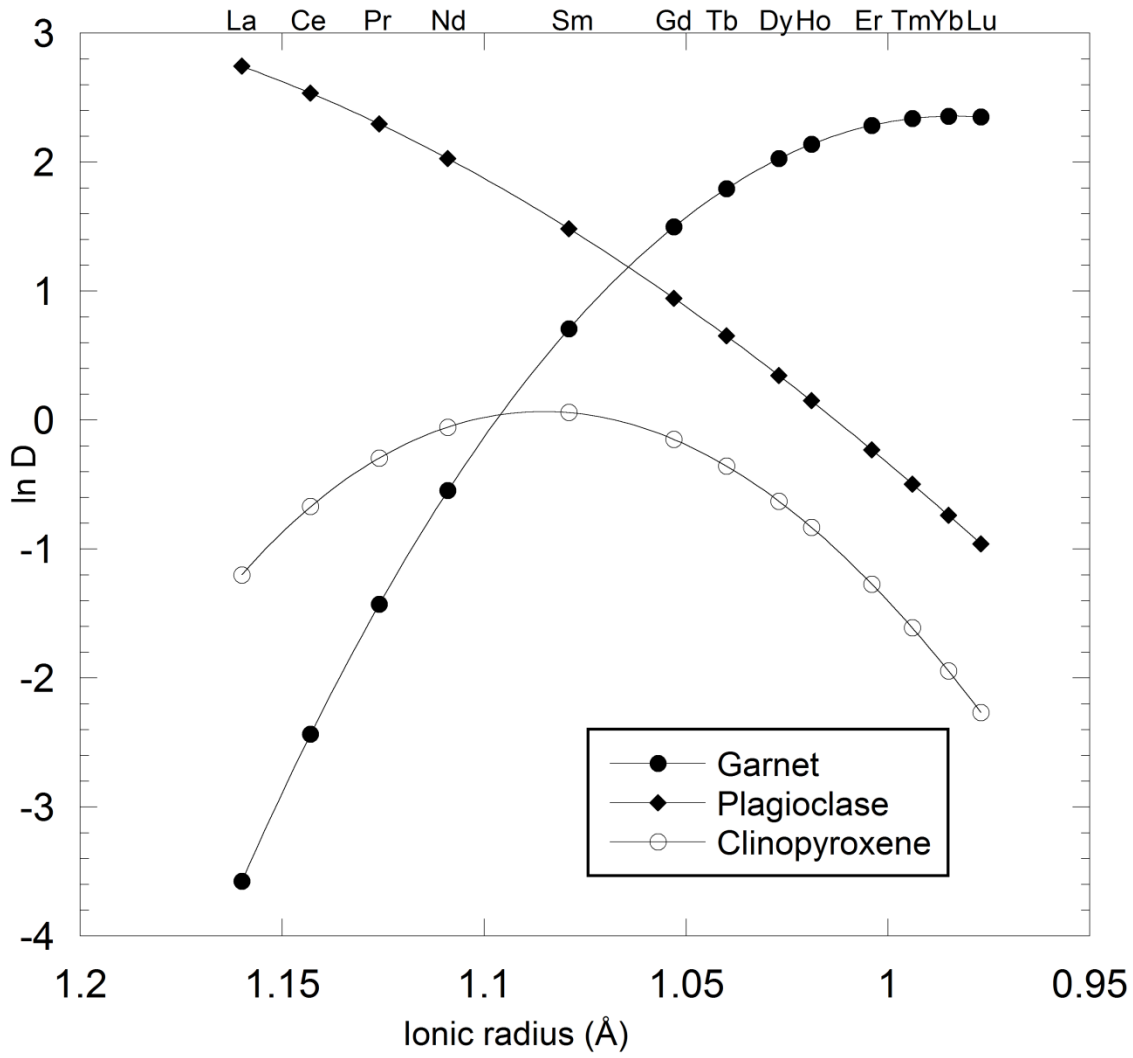
La
Ce
Pr
Nd
Sm
Gd
Tb
Dy
Ho
Er
Tm
Yb
Lu
3
2
1
0
-1
-2
-3
-4
ln D
1.2
1.15
1.1
1.05
1
0.95
Ionic radius (Å)
Garnet
Plagioclase
Clinopyroxene

Figure 2

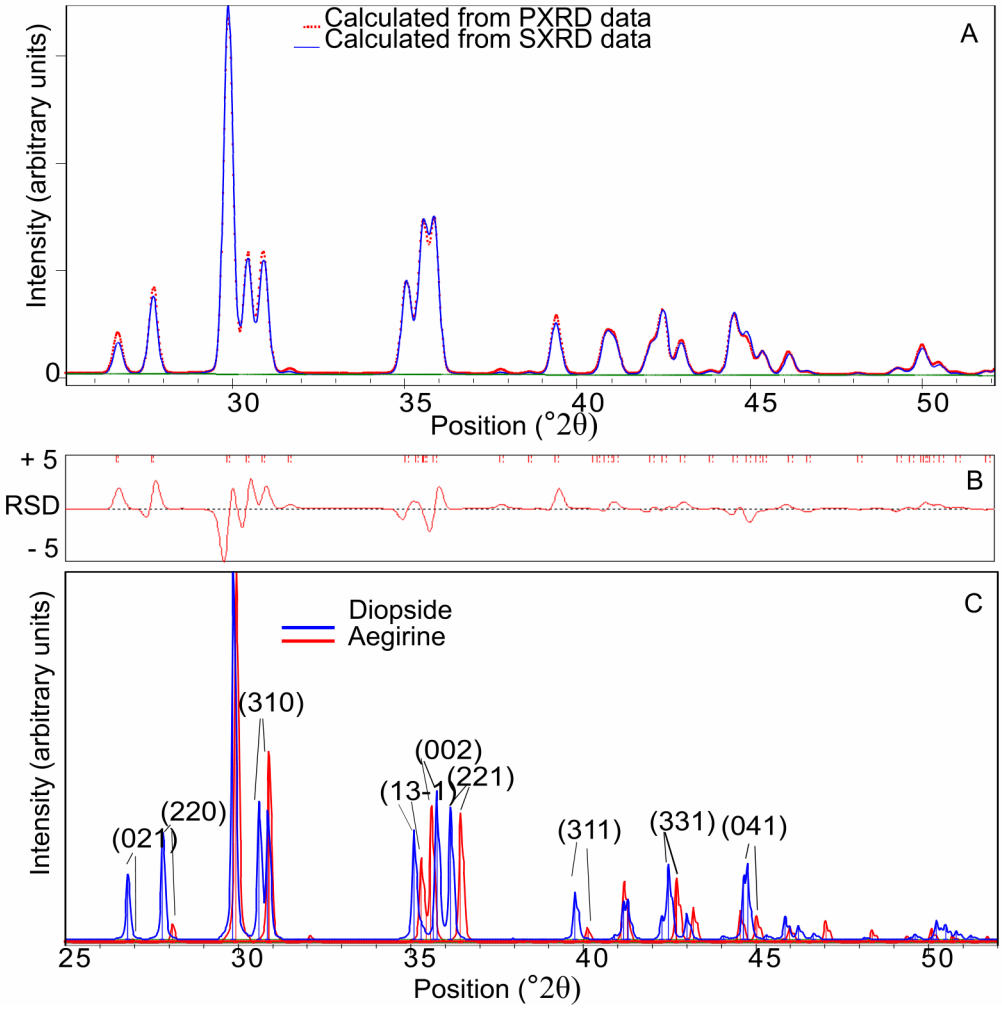
Calculated from PXRD data
Calculated from SXRD data
A
Intensity (arbitrary units)
0
30
35
40
45
50
Position (°2θ)
+ 5
RSD
- 5
B
C
Diopside
Aegirine
(310)
(002)
(221)
(13-1)
(220)
(021)
(311)
(331)
(041)
Intensity (arbitrary units)
25
30
35
40
45
50
Position (°2θ)

Figure 3

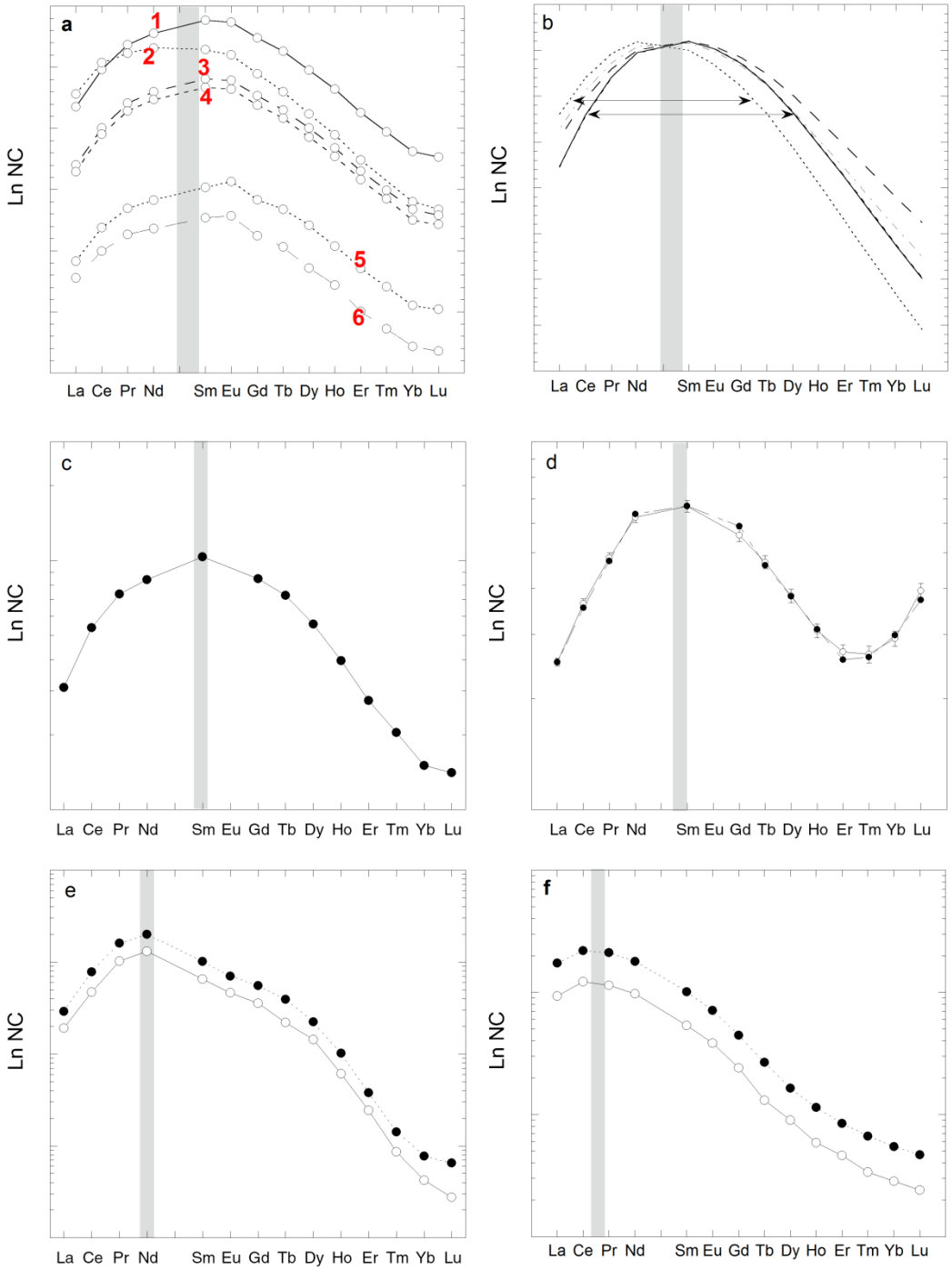
a
1
2
3
4
5
6
Ln NC
La Ce Pr Nd Sm Eu Gd Tb Dy Ho Er Tm Yb Lu
b
Ln NC
La Ce Pr Nd Sm Eu Gd Tb Dy Ho Er Tm Yb Lu
c
Ln NC
La Ce Pr Nd Sm Eu Gd Tb Dy Ho Er Tm Yb Lu
d
Ln NC
La Ce Pr Nd Sm Eu Gd Tb Dy Ho Er Tm Yb Lu
e
Ln NC
La Ce Pr Nd Sm Eu Gd Tb Dy Ho Er Tm Yb Lu
f
Ln NC
La Ce Pr Nd Sm Eu Gd Tb Dy Ho Er Tm Yb Lu

Figure 4

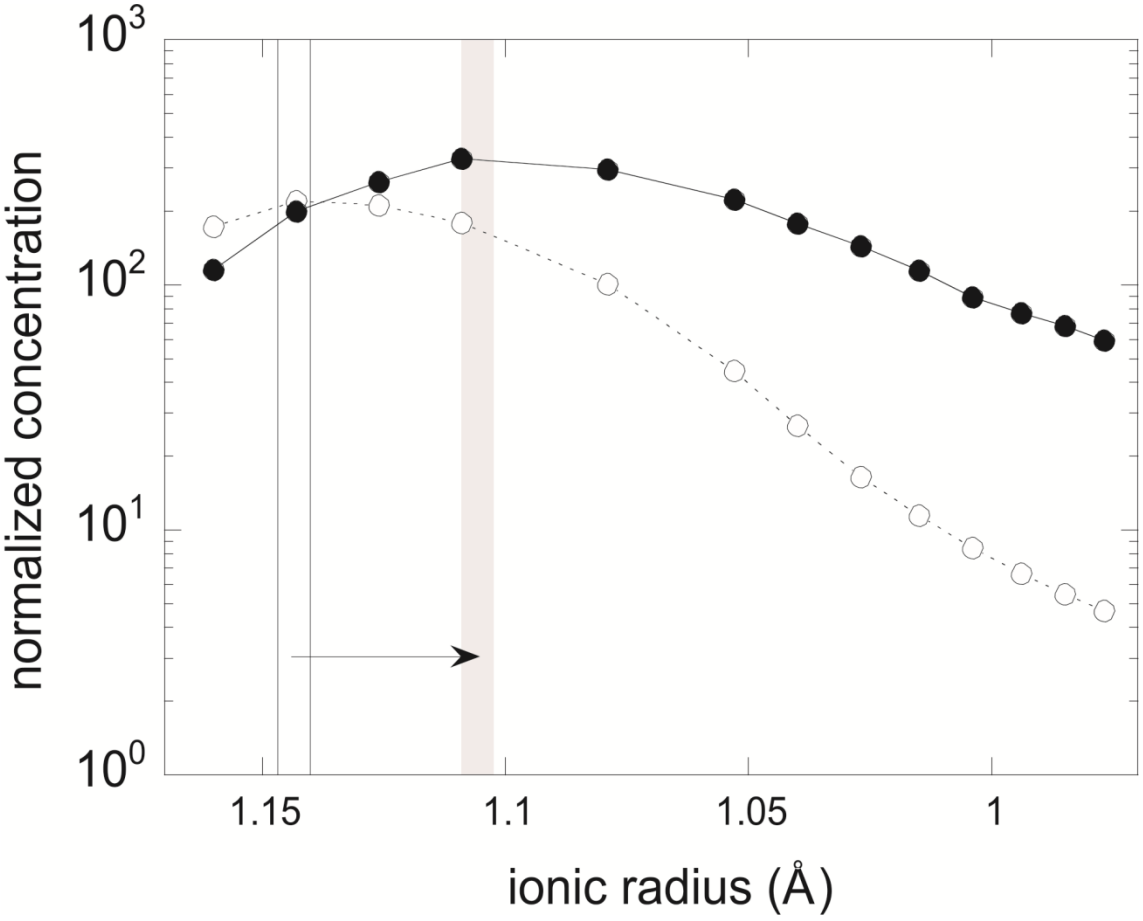
10^3
10^2
10^1
10^0
normalized concentration
1.15
1.1
1.05
1
ionic radius (Å)

Figure 5

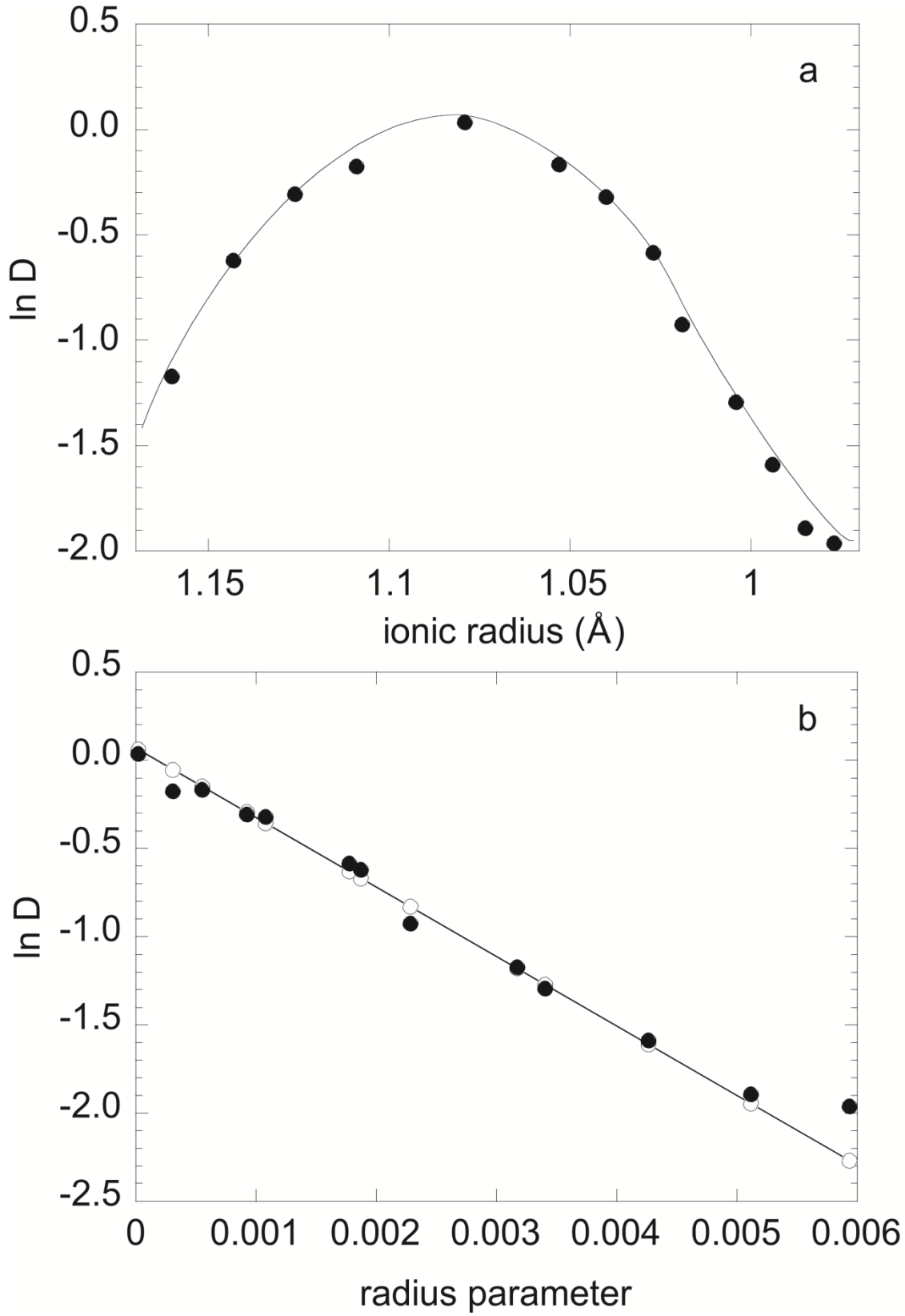
a
ln D
0.5
0.0
-0.5
-1.0
-1.5
-2.0
1.15
1.1
1.05
1
ionic radius (Å)
b
ln D
0.5
0.0
-0.5
-1.0
-1.5
-2.0
-2.5
0
0.001
0.002
0.003
0.004
0.005
0.006
radius parameter

Figure 6

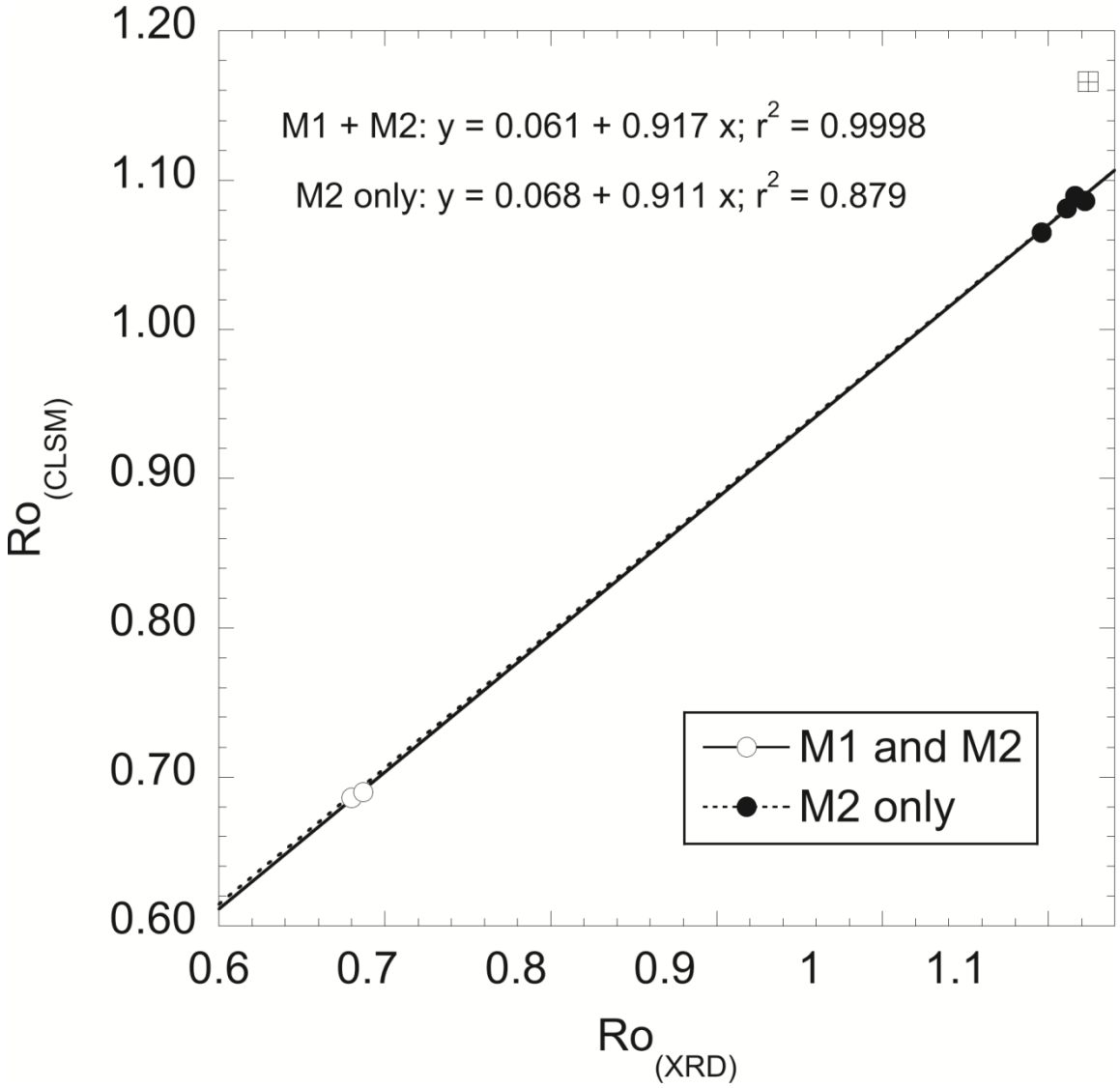
M1 + M2: y = 0.061 + 0.917 x; r2 = 0.9998
M2 only: y = 0.068 + 0.911 x; r2 = 0.879
M1 and M2
M2 only
Ro(CLSM)
Ro(XRD)
1.20
1.10
1.00
0.90
0.80
0.70
0.60
0.6
0.7
0.8
0.9
1
1.1

Figure 7

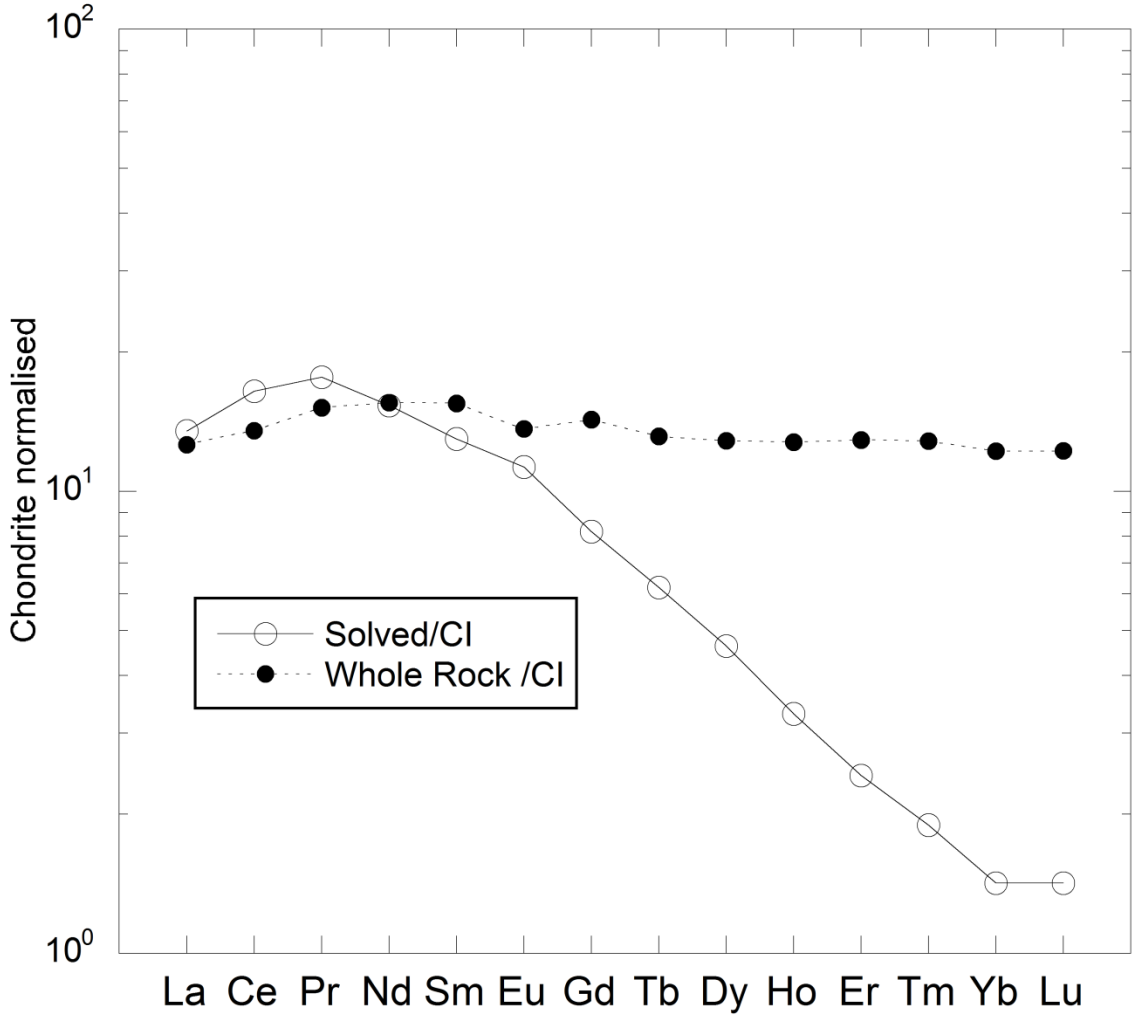
10^2
10^1
10^0
Chondrite normalised
Solved/CI
Whole Rock /CI
La Ce Pr Nd Sm Eu Gd Tb Dy Ho Er Tm Yb Lu

Table 1 Comparison of gandolfi and single crystal derived unit cell parameters and atomic coordinates

Grain 39					Grain 56				
Unit cell parameters									
Powder		Single xtl		Δ (powder-single) Å	Powder		Single xtl		Δ (powder-
a [Å]	9.7017 (2)	*a* [Å]	9.696 (2)	0.006	*a* [Å]	9.7178 (2)	*a* [Å]	9.720 (2)	-0.002
b [Å]	8.8782 (1)	*b* [Å]	8.873 (2)	0.005	*b* [Å]	8.8930 (2)	*b* [Å]	8.894 (2)	-0.001
c [Å]	5.2586 (1)	*c* [Å]	5.252 (1)	0.007	*c* [Å]	5.2526 (1)	*c* [Å]	5.254 (1)	-0.001
beta [°]	106.304 (2)	*beta* [°]	106.27 (3)	0.03	*beta* [°]	106.100 (2)	*beta* [°]	106.08 (3)	0.016
Fractional atomic coordinates									
M1		M1			M1		M1		
x	*0*	x	*0*	0	x	*0*	x	*0*	
y	0.5935 (2)	y	0.5933 (1)	0.0002	y	0.5928 (2)	y	0.5927 (1)	0.0001
z	*0.25*	z	*0.25*	0	z	*0.25*	z	*0.25*	
M2		M2			M2		M2		
x	*0*	x	*0*	0	x	*0*	x	*0*	
y	0.2000 (1)	y	0.1992 (1)	0.0008	y	0.1992 (2)	y	0.1990 (1)	0.0002
z	*0.25*	z	*0.25*	0	z	*0.25*	z	*0.25*	
SI		SI			SI		SI		
x	0.2877 (1)	x	0.2874 (1)	0.0003	x	0.2859 (2)	x	0.2869 (1)	-0.0010
y	0.4067 (1)	y	0.4073 (1)	-0.0006	y	0.4066 (2)	y	0.4070 (1)	-0.0004
z	0.2287 (2)	z	0.2303 (1)	-0.0016	z	0.2291 (4)	z	0.2298 (1)	-0.0007
O1		O1			O1		O1		
x	0.1128 (2)	x	0.1151 (2)	-0.0023	x	0.1126 (3)	x	0.1153 (2)	-0.0027
y	0.4141 (3)	y	0.4150 (2)	-0.0009	y	0.4167 (5)	y	0.4137 (2)	0.0030
z	0.1398 (4)	z	0.1403 (2)	-0.0005	z	0.1416 (6)	z	0.1410 (4)	0.0006
O2		O2			O2		O2		
x	0.1507 (3)	x	0.1488 (1)	0.0019	x	0.1498 (5)	x	0.1490 (2)	0.0008
y	0.0196 (2)	y	0.0167 (2)	0.0029	y	0.0194 (3)	y	0.0171 (2)	0.0023
z	0.0056 (7)	z	0.0021 (3)	0.0036	z	0.0058 (9)	z	0.0031 (4)	0.0027
O3		O3			O3		O3		
x	0.3619 (2)	x	0.3611 (2)	0.0008	x	0.3616 (4)	x	0.3614 (2)	0.0002
y	0.2494 (2)	y	0.2482 (2)	0.0012	y	0.2519 (3)	y	0.2490 (2)	0.0030
z	0.3100 (5)	z	0.3166 (3)	-0.0066	z	0.3200 (7)	z	0.3180 (4)	0.0020
Cation - oxygen bond lengths									
site T		T			T		T		
O3	1.575 (3)	O3	1.588 (2)	-0.013	O3	1.570 (4)	O3	1.590 (2)	-0.020
O1	1.629 (3)	O1	1.606 (2)	0.023	O1	1.620 (4)	O1	1.604 (2)	0.016
O2	1.648 (4)	O2	1.659 (2)	-0.011	O2	1.666 (6)	O2	1.662 (2)	0.004
O2'	1.686 (3)	O2'	1.676 (2)	0.010	O2'	1.689 (5)	O2'	1.683 (2)	0.006
Mean	1.635		1.632	0.002		1.636		1.635	0.002
M1		M1			M1		M1		
O3 x 2	2.012 (3)	O3 x 2	2.023 (2)	-0.011	O3 x 2	2.046 (4)	O3 x 2	2.035 (2)	0.011
O1 x 2	2.036 (2)	O1 x 2	2.042 (2)	-0.006	O1 x 2	2.054 (3)	O1 x 2	2.050 (2)	0.004
O1' x 2	2.104 (3)	O1' x 2	2.107 (2)	-0.003	O1' x 2	2.078 (5)	O1' x 2	2.115 (2)	-0.037
Mean	2.051		2.057	-0.007		2.059		2.067	-0.007
M2		M2			M2		M2		
O3 x 2	2.346 (3)	O3 x 2	2.345 (2)	-0.021	O3 x 2	2.327 (3)	O3 x 2	2.345 (2)	-0.018
O1 x 2	2.368 (3)	O1 x 2	2.367 (2)	0.023	O1 x 2	2.368 (5)	O1 x 2	2.364 (2)	0.004
O2 x 2	2.578 (3)	O2 x 2	2.537 (2)	0.041	O2 x 2	2.573 (4)	O2 x 2	2.548 (2)	0.025
O2' x 2	2.722 (4)	O2' x 2	2.729 (2)	-0.007	O2' x 2	2.713 (5)	O2' x 2	2.728 (2)	-0.015
Mean	2.504		2.495	0.009		2.495		2.496	-0.001

Special positions in the unti cell are given in italics. Parentheses give 1 σ of the final digit

Agreement parameters Grain 39 SXRD R1=0.038; PXRD Rp=6.0, Rwp=6.2, Dweighted=0.15, GoF=0.73, RBragg=3.6.
Grain 56 SXRD R1=0.046; PXRD Rp=11.2,Rwp=10.2, Dweighted=0.29, GoF=1.35, RBragg=5.0

Table 3

Method XRD CLSM* Host ion Eq15 **

Table 2: Major (wt%) and trace element (ppb) analysis of cpx and selected whole rock

wt%	Grain #39			Grain #56			Deeti Al-Di			Omphacite			Inagli -Di		
SiO_2	54.13			54.32			52.38			52.61			54.93		
TiO_2	0.13			0.04			0.97			0.18			0.08		
Al_2O_3	2.31			2.12			1.91			2.94			0.26		
Cr_2O_3	2.94			1.07			nd			0.01			0.61		
Fe_2O_3	nd			nd			0.472			1.52			n.d.		
FeO	2.21			1.62			4.25			5.59			1.19		
MnO	0.01			0.01			n.d.			0.06			0.05		
MgO	15.23			17.02			15.12			14.66			17.43		
CaO	19.37			22.59			24.13			21.19			24.54		
NiO	n.d.			n.d.			n.d.			0.03			0.03		
Na_2O	2.87			1.45			0.78			0.89			0.38		
K_2O	nd			nd			n.d.			nd			nd		
Total	99.2			100.24			100.00			99.67			99.5		

ppb	solution	LA	1σ	solution	LA	1σ	solution	LA (n=51)	1σ	solution (wr)	LA	1σ	solution	LA (n=30)	1σ
Sc				140815									54761		
Ga				2691									879		
Y	14851	8417	323	12746	8309	127	5256			17811	4839	71	4443		
La	41046	22625	299	6884	4605	94	12180	7023	536	2963	731	14	8948	8961	217
Ce	134387	74940	1104	47788	29213	298	28600	24889	1542	8158	3758	56	23849	24450	727
Pr	20029	10937	171	15257	9511	128	3905	4362	177	1354	793	18	3606	3678	113
Nd	83618	46801	967	93590	62023	659	16424	20937	846	7038	5099	63	16245	15902	515
Sm	15421	8511	182	15561	10437	182	3260	5123	266	2283	2007	28	3488	3479	130
Eu	4130	2205	50	4080	2647	71	959	1616	70	765	715	14	966	948	36
Gd	9159	4842	165	11417	6922	172	2644	4123	225	478	1851	49	2427	2291	91
Tb	998	489	17	1467	846	23	324	568	29	2813	283	9	259	264	11
Dy	4176	2281	84	5665	3787	108	1537	2800	171	3127	1454	52	1103	1107	47
Ho	648	346	11	574	337	12	246	441	32	712	228	7	175	174	8
Er	1398	714	28	626	374	16	517	1010	66	2054	461	12	402	422	18
Tm	169	89	4	36	27	1	59	112	8	311	52	3	57	58	3
Yb	927	523	25	131	71	7	339	610	45	1986	245	10	406	398	19
Lu	119	63	3	16	7	1	46	87	7	297	36	1	74	79	4

M2

Comparison of Ro given by different means of estimation

*This radius was calculated from the weighted mean of host ion radii

** This radius is obtained when using equation 15 Wood and Blundy (1997), which is not calibrated for M1.

Electronic Supplement to chapter 3

Table of Contents

Materials

Diopside from a potassic ultramafic complex

A single, gem quality, slightly chromian (Cr_2O_3 = 0.57±0.04) diopside from the Inagli Complex, Aldan Shield, eastern Siberia was provided for this study by R.H. Mitchell. Three distinctive types of gem quality diopside have been documented from metasomatic veins in this complex (Naumov et al., 2008). The studied crystal corresponds to the 'green diopside' variety. The entire crystal was cast in epoxy and then sliced with a micro-saw. One slice was polished and major element chemistry obtained on two perpendicular traverses by electron microprobe (EMP). The same slice was subsequently analyzed in situ for trace elements by laser ablation ICP-MS (LA-ICP-MS). A very small volume (less than 1 mm^3) of sample from between two laser ablation pits was physically removed. This was used for Gandolfi XRD analysis and the remaining material (1.9 mg) was digested for solution ICP-MS trace element analysis.

The bulk of the crystal remains for future analysis. The crystal appears homogenous with respect to both major and trace element chemistry.

Diopside from an alkaline rift complex

A single prismatic cpx phenocryst approximately 10mm x 10mm x 20mm from the Deeti melilitite, also provided by R.H. Mitchell, was characterized in this study. The Deeti melilitite, located at -2.811371 northing and 35.965118 easting, is a "ubehebe" type volcanic tuff ring, i.e., a cone on the order of 50 m in height comprised of alternating layers of lapilli and ejected bombs.

The mounting and analytical procedure was the same as for the Inagli Cr-diopside. The crystal showed little to no zonation as noted by previous investigations of similar material (i.e. Johnson et al., 1997) from this volcano. Although strictly classified as diopside, this sample was chosen based on the presence of an appreciable Tschermak component when normalized to six oxygen atoms. The bulk of the crystal remains for future analysis.

Eclogite hosted omphacite

Willard and Adams (1994) first reported eclogite-type material in the vicinity of Bakersfield, North Carolina, near the base of the Ashe Mountain Suite. A detailed mineralogical survey and interpretation of major element evolution with changing P-T conditions was presented by Page et al. (2003). The principal peak metamorphic minerals are garnet, clinopyroxene and quartz. Extraction of chemically homogenous clinopyroxene from this sample proved difficult for two reasons. First, there is retrograde hydration, which led to amphibole overgrowth. Second, there is a significant spread in preserved clinopyroxene chemistry. While all pyroxene has a low Ca-

tschermakite component, aegirine and diopside components are variable. The grains characterized

from the studied sample fall into the overlap between pro- and retrograde omphacite as defined in figure 3 of Page et al. (2003).

An attempt was made initially to characterize and extract clinopyroxene from a polished section. Combined EMP and LA-ICP-MS data for omphacite confirmed that major and trace element chemical variability is correlated. Compositional boundaries were found be quite sharp but very irregular in geometry and it proved impossible to extract suitable material from the remaining section after LA-ICP-MS analysis.

Eventually, we resorted to hand-picking individual clinopyroxene fragments from a mineral concentrate (provided by D.T. Tinkham) into an epoxy grain mount. All grains were studied for homogeneity in major element composition with EMP and from the suitable grains, the one lowest in Al (A_2O_3 = 2.94 wt.%) was selected as an indication of prograde nature. The trace element concentrations were obtained by LA-ICP-MS and a small fragment of the analyzed crystal adjacent to the laser pit was extracted for Gandolfi XRD analysis. The trace element composition of the whole rock was determined by solution ICP-MS.

Kimberlite hosted peridotitic chromian diopside xenocrysts

Mantle xenocryst clinopyroxene was obtained from kimberlite heavy mineral concentrates were provided by M. Seller. The criteria outlined in Nimis (2002) were used to screen the clinopyroxene based on major element chemistry to represent genuine peridotitic xenocrysts. Grains were classified by a two-stage scheme. In a first step,

Cr_2O_3 versus Al_2O_3 compositional space was used to select chromian diopside interpreted to have been derived from the on-craton garnet peridotite stability field (Ramsay, 1994). Second, when plotted in MgO-Al_2O_3 compositional space, clinopyroxene of peridotitic origin was distinguished as having greater than 18 wt.% MgO and more than 0.7 wt.% Al_2O_3. Rare-earth element data were obtained by LA-ICP-MS for a large number of classified grains. It was found that the vast majority of grains produced well-defined convex parabola in Onuma diagrams, similar to those established for typical kimberlite chromian diopside macrocrysts (e.g. Merry and leRoex, 2007). Grain #56 (ca. 3 mm diameter) was chosen to represent this dominant population. A subordinate population yielded slightly different REE patterns, with much less well-developed LREE limbs of the Onuma parabola. This difference will be discussed in detail later. Grain #39 (ca. 2.5 mm diameter) represents this latter population.

Both grains were studied in situ for major element (EMP) and trace element (LA- ICP-MS) composition. Small fragments (the smallest being 0.133 mg) of the remaining grains were also used for trace element analysis by solution ICP-MS. Equally, small fragments were used for Gandolfi XRD analysis. Finally, one small fragment of both grains was also subjected to single crystal XRD.

Table 3ES1 Rietveld Agreement Parameters

Parameter\Sample	BakEc*	Inagli	Deeti
R expected	11.21	10.90	4.29
R profile	5.53	8.02	2.19
R weighted profile	6.70	9.42	2.84
D statistic	0.15	0.30	0.08
Weighted D	0.17	0.34	0.08
Goodness of Fit	0.36	0.75	0.44
R-Bragg	5.55	4.84	1.75

*BakEc stands for Bakersville eclogite

Table 3ES2 Regression Parameters

M2 Site

Sample	Intercept	Slope	R^2	Elements excluded
Grain #39	2.37	-256.25	0.98	Ho, Er, Tm, Yb, Lu,
Grain #56	5.09	-736.036	0.99	Lu
BakEc	0.06	-389.26	0.99	Lu
Inagli	6.00	-292.65	0.98	Er, Tm, Yb, Lu, Sc
Deeti	-0.70	-319.00	0.99	Er, Tm, Yb, Lu

M1 site

Sample	Intercept	Slope	R^2	Elements included
Grain #56	5.85	-152.53	0.99	Lu, Sc, Ga
Inagli	8.98	-89.62	0.97	Er, Yb, Tm, Lu, Sc

References

Johnson LH, Jones AP, Church AA, Taylor WR (1997) Ultramafic xenoliths and megacrysts from a melilitite tuff cone, Deeti, northern Tanzania. Journal of African Earth Sciences 25(1): 29-42

Merry M, le Roex A (2007) Megacryst suites from the Lekkerfontein and Uintjiesberg kimberlites, southern Africa: evidence for a non-cognate origin. South African Journal of Geology 110(4): 597-610

Naumov VB, Kamenetsky VS, Thomas R, Kononkova NN, Ryzhenko BN (2008) Inclusions of silicate and sulfate melts in chrome diposide from the Inagli deposit, Yakutia, Russia. Geochemistry International 46(6): 554-564

Nimis P (2002) The pressures and temperatures of formation of diamond based on thermobarometry of chromian diopside inclusions. Canadian Mineralogist 40: 871-884

Page FZ, Essene EJ, Mukasa SB (2003) Prograde and retrograde history of eclogites from the Eastern Blue Ridge, North Carolina, USA. Journal of Metamorphic Geology 21(7): 685-698

Ramsay RR, Edwards D, Taylor WR, Rock NMS, Griffin BJ (1994) Compositions of garnet and spinel from the Aries diamondiferous kimberlite pipe, central kimberley block, western-Australia - implications for exploration. Journal of Geochemical Exploration 51(1):59-78 doi:10.1016/0375-6742(94)90005-1

Willard RA, Adams MG (1994) Newly discovered eclogite in the Southern Appalachian orogen, northwestern North Carolina. Earth and Planetary Science Letters 123 (1-4): 61-70

Chapter 3 appendix

Figure 3A1 Rietveld refinement of M1G14 garnet

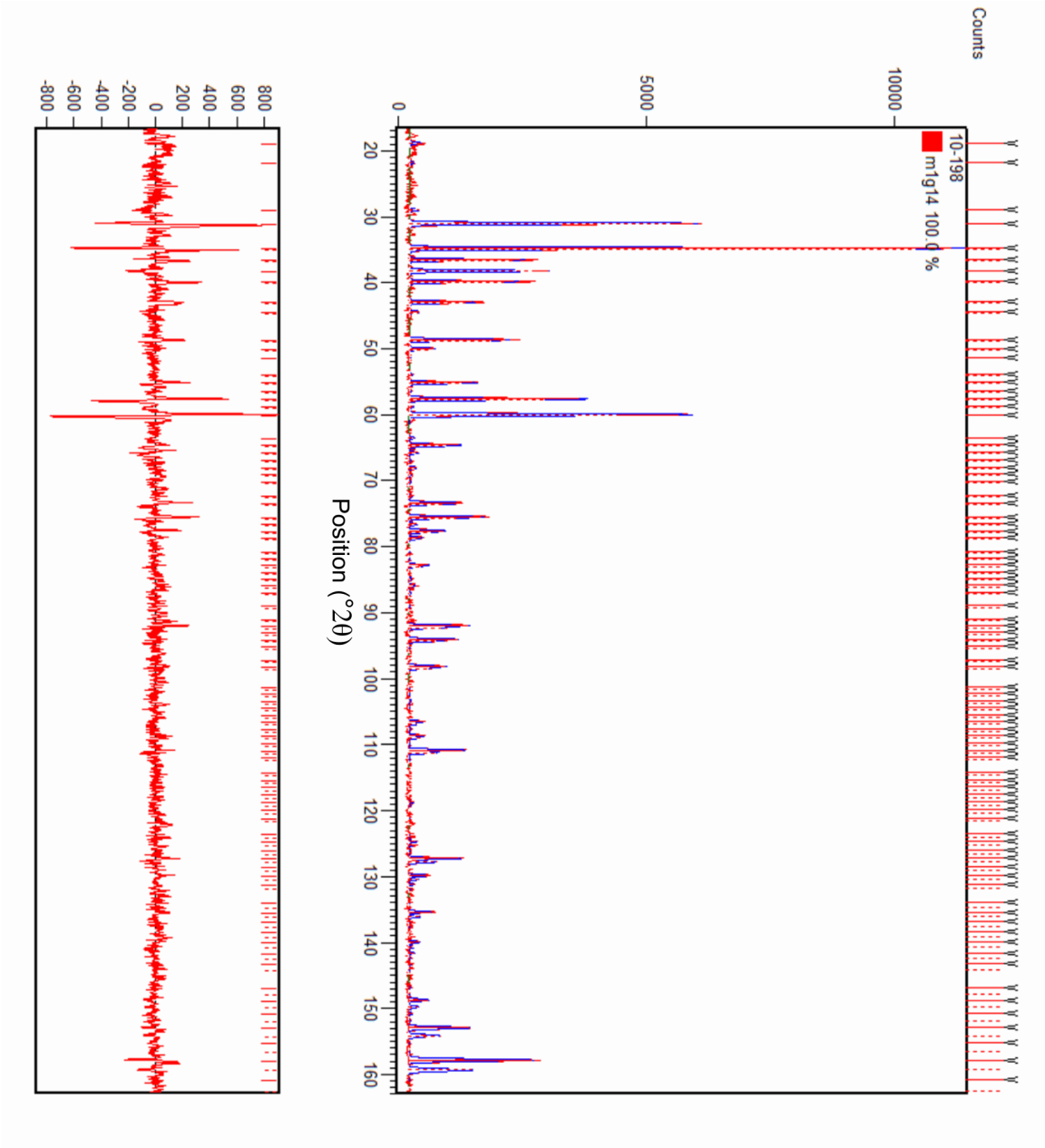

Table 3A1 XRD and trace element data for M1 G14 garnet

XRD data for M1 G14 garnet

Single Crystal			IP-DIIS		
			Zero Shift	0.0133	°2θ
a [Å]	11.532	0.0015	a [Å]	11.5367	0.0001
b [Å]	11.532	0.0015	b [Å]	11.5367	0.0001
c [Å]	11.532	0.0015	c [Å]	11.5367	0.0001
O1			O1		
X	0.0967	0.0001	X	0.0959	0.0003
Y	0.2005	0.0001	Y	0.2005	0.0002
Z	0.2837	0.0001	Z	0.2843	0.0002
U	0	0	U	0.0065	0.0007
V	0	0	V	-0.0121	0.0035
W	0.01	0	W	0.0959	0.0017
			n	0.03	0.02

Major element data wt%		Atoms based on 12 O	
SiO_2	41.36	Si	2.99
TiO_2	0	Ti	0
Al_2O_3	20.58	Al	1.75
Cr_2O_3	3.57	Cr	0.2
Fe_2O_3	0.788	Fe+3	0.04
FeO	7.092	Fe+2	0.43
MnO	0.37	Mn	0.02
MgO	20.57	Mg	2.22
CaO	4.54	Ca	0.35
Na_2O	0.02	Na	0
	98.89		

Calssified as Lherzolite (Schulze, 2006)

Trace element data (ppm)

Core	ppm	Rim	ppm
Li	0.118	Li	0.087
Be	0	Be	0
B	542.9	B	468.3
Sc	164	Sc	183.3
Ti	260.2	Ti	293.4
V	125.6	V	133.5
Co	35.98	Co	40.6
Ni	18.44	Ni	19.42
Rb	0.038	Rb	0
Sr	0.684	Sr	0.756
Y	1.947	Y	1.945
Zr	26.86	Zr	27.68
Nb	0.174	Nb	0.238
Cs	0.001	Cs	0.004
Ba	0.074	Ba	0.075
La	0.054	La	0.069
Ce	0.704	Ce	0.701
Pr	0.357	Pr	0.325
Nd	5.222	Nd	4.589
Sm	4.597	Sm	4.445
Eu	1.107	Eu	1.099
Gd	1.985	Gd	1.809
Tb	0.181	Tb	0.189
Dy	0.666	Dy	0.657
Ho	0.084	Ho	0.096
Er	0.211	Er	0.234
Tm	0.036	Tm	0.046
Yb	0.336	Yb	0.346
Lu	0.089	Lu	0.093
Hf	0.288	Hf	0.318
Ta	0.01	Ta	0.013
W	0	W	0.004
Tl	0.003	Tl	0.003
206Pb	0.018	206Pb	0.013
208Pb	0.015	208Pb	0.015
Bi	0.012	Bi	0.001
Th	0.011	Th	0.032
U	0.062	U	0.073

Table 3A2 Grain 39 solution data (ppb)

Run 1	Sample weight (mg)	0.26

Li	68	Er	108
Be	262	Tm	22
Sc	1450	Yb	216
Ti	190379	Lu	53
V	9702	Hf	106
Cr	687	Ta	9
Co	527	W	0
Ni	946	Tl	0
Cu	731	Pb via 206	425
Zn	38456	Pb via 207	443
Ga	536	Pb via 208	435
As	7	Th	13
Rb	56	U	2
Sr	74514		
Y	972		
Zr	16843		
Zr	16709		
Nb	2396		
Mo	10		
Ag	6		
Cd	40		
In	38		
Sn	51		
Sb	4		
Cs	1		
Ba	812		
La	2460		
Ce	6345		
Pr	843		
Nd	3098		
Sm	483		
Eu	145		
Tb	43		
Gd	308		
Dy	216		
Ho	40		

Chapter 4

An alternative explanation for sinusoidal REE patterns in peridotitic garnets with implications for the early Earth mantle structure

Kirk C. Ross[a,$], Andrew M. McDonald[a], Heath Bagshaw[b], Balz S. Kamber[c]

[a]Department of Earth Sciences, Laurentian University, Sudbury, Ontario, Canada

[b]Center for Microscopy and Analysis, Trinity College Dublin, Ireland

[c]Department of Geology, School of Natural Sciences, Trinity College Dublin, Ireland

[$]corresponding author mailing address: Department of Earth Sciences, Laurentian University, 935 Ramsey Lake Road, Sudbury, P3E 2C6, Ontario, Canada; (telephone: ++1 707 675-1151; fax: ++1 705 675-4898; email: kross@laurentian.ca)

Abstract

This study reports new data for kimberlite-derived peridotitic garnets that display sinusoidal REE patterns. LA-ICP-MS and EMPA analysis of a large number of grains revealed a continuum from "normal" garnet with HREE enrichment to highly sinusoidal REE patterns that have an unexpectedly high MREE content. Of all grains, 8% were truly sinusoidal (i.e. with a resolvable secondary apex over Nd-Sm), 44% were normal while the remaining 48% showed intermediate patterns. High-field-strength element systematics in the sinusoidal REE pattern garnets argue against metasomatic REE re-enrichment as do theoretical equilibration calculations with highly enriched mantle fluids or melts. The sinusoidal segment of the REE pattern in these garnets resembles an Onuma diagram. The first working hypothesis that was tested here therefore was whether these REE patterns might be an artefact of an undetected MREE-enriched inclusion phase. An exhaustive search on 18 of the most sinusoidal garnets using XRD, EMPA, LA-ICP-MS and TEM, however, suggested this not to be the case. The sinusoidal REE garnets are compositionally uniform on the scale of the electron beam interaction volume. Only 4 of 18 XRD patterns showed additional peaks at ca. 2.63 and 1.88 Å that could not be indexed on the garnet unit cell. These positions coincide with the orthorhombic perovskite (121)+(002) and (202) reflections. Having established that metasomatic re-enrichment is unsupported and that unidentified MREE-rich mineral inclusions are unlikely, an alternative working hypothesis was developed. This is founded on the observation that the sinusoidal REE pattern of these garnets can be generated if the single-phase garnets originated as bi-mineralic cumulates of Ca-perovskite (CaPv) and Mg-perovskite (MgPv) or CaPv and garnet. Experimental evidence of Oguri et al. (2000)

shows that upon decompression in the mantle transition zone, such bi-mineralic assemblages transform into a single garnet phase. According to this hypothesis, it is possible that the highly unusual REE patterns were inherited from perovskites and that the mantle xenocrysts could represent samples from magma ocean cumulates.

1. Introduction

A thorough understanding of the principles and dynamics that govern crystal-melt trace-element partitioning is fundamental to many aspects of the earth sciences and solid-state physics. Controls on the distribution of trace elements in minerals were initially proposed by Goldschmidt (1937) in what are commonly referred to as Goldschmidt's rules. Few major conceptual advances about mineral/melt partitioning of trace elements were made for several decades until a contribution from Onuma et al. (1967) showed a direct relationship between the radius of a substituent trace element and the crystal structure of the host mineral.

To quantify the behaviour of trace elements, the crystal-melt partition behaviour of trace-element i is modeled by its distribution coefficient (Di) given as: mineral concentration of i / melt concentration of i. Once considered constant, or only dependent on a single chemical parameter of the host mineral or melt (e.g. Mg# affecting D_{Ni} ol/melt; Hart and Davies, 1978) or a single dominant thermodynamic property (e.g. P on D_{Ni} ol/melt; Beattie et al., 1991) it is now widely agreed that D's are in fact thermodynamic parameters influenced by many variables (e.g. for the example of D_{Ni} ol/melt; Filiberto et al., 2009). These include: mineral composition, melt composition, temperature (T) and pressure (P) (e.g. van Westrenen and Draper, 2007). Appropriate D's must therefore be calibrated for any particular petrologic environment. In both high- and low-pressure

experiments designed to quantify silicate mineral-melt rare-earth element (REE) partitioning, mineral composition has shown to be among the most influential variables on apparent D's. Indeed, such a strong relation between mineral chemistry (and in turn crystallography) of garnet and REE D's was observed that an expression to predict Di based on the crystallographic structure determined from major element chemistry was formulated (van Westrenen and Draper, 2007). Clearly, any attempt at gaining a full understanding of the partitioning behaviour of trace elements into major mantle silicates such as garnet relies on a detailed investigation into the crystal structure.

The monomineralic grains studied here were collected from a heavy mineral concentrate and mounted in epoxy with no evidence of melt inclusions. Accordingly, the equilibrium melt composition was estimated using major element chemistry of the grains studied. Such classification (Schulze, 2003) revealed a peridotitic origin for all the grains selected for further analysis (table 1). We therefore chose CI chondrite (McDonough and Sun, 1995) to represent the composition of the whole rock in equilibrium with these garnets. For this reason, the values given here represent only apparent D's or normalized concentration (NC). Thus, throughout the present communication D refers to NC rather than to the true distribution coefficient. Nevertheless, normalizing the REE data to the carbonaceous Ivuna chondrite provides an adequate standardization such that the shape and sinuosity of the garnet REE patterns can be quantified. Discussion concerning the effects of different normalizations on the relative and absolute REE pattern for a variety of minerals can be found in Ross and Kamber (2012).

The cubic garnet with the general formula $X_3^{XII}Y_2^{VI}Z_3^{IV}O_{12}$ (where Roman numerals indicate coordination) is characterized by three crystallographically unique metal sites; X,

Y and Z. The 8-coordinated dodecahedral X-site gives the largest mean metal-oxygen (MO_8) bond length ranging from ca. 2.39 Å for grossular to 2.27 Å for pyrope. Its host cation provides the basis for classification (i.e. Fe, almandine; Ca, grossular; Mg, pyrope; Mn, spessartine). The extended X-ray absorption fine structure experiments of Quartieri et al. (2002) have shown the garnet X-site to be the principal site into which REE substitute in the garnet structure. The crystallographic evidence indicates that when occupied by a divalent cation, the cavity in this site is 1.01 Å (2.39 minus the O radius of 1.38 Å, Shannon, 1976) in grossular to 0.895 Å in pyrope. This is as small as or smaller in radius than the smallest REE (Lu^{3+} 0.977 Å; Shannon, 1976). The Y-site, typically occupied by Al (note that this is also the principal site into which Cr^{3+} and Fe^{3+} substitute), in isometric 6-fold octahedral coordination by O is volumetrically much smaller than the X-site with a mean Y-O bond length on the order of only 1.89 Å. After the radius of O is subtracted, this leaves approximately 0.51 Å. The Z-site is in tetrahedral coordination and is typically occupied by Si in rock forming garnets and, similar to the Y-site, based on the mean M-O bond length minus the radius of O (1.65 Å – 1.38 Å = 0.27 Å), is clearly too small to accommodate substitution of the REE.

For the overwhelming majority of garnets, these crystallographic constraints and the observed apparent trace element distribution are in agreement. Namely, resulting REE Onuma diagrams show a steady increase in apparent D's from La through to Lu. The agreement between crystal-chemical prediction and REE incorporation is so strong that it would be possible to approximate the normalized garnet REE pattern solely from crystallographic data. The consistently heavy-REE (HREE) enriched garnet patterns are

the foundation on which Sm/Nd and Lu/Hf garnet geochronology is successfully based. In other words, metamorphic garnets have consistently high Sm/Nd and Lu/Hf ratios.

However, on occasion, the observed REE pattern is very different from that predicted by crystallography. In crustal garnets, the reason for this mismatch often is the contribution of minute light-REE (LREE) or middle-REE (MREE) enriched inclusions, such as phosphates. These inclusions can now be chemically mapped by LA-ICP-MS (e.g. Ulrich et al., 2009). Another class of garnet with unusual and unexpected REE patterns is associated with kimberlites and diamond inclusions. The chondrite normalized REE pattern of these garnets is sinusoidal and, for the reasons discussed above, cannot be rationalized with the garnet structure. Recognizing this difficulty, it was proposed that metasomatic re-enrichment by oxidizing mantle fluids or melts was responsible for the MREE enrichment (Hoal et al., 1994; Stachel et al., 1998; Griffin et al., 1999; Wang et al., 2000). This is now the widely accepted model, which is of importance to diamond genesis, as such garnets have been found as inclusions in diamond.

Here we present an array of data, including chemical and structural, for garnets selected from a pool of grains extracted from kimberlite heavy mineral concentrates. Eighteen garnets were selected for XRD structural analysis based on the degree of sinuosity and location of the apex in the REE pattern. The purpose of the study was to test the currently accepted and alterative mechanisms that could result in the MREE enrichment in these otherwise anomalous garnet REE patterns by means of a multi-technique approach.

2. Materials and Methods

2.1. Materials

The material for all analyses in this study was provided by Michael Seller of DeBeers Canada Inc. – exploration division. Eighteen grain mounts (up to ~ 150 grains each) represented garnets from heavy mineral concentrates derived from Canadian kimberlites. The garnets were previously characterized in terms of their chemistry by means of industry-grade electron microprobe analyses (EMP) by wave-length dispersive spectroscopy (WDS; with a Cameca SX 100 at the DeBeers analytical facility in South Africa). Unfortunately, the major element data did not include errors and therefore errors are reported only for the analyses performed by the authors (trace elements, XRD, etc.). Major element data were used for classification and for normalizing the trace element analyses. All grains were analyzed for REE and assorted trace elements. Upon completion of the REE analysis, grains with unusual normalized REE patterns were selected for XRD analysis and further experiments.

2.2. Methods

The analytical methods cover a variety of aspects of garnet properties. Some analyses were destructive. These were typically conducted on a small fragment of the grain or only consumed a part of the grain exposed in the mounts.

2.2.1. Laser ablation inductively-coupled-plasma mass-spectrometry (LA-ICP-MS)

Trace-element data were obtained in situ by ultra violet UV LA-ICP-MS using a Supercell^{TM} equipped NewWave^{TM} Nd:YAG 213 nm laser coupled to a ThermoFisher^{TM} X SeriesII quadrupole ICP-MS. Polished grain mounts were ablated in 99.9995% pure He carrier gas (ca. 0.5 l min^{-1}), which was mixed immediately down-stream with Ar (0.8 l

min^{-1}) to ensure efficient aerosol transfer (e.g. Kamber, 2009). Where possible, a 100 µm spot size was used and the laser was fired with a repetition rate of 10 Hz. Fluence was kept constant at 11 $J \cdot cm^{-2}$. All areas were pre-ablated by three pulses with a 130 µm spot size with similar settings. Total analysis time was 70 s, consisting of 30 s background acquisition, 25 s of ablation, and the remainder (15 s) being washout. The synthetic glass standard NIST612 was used for calibration with Ca (as determined from the EMP) as the internal standard (e.g. Heinrich et al., 2003). Data quantification was performed with the Iolite software (Hellstrom et al., 2008). At the beginning of the study, the well-characterized ICP-MS standard (BHVO2g, Gao et al., 2002) was interspersed among sample analyses to test for accuracy and precision. The resulting 23 secondary standard analyses yielded a mean accuracy of 9.8%. The precision was always better than the accuracy determined from the standard comparison.

On four selected highly sinusoidal garnets, very detailed surface trace element maps were also generated using the approach of Ulrich et al. (2009). The data were gathered with the same mass spectrometer as the conventional spot analyses but the samples were ablated with a Resonetics M-50 ablation device equipped with a two-volume sampling cell. Operation parameters were similar to those reported in Petrus and Kamber (2012). The laser spot-size was reduced to 8 µm. Previous mapping efforts (e.g. Ulrich et al., 2009; Webb and Kamber, 2011) showed that this method is capable of detecting inclusions smaller than half the beam size if they had distinct trace element content. To facilitate detection of the exceedingly weak signal generated by an 8 µm spot, we measured the minimum of REE to detect a sinusoidal REE pattern, chose those REE with a positive Oddo-Harkins effect and extended the dwell-times to 250 ms.

2.2.2. Electron microbeam analysis

The industry-standard EMP data provided by DeBeers inc. contained concentration measurements for Si, Ti, Al, Cr, Fe, Mn, Mg, Ca, Na, K and Zn. These were used to classify the garnet material based on the scheme proposed by Schulze (2003) and for internal standardization of the LA-ICP-MS data.

On grains selected for further study based on the trace element data, compositional homogeneity investigation was carried out in two ways. First, on a JEOL 6400 x scanning electron microscope (SEM) equipped with an OXFORD INCA X-site energy dispersive X-ray (EDS) detector operating with a beam current of 1 nA. Second, on a Cameca SX100 EMP, operating at 20Kv for all elements with counting times of 20 s for Si, Al, Mg, Fe; 30 s for Cr and Ca; 40 s for Mn and 60 s for Ti and Na.

2.2.3. Etching

To test for the presence of possible mineral inclusions in garnets that showed highly sinusoidal REE patterns, the exposed polished puck surface was etched in boiling HF (50%) vapour. It was expected that the Cr-pyrope would remain relatively less affected by HF vapour, given that successful digestion of garnet for isotope or chemical analysis requires the use of high-P Parr bombs operated at a temperature of at least 180ºC. It was speculated that included silicate phases, such as pyroxenes, would preferentially dissolve and leave a visible etch pit. Initial experimentation was required to establish that exposure between 15 and 30 minutes resulted in the best compromise between etching and complete destruction of the polished surface. After exposure to the HF vapours, the puck was placed in an ultrasonic bath filled with ultra-pure water for 15 minutes, carbon coated and observed under the SEM.

2.2.4. X-ray diffraction

XRD analyses were conducted on minute samples extracted next to the laser ablation pits. Powder X-ray diffraction data were obtained with a 114.59 mm Gandolfi camera. The camera was equipped with a 0.3 mm pin-hole collimator and rotary vacuum pump capable of achieving an absolute pressure of 0.03 atm. X-radiation was generated by a Phillips 1710 diffractometer emitting Ni filtered $CuK\alpha_1$ + $CuK\alpha_2$ radiation (average wavelength 1.1564 Å) with operating conditions of 40 mA and 30 kV. XRD experiment times ranged between 4-10 h. For X-ray detection a $BaFBr:Eu^{2+}$ FUJITM SR-type image plate (IP) was used. Equigranular monocrystalline garnet fragments were affixed to the end of a tapered glass-fibre (100 drawn to 15 μm diameter) using fingernail hardener. The grains had a total volume of ≈ 200 μm^3. To improve the overall quality of the XRD patterns in terms of the continuity of the Debye rings and to reduce the likelihood of systematic extinctions, in some cases (grains 039_6_152,039_ 6_141 and 039_6_129) a single garnet fragment was gently crushed between two glass slides to give multiple (~20) subgrains that were then mounted as described above. Based on their unusual REE patterns, 18 garnet grains were submitted to XRD experimentation.

The principal steps of data integration to achieve conversion of image plate data to a fully quantitative digital diffractogram are outlined in Matsuzaki and Shinoda (2004). The software used for the conversion of an IP diffraction image to a full-profile digital diffractogram was developed in house (DIIS; Petrus et al., 2011) and was tested for accuracy with standard materials by Ross et al. (submitted). The data given by this XRD technique yield a fully quantitative digital diffractogram from a single (or gently crushed to subgrains) fragment roughly 50 μm in diameter.

2.2.5. Transmission electron microscopy (TEM)

A single garnet grain that showed some of the most sinusoidal REE pattern and that also showed evidence for pits after HF etching was selected for TEM analysis completed at the Centre for Microscopy and Analysis, Trinity College Dublin. A randomly selected slice of sample was obtained in the following manner. The sample was sputter coated with 10 nm of Au using a Cressington 108 auto sputter coater. A Carl Zeiss Auriga focused ion beam (FIB) was used for TEM specimen preparation. A protective layer of platinum was deposited on the region of interest, by electron beam induced deposition. The sample was then thinned to approximately 1 micron by the FIB, undercut, and transferred to a Cu omniprobe TEM sample holder with an in-situ micromanipulator. Finally the specimen was thinned to electron transparency, by FIB, with the final polishing step performed at 20 pA beam current. Electron diffraction analysis was performed using a JEOL 2100 TEM fitted with a LaB_6 Filament operating at 100 kV and utilizing a JEOL double tilt holder (model EM-31640) to facilitate sample movement to obtain Zone Axis Diffraction Patterns (ZADP). Diffraction pattern images were recorded using an AMT CCD camera bottom mounted to the instrument.

3. Results

3.1. Major element chemistry

The first step of this study was to investigate the nature of these unusual garnets and to test whether there was a correlation between the REE patterns and the petrogeneses of the garnets as inferred from classification. In total, the major- and trace-element chemistry of over one thousand garnet grains was studied. When classified according to the scheme proposed by Schulze (2003) the following approximate distribution emerged: 70%

lherzolite-type, 21% harzburgite-type, 3% megacryst-type, 3% eclogite-type (2.0% group A, < 1% group B and C), < 1% crustal, and < 1% wherlitic. The majority of grains analyzed plot within the peridotitic region close to the lherzolite-harzburgite boundary, either falling just above (lherzolite) or below (harzburgite). The peridotitic garnets range in Mg # (Mg/(Fe+Mg)) from 0.7 - 0.8. Confidentiality agreements prevent the graphical display of such data.

3.2. Trace element chemistry LA-ICP-MS

About 1% of the grains analyzed by LA-ICP-MS were either smaller than the volume sampled by the laser (resulting in a signal dominated by trace elements in the epoxy) or badly fractured and contained material characteristic of the host kimberlite. These data were considered spurious and were excluded from the sample population. Trace element analysis of the remaining garnets revealed a continuum of trace element patterns between two end-members (illustrated on figure 1). One end-member, which constitutes 44% of the grains, represents the normal garnet pattern with a positively sloping normalized REE pattern (figure 1a). Almost half the garnets (48%) occupied a progression from normal garnet patterns exemplified by HREE enrichment with a smooth positive slope approaching Lu to garnets that show pronounced enrichment in the MREE. Developing from a normal garnet pattern, the progressive increase in the MREE component, a slight trough develops around Er giving rise to a secondary apex around Gd (figure 1b). The other end-member (8%) consists of a highly sinusoidal REE pattern with two points of inflection (1c). The LREE show a positive progression with increasing atomic number (Z) to a maximum located around Nd, where the REE dip to a negative trend to a trough around Er. Together, the positive LREE with the negative trending MREE distributions

give rise to the sinusoidal segment of the REE diagram. With increasing Z, the HREE revert to a very steep positive trend (figure 1c), much steeper than that of a normal garnet. With increasing sinuosity, the apex shifts to larger radii while the HREE develop a depleted signature with dramatically increasing Lu/Yb ratios. Clearly, there is a continuum but a sufficient number of grains were identified for the two well-developed populations: garnets with a secondary apex over Nd, representing the most sinusoidal garnets and normal garnets.

An attempt was made to test whether the REE systematics of the garnet population correlated with other major or trace element characteristics. We note that a correlation between MREE enrichment and Ca content was recently observed in diamond inclusion (DI) garnets by Richardson et al. (2009). These authors found that DI garnets could be classified into low, intermediate, high and very high Ca content. By separating the garnets into these groups, Richardson et al. (2009) found that Sr content anti-correlated with Sm/Nd and Nd isotope composition. The normal, high Sm/Nd garnets have low Sr and highly radiogenic Nd while the low Sm/Nd (and hence likely sinusoidal) garnets have unusually high Sr, low Sm/Nd and correspondingly unradiogenic Nd isotopes. In our much larger dataset, no such correlations were found, which we attribute to the fact that the present study investigated samples from multiple sources, whereas Richardson et al. (2009) studied exclusively DI garnets from a single kimberlite.

3.3. Etching experiments

Etching experiments were conducted on 6 mounts, of which three showed development of sufficiently deep etch pits without excessive damage to the polished surface of the garnets while the remaining grains were either exposed to the HF vapor for an

insufficient amount of time to have an effect on the included phase(s) – or exposed to HF to such an extent that their surfaces were digested. SEM images showed that the majority of garnets had euhedral, prismatic cavities caused by the HF exposure. Shown in figure 2 are residual etch pits observed in peridotitic garnet 1435_5_33 (2a) and 1335_28_70 (2b). Three observations are striking. First, there is apparently a random orientation of the cavities, which typically measured a few microns in diameter. Therefore no preferred crystallographic orientation can be attributed to the etched phase and therefore exsolution of more HF-soluble phase along the garnet's symmetry planes was excluded as an explanation. Second, based on the macro-molecule unit-cell relationship at least some of the etch pits show the dissolution of a phase with lower than cubic symmetry (figure 2b) and clearly not compatible with a high-symmetry phase such as garnet. They are unlikely to represent a crystallographically controlled advance of HF-etching into actual garnet. Rather, owing to the resilience of garnet to HF, they are interpreted as preferentially etched inclusions of a phase less resistant to HF. Third, whereas all garnets with sinusoidal REE patterns showed etching, apparent low-symmetry cavities were also found in garnet with normal REE patterns.

3.4. Electron microbeam analysis

After discovery of the etch pits, several grains were re-polished and subjected to micro-beam analysis. Under BSE, no inclusions were evident. Detailed X-ray maps and long, randomly-spaced EMP traverses were performed next. The most detailed of these were conducted on two re-polished, highly sinusoidal garnets with the most euhedral etch pits. No compositional deviation was detected. As an example, a traverse path on a garnet is shown in figure 3 as a dark sub-horizontal band where the carbon coat was modified by

the electron beam. Of the 225 individual spots comprising the traverse, Si varied by no more the 0.15 wt.% while all remaining elements varied by less than 0.09 wt.%. The profile for Al, Cr, Ca and Mg are shown in figure 3. Minor deviations can be observed but there is a clear absence of evidence for a compositionally resolvable included phase different from garnet. This could mean one of three things: first; the etched phase is isochemical with garnet; second, the excitation volume of the electron beam was too large to detect the inclusions; third, the etched phase was the garnet itself. The second explanation seems highly implausible given that the etched cavities are at least 1 micron but often 3-4 microns in dimension.

3.5. XRD

Judging from the density of etch pits, it was anticipated that the included phases should make up at least 1% if not 2-4% or more of the 'garnet'. The employed XRD technique is particularly well suited for the investigation of modifications of the garnet structure or the presence of additional crystalline phases. Simultaneous 2-D detection of X-rays by the image-plate (IP) over nearly the entire 2θ range (~5-165 °2θ, Co $K\alpha_{average}$) not only permits detailed structural resolution of the host garnet through Rietveld structural refinement, but also the opportunity to observe diffraction peaks that are not attributed to the garnet structure. Since any additional non-garnet peaks are the focus of the XRD studies, and because such peaks may be very weak in relative intensity, the garnet grains were left to “soak” in the X-ray beam. This led to the saturation of the strongly diffracting garnet lines on the IP but permitted the detection of weak diffractions arising from any included crystalline material. Eighteen sinusoidal (16 lherzolitic and 2 harzburgitic) grains were analyzed. Only four of the 18 grains showed evidence of a

phase present in addition to garnet. Two patterns showed a single peak that cannot be indexed on a garnet unit cell (space group Ia-3d, a = 11.5483(1) Å) with a d-spacing around 4.143(2) Å and ~14% relative intensity of the 100% garnet peak (024). Figure 4 shows XRD analysis of 039_6_129 in red overlain by the calculated garnet structure (blue) as given from the Rietveld refinement. Peaks at 2.630(2) Å and 1.886(3) Å with intensities about 14% and 10% of the garnet 100 peak respectively that cannot be indexed on a garnet unit cell.

A search-match analysis is difficult, if not impossible on only one superfluous stand-alone peak. Nonetheless, we searched the ICDD database for a single phase that had only one strong peak at d-spacing of either 4.143 Å or 2.630 Å with any other peak associated with the included phase either overlapping with the diffractions attributed to the garnet structure or so weak in relative intensity that they would not be detected by the IP. The peak at 4.143 Å could be indexed as the cristobalite (111) on a cubic unit cell (Fm-3m, a = 7.1689(1) Å). Cristobalite could have formed from a high P polymorph of quartz during the kimberlite eruption. However, traverses showed no significant deviation in major element chemistry from a homogenous garnet composition on the scale of analysis (1 μm spot). Its structure strongly excludes cations like the REE and it is therefore not a likely candidate as an included phase.

The peaks at 2.630 and 1.886 Å could be successfully indexed as the (121) + (002) and the (202) on an orthorhombic perovskite unit cell (Pnma, a=5.343 Å b=7.508 Å c=5.360 Å). Calculation of a diffraction pattern based on the perovskite structure with these cell dimensions shows that these two peaks [the combined (121)+(002) and the (202)] are among the three most intense peaks. The third, (123)+(321), overlaps with the strongly

diffracting garnet (246) at d-spacing of roughly 1.53 Å and is therefore difficult to quantify.

In summary, XRD analysis revealed that over 75% of the garnets analyzed were homogeneous single crystals, despite the sinuosity of their REE pattern. The presence of the occasional superfluous peak in the XRD pattern does not constitute sufficient evidence to suggest that these anomalous REE patterns are the consequence of an included MREE enriched phase. Therefore the XRD results indicate that the sinusoidal REE pattern does not result from the inclusion of a solid phase that can be detected by this XRD method.

3.6. Trace element mapping

Of the four samples whose surface distribution was mapped for selected REE using LA-ICP-MS it was found that in sample 039_6_129, the MREE were not homogenously distributed, while in the three others they were. In this one sample there appear to be areas of elevated MREE content (see figure 5). Shimizu and Sobolev (1995) reported 'islands' of strongly enriched Sr content in Mir kimberlite DI garnets but their ion-probe data did not produce complete maps of grains and no superimposed map s of Sm/Nd. In the present study, combined mapping of Sm, Gd and Sr did not reveal a correlation between the concentrations of MREE and Sr. This lack of correlation cannot be an artefact of the extended dwell-times because the scan speed of the laser was 2 μm s^{-1}, providing sufficient dwell time for all the measured masses to sample areas on the scale of 2 μm.

3.7. TEM characterisation

Electron diffraction patterns were obtained on suitably oriented areas of the focused ion beam (FIB) -generated lamella. The bottom mounted AMT CCD camera of the TEM was used to understand the crystallographic orientation of the lamella and to scan for unexpected reflections. The entire electron diffraction pattern can be explained by the garnet structure with no indication of an additional phase. Figure 6a shows the electron diffraction pattern of the garnet in a [111] orientation. Figure 6b shows the corresponding garnet crystal structure in the same orientation as in 6a. All diffraction spots present could be accounted for by the garnet host with no indication of additional phases.

4. Discussion

There are several possible explanations for the development of the sinusoidal REE patterns in garnet. The three most obvious are discussed here in the following order: (1) modification of an originally typical garnet pattern by metasomatic re-enrichment (i.e. the conventional explanation); (2) the presence of an included phase in garnet; and (3) inheritance of a REE pattern by garnet that isochemically recrystallized after a different precursor parental phase(s).

4.1. Metasomatic modification

Among the first to report sinusoidal REE patterns in garnet with anomalous MREE enrichment were Shimizu and Richardson (1987). Since then, many others have noted a similar REE pattern in garnet brought to the surface by kimberlites (e.g. Nixon et al., 1987; Hoal et al., 1994; Griffin et al., 1999; Stachel et al., 2004). Most authors have attributed the sinusoidal REE pattern to varying degrees of metasomatic alteration or re-

equilibration with LREE enriched metasomatic fluids/melts (Shimizu and Sobolev, 1995; Stachel et al., 1998; Griffin et al., 1999; Wang et al., 2000; Burgess and Harte, 2004).

Stachel et al. (1998) suggested a multi-stage tectonomagmatic trace-element depletion followed by a LREE re-enrichment process. Accordingly, the host peridotite was first exposed to a polybaric melt depletion event that occurred in both the spinel and garnet stability fields giving rise to the steep slope among the HREE of the garnet (e.g. Lu/Yb >1.3). Second, garnets (and only garnets, as MREE enrichment has not been observed in any other peridotitic minerals) were then selectively re-enriched. After exposure to highly fractionated LREE of the metasomatic agent, these garnets were postulated to have ended up with sinusoidal REE pattern due to preferential later diffusional loss of the LREE over the MREE. However, experimental diffusion studies for garnet (van Orman et al., 2002; Tirone et al. 2005) show that diffusion coefficients of the REE in garnet differ imperceptibly and that the diffusivity of REE is in no way related the mineral/melt partition coefficient (D_{REE}). With the benefit of the insight from diffusion studies published since the Stachel et al. (1998) model, it appears that the only remaining mechanism by which garnets may acquire the sinusoidal character is by re-equilibration with a melt/fluid enriched would be if that fluid itself were selectively vastly enriched in the MREE, rather than the LREE. These could possibly have been pervasive percolating CHO fluids but this assumption is ad hoc. Stachel et al. (1998) acknowledged that REE transportation properties of the hypothesized fluids remain unknown.

It is straight-forward to illustrate the issue of re-enrichment in MREE only. All known highly-enriched alkaline or carbonatitic melt products (e.g. kimberlite, lamprophyre, carbonatite) show extreme LREE but not MREE enrichment. Figure 7 shows a REE

pattern calculated for an originally ordinary mantle garnet (D's from Zack et al. 1997) that equilibrated with a highly fractionated carbonatitic melt (from Keller and Zaitsev, 2006). The comparison with the original garnet and a sinusoidal garnet from the present study shows that whereas a slight hump around Gd develops with normalization to a LREE enriched carbonatitic melt, the degree of sinuosity and location of the apex never approaches similarity to a sinusoidal garnet.

A further way of testing interaction with metasomatizing fluids is to explore whether the high-field-strength-elements (HFSE) show CHArge and RAdius Controlled (CHARAC) behaviour where the trace element substitution is controlled by the charge and radius of the substituent cation (and lattice site), or whether these ratios deviate strongly from prediction due to fluid interaction (e.g. Bau 1996). Garnets that interacted with fluids and highly fractionated melts are expected to have Y/Ho and Zr/Hf ratios different (typically lower) than the chondritic ratios (see also Veksler et al., 1998). A plot of Y/Ho versus Zr/Hf ratios in the garnets studied here is found in figure 8. Comparison with the CHARAC field illustrates that these elemental ratios show no indication for the garnets having equilibrated or reacted with metasomatic fluids or melts. Furthermore, a Y/Ho versus Zr/Hf plot neither discriminated between the different parageneses of the garnets studied here (i.e. megacryst, lherzolite, harzburgite etc. garnets plotted on identical Y/Ho vs. Zr/Hf trends) nor among the different types of REE patterns.

In summary, the metasomatic fluids responsible for the sinusoidal REE pattern in these garnets likely represent a very low degree of partial melting or a residual fluid phase from a highly fractionated magma. Such melts are strongly LREE>MREE enriched and typically give rise to a non-CHARAC signature (Bau, 1996). Since these sinusoidal

garnets (table 1) show no significant deviation from CHARAC behaviour, it appears that a metasomatic origin for the smooth sinusoidal shape of these mantle garnets is not yet supported by experimental and empirical evidence.

4.2. Inclusions

The observations of residual etch pits left from exposure to HF vapour (shown in figure 2) suggested the possibility that the sinusoidal REE pattern might be an artefact of an included phase, such as for example cpx, which typically is MREE enriched. Trace element studies on eclogitic garnet have shown that the garnet REE pattern can in fact show a composite REE pattern from both the host garnet and an included phase such as cpx (Harte and Kirkley, 1997). For this reason, an exhaustive investigation was conducted in this study with the aim of locating and characterizing the inclusions using XRD, SEM-EDS, EMP, LA-ICPMS, and TEM. It was hypothesized that the inclusions should show up as compositionally and/or crystallographically material distinctive from garnet. However, in spite of an exhaustive effort (detailed EMP WDS traverses, IP XRD and TEM) no conclusive evidence for included phases was found other than the cristobalite and possible perovskite described earlier in the XRD results.

In one of four carefully mapped garnets, the MREE were apparently enriched in small areas that could represent inclusions. However, prior SEM analysis did not reveal major element evidence for chemically distinct inclusions. As a final test of whether the more easily HF-etched material could be the host of MREE, two differential digestion experiments were designed. First, ca. 100 µg grains of sinusoidal garnet fragments were ground in agate and the resulting powder was subjected to a 2 hour leach in cold 50% HF. The acid was transferred to a separate vessel and the remaining garnet digested at high P

and T with full strength HF and HNO_3. Both fractions were analyzed separately by solution ICP-MS according to the procedure detailed in Ross and Kamber (2012). The analyses did not yield absolute concentrations on account of the unknown mass fractions but the REE patterns had identical shape. Second, a polished garnet was placed face down in 50% warm HF for 20 minutes and the resulting acid was then dried down, converted and analyzed. Its REE pattern was identical of that obtained by LA-ICP-MS. Importantly, the pattern of the leachate also had the strong HREE enrichment.

The results from XRD experiments combined with those from the HF leach experiments show the presence of some occasionally included foreign crystalline materials. Although extra lines in the XRD spectra may be related to the etch pits in the few samples where they were found, there is a majority of sinusoidal garnets that show no evidence for inclusions at all. These observations lead us to conclude that in most garnets the sinusoidal REE pattern is not caused by inclusions. In discussing global compilations of REE in peridotitic garnets, however, the possibility needs to be entertained that not all garnets owe their sinusoidal REE pattern to the same process.

4.3. REE pattern inherited from a precursor mineral.

Since neither the metasomatic model nor the inclusion observations provide acceptable explanations for the sinusoidal shape of the observed REE patterns, we next explore a working hypothesis that breaks with the traditional view. Namely, using Cr as a proxy for melt depletion of the source rock, it is widely assumed that garnets commonly associated with kimberlites originated in the garnet stability field of the upper mantle that had been subject to prior melt depletion (e.g. Stachel et al., 2004). In other words, these garnets are

widely viewed as having derived from the asthenospheric mantle above the mantle transition zone, since they lack a majoritic component.

The working hypothesis advanced here explores whether they could have been derived from much greater depth, i.e. in the transition zone or even the uppermost lower mantle. High pressure experiments on Ca- (Greaux at al., 2011) and Mg-rich garnets (Irifune et al., 1996; Oguri et al., 2000) show that at pressures corresponding to the transition zone and uppermost lower mantle, garnet progressively exolves cubic Ca perovskite (CaPv), followed by a CaPv + an orthorhombic Mg perovskite (MgPv) + stishovite, respectively. In other words, in the absence of pyroxene, garnet can undergo an isochemical transformation to perovskite without developing a majoritic component. Significantly, the experiments of Oguri et al. (2000) show that these transformations are not restricted to pure end-members. These authors used natural garnet ($(Mg_{0.733,}\ Fe_{0.173,}\ Ca_{0.110,}\ Mn_{0.004})_3\ (Al_{0.924,}\ Cr_{0.030,}\ Ti_{0.015})_2\ Si_{3.011}\ O_{12)}$) not dissimilar in composition to those studied here (table 1) and showed complete regressive transformation from the high pressure and temperature phases back to garnet.

Thus, it is at least theoretically possible that the phase now observed as a single garnet could have originated as a bi-mineralic rock of two perovskites (CaPv and MgPv) or a perovskite-garnet combination (Gasparik and Hutchison, 2000).

It is important to note that such hypothesized rocks in the uppermost lower mantle or the transition zone would not have had a primitive mantle bulk composition. Rather these phases could, for example, have existed in the mantle as cumulates from the post-Moon forming magma ocean. If the existence of such cumulates is accepted as a possibility, their path towards single phase garnet is not complex. Namely, eventual and possibly

protracted exhumation from the lower mantle or transition zone to the upper mantle would have enabled the perovskitic phases to undergo a sub-solidus phase transformation to garnet. Owing to the isochemical nature of this transformation (e.g. $(X_{0.75}\ Al_{0.25})\ (Si_{0.75}\ Al_{0.25})\ O_3$ perovskite $\leftrightarrow X_3\ Al_2\ Si_3\ O_{12}$ garnet , where X is Mg or Ca) it requires neither additional phases nor the development and exclusion of additional phases. As a result, the daughter mineral (garnet) would inherit the trace element characteristics of the parent minerals.

Experimental studies have shown that CaPv hosts the majority of the large ion lithophile elements (LILE) and incompatible elements in the lower part of the transition zone and uppermost lower-mantle (e.g. Corgne et al., 2005). We next explore whether the sinusoidal garnet REE patterns could have originated as a combination of CaPv and MgPv cumulates.

Discussion of the details of REE distribution in the hypothesized precursor minerals and reverted garnets requires a brief review of the influence of the crystal structure and the lattice strain model on the apparent and actual Ds. When shown in a spidergram of atomic number versus D, it is difficult to visualize the influence of the crystal structure on the partitioning of trace elements (figure 9a). Onuma (1967) was amongst the first to show isovalent trace-elements according to their ionic radius of Ri on the ordinate against the LnD of cations, an inverse near-parabolic distribution emerges. Commonly referred to as an Onuma diagram (figure 9b), this plot shows the propensity of a crystal-lattice-site to incorporate isovalent cations whose radii slightly differ. The apex of the Onuma diagram represents the Ln of the maximum D (Do) of a fictitious cation whose radius is ideal (Ro) such that it has strain-free admittance to the lattice-site. Isovalent cations with radii larger

or smaller than Ro must do work on the surrounding lattice (Brice, 1975; Blundy and Wood, 1994; LaTourrette et al., 1995; Blundy et al., 1998). Thus, the strain-energy penalty induced by misfit cations, whether the cation is larger or smaller, invariably give Di's less than Do. The near-parabolic inverse relationship between Ri, and Di was formalized in a parameterization given by Brice (1975), who showed the relative D for misfit cations quantified into a radius parameter. Given as equation 1, the radius parameter (Rp) increase in positive value based on an exponential relationship of the absolute difference in radius between a misfit cation and one of Ro.

$$Rp = Ro/2(Ri-Ro)^2+1/3(Ri-Ro)^3 \quad \text{Eq 1}$$

where Ro is the ideal radius for the crystal site and Ri is the radius of a misfit cation. The Onuma diagram is asymmetrical in that it shows greater general admittance for cations smaller than Ro than for those larger; an artifact of the crystal lattice that stresses the importance of the second term in the Brice formulation. This equation is useful to model the relationship between the parameter Ro, which implies an integral crystallographic component, and the apparent D.

Figure 9c shows the collinear array that emerges when the radius parameter given from a correct choice of Ro is plotted against the natural logarithm (Ln) of D. This permits the derivation of Ro from measured D's though a non-linear least-squares regression towards unity of the correlation between the Rp and LnDs for elements that occupy the site of interest. Cations opposite the apex of the Onuma diagram permit a very precise derivation of the apex through this line of best-fit (figure 9c). Informally referred to here as a Brice diagram, the y-intercept in figure 9c gives LnDo while the slope is related directly to the susceptibility of the lattice site to incorporate misfit cations. The slope represents a point

on a univariant line in P-T space where the slope is maintained with a change in either P or T so long as the corresponding change is made in the other variable. This is easily envisaged by considering that increasing temperature will result in increased site elasticity so the limbs in the Onuma diagram will show a corresponding decrease in tightness while an increase in confining pressure contributes to greater limb tightness. With the benefit of having reviewed the Brice diagram, it is straight-forward to test how the sinusoidal garnet REE pattern could have originated. Figures 10a shows the Onuma REE patterns for garnet (open squares) and cpx (solid circles) respectively while 10b shows their respective Brice diagrams (symbols as in 10a). Figures 10c and 10d show the overall REE pattern with 10% and 20% cpx included in the garnet structure, respectively. In order to obtain REE patterns for these proportions we first fitted the cpx and garnet REE patterns with Onuma diagrams. We then normalized the observed D for each element to Do. Finally we added the two normalized patterns in the proportions of 90% garnet – 10% cpx and 80% garnet – 20% cpx in figures 10c and 10d. Two noteworthy features include the lack of steep HREE enrichment typical of sinusoidal garnets and that the limbs in the Onuma diagram attributed to the included cpx do not show the same degree of tightness as the sinus in these anomalous garnets. This is because the M2 site in cpx (the principal site on which REE substitute) has sufficient elasticity to readily admit misfit cations and therefore gives rise to an Onuma diagram with gently sloping limbs or a Brice diagram with a less steep slope than that observed in the sinusoidal garnets. It is thus clear that as inclusions, even though they can be enriched in MREE, cpx can be excluded as the reason for the sinusoidal patterns.

A model perovskite cumulate Onuma REE diagram was constructed by adding experimental partition coefficients for the two phases in the approximate proportions of 15% CaPv (sample 2CST2 from Corgne and Wood, 2005) and 85% MgPv (2016a from Corgne et al. 2005) to resemble the Ca:Mg ratio of the observed garnets. This mixture yields Onuma REE diagram that strongly resembles that of the sinusoidal garnets. Shown in figure 11 are the observed Onuma diagrams for CaPv (11a) and MgPv (11b), whereas figure 11c shows a mixture of the two perovskite patterns (15% CaPv and 85% MgPv). Finally, figure 11d shows a sinusoidal garnet studied here (sample 039_6_141). The similarity between 11c and 11d is immediately apparent. As previously mentioned, sinusoidal garnets show a complete continuum between a normal garnet to one that is highly sinusoidal. This may reflect the progressive solubility of CaPv in garnet with decreasing depth (Wood, 2000). The presence of garnet and perovskite is not in violation of mantle mineralogy because it has been shown that there is a region in P-T space where both phases coexist (Gasparik and Hutchison, 2000; Wood, 2000). With increasing development of the sinusoidal segment, the limbs of the remaining Onuma diagram attributed to the Mg bearing phase (garnet or MgPv) become tighter, a characteristic of the distorted perovskite structure. Such a distorted perovskite structure is expected for the residual Mg orthorhombic (Pbmn) perovskite because it is here that the majority of the Al is presumed to reside (Wood, 2000). To give a garnet composition, 25% Al must be incorporated into the perovskite structure, where it is presumed to substitute for Si in the B-site of the perovskite structure. The substitution of Al^{3+} for Si^{4+} may, at least in part, be responsible for the high elastic moduli observed in the anomalously garnets REE patterns.

Notwithstanding the pleasing agreement between the modelled and observed patterns, we note that the slope in the Brice diagram for 11d (inset) is very high. Using the empirical cation-anion relationship of Hazen and Finger (1979), and the equations of Wood and Blundy (1997) to solve for temperature, the inferred P-T conditions at the time of crystallization are inadequate for a reasonable mantle adiabat (i.e. at 25 GPa, the fitted temperature is only 210°C). For comparison, fitting the data of Corgne and Wood (2005, sample 2CST2) revealed a precise match to their experimental conditions. However, an unusually high elastic modulus associated with phases under high pressure has been previously reported by van Westrenen (2007), who devised an alternative empirical quantification used to predict the elastic modulus of a mineral under these conditions. Although his empirical model does much better at predicting the P-T conditions at the time of formation (i.e. a fitted temperature of 500°C) it still falls short of giving what we consider to be accurate P-T conditions. Another reason for this discrepancy could be that due to the isochemical transformation of elements from two cumulate phases (CaPv and MgPv) into one lower P mineral (garnet), the resulting Brice diagram may reflect disequilibrium. In other words, envisaging a km-thick cumulate layer of perovskites that transforms to garnetite can only exchange with surrounding material, which is chemically identical and cannot therefore equilibrate.

An alternative explanation is that further mantle precursor phases, such as the tetragonal almandine pyrope phase (TAPP) and calcium alumino-silicate phase (CAS) were involved. This possibility cannot presently be assessed because of insufficient data regarding trace element distribution and details of crystallographic structure. Regardless, the need remains for a better quantification of elastic moduli at very high P.

5. Conclusions

The sinusoidal REE pattern associated with peridotitic garnet sampled by kimberlite cannot be reconciled by garnet crystallography and the CLSM. Garnets that display sinusoidal REE patterns may not necessarily have undergone metasomatic re-enrichment by fluids or melts in the mantle. When expressed as an Onuma diagram, many of these sinusoidal garnets display a sinus that is reminiscent of a phase other than garnet. Whereas a complex chain of events, invoking polybaric melting, followed by metasomatism to re-enrich the LREE and MREE and finally differential diffusion to lose the LREE selectively, is not impossible, we regard this currently preferred explanation as unlikely. Furthermore, it was found that HFSE systematics do not support metasomatism either.

One obvious alternative explanation - that the MREE enrichment is caused by undetected inclusions - was tested with an exhaustive investigation using a number of techniques. These experiments revealed sufficient evidence for the presence of inclusions in some of the garnets studied here but they were not present in all sinusoidal garnets and were present in garnets with a normal REE pattern. Together these data strongly indicate that the included phase(s) is not directly responsible for the sinusoidal REE pattern. We advance an alternative working hypotheses in which it is envisaged that these garnets originally precipitated in the lower part of the transition zone as perovskite cumulates from the magma ocean. In this region, two perovskites (CaPv + Mg Pv) or perovskite plus garnet are stable. Existing evidence suggests that these cumulates have REE characteristics similar to sinusoidal REE patterns, basically reflecting the superposition of two separate REE patterns from the bi-mineralic cumulate. In our model, the MREE apex

represents CaPv, while the HREE apex represents MgPv or garnet. According to recent high P experiments, such bi-mineralic assemblages can transform into single phase garnet upon decompression. Thus, subsequent exhumation of the cumulates upon entrainment of the transition zone into the upper mantle would result in the isochemical subsolidus regressive transformation to a daughter garnet phase. This garnet would then have simply inherited the REE distribution characteristics of the parent phase(s), namely two perovskites or perovskite plus garnet.

Notwithstanding the presently incompletely tested nature of the perovskite precursor hypothesis, it is hoped that the prospect of these garnets being samples from the magma ocean cumulates is sufficiently interesting to spark further investigations, including isotopic studies, into this possibility.

References

Bau M (1996) Controls on the fractionation of isovalent trace elements in magmatic and aqueous systems: Evidence from Y/Ho, Zr/Hf, and lanthanide tetrad effect. Contributions to Mineralogy and Petrology 123(3): 323-333 doi: 10.1007/s004100050159

Beattie P, Ford C, Russell D (1991) Partition coefficients for olivine-melt and orthopyroxene-melt systems. Contributions to Mineralogy and Petrology 109: 212–224

Blundy JD, and Wood B (1994) Prediction of crystal-melt partition coefficients from elastic moduli. Nature, pp 452-454

Blundy JD, Robinson JAC, Wood BJ (1998) Heavy REE are compatible in clinopyroxene on the spinel lherzolite solidus. Earth and Planetary Science Letters 160(3-4): 493-504

Brice JC (1975) Some thermodynamic aspects of growth of strained crystals. Journal of Crystal Growth 28(2): 249-253 doi: 10.1016/0022-0248(75)90241-9

Burgess SR, Harte B (2004) Tracing lithosphere evolution through the analysis of heterogeneous G9-G10 garnets in peridotite xenoliths, II: REE chemistry. Journal of Petrology 45(3): 609-634 doi: 10.1093/petrology/egg095

Corgne A, Liebske C, Wood BJ, Rubie DC, Frost DJ (2005) Silicate perovskite-melt partitioning of trace elements and geochemical signature of a deep perovskitic reservoir. Geochimica et Cosmochimica Acta 69(2): 485-496 doi: 10.1016/j. gca. 2004.06.041

Corgne A, Wood BJ (2004) Trace element partitioning between majoritic garnet and silicate melt at 25 GPa. Physics of the Earth and Planetary Interiors 143: 407-419 doi: 10.1016/j. pepi. 2003.08.012

Corgne A, Wood BJ (2005) Trace element partitioning and substitution mechanisms in calcium perovskites. Contributions to Mineralogy and Petrology 149(1): 85-97 doi: 10.1007/s00410-004-0638-3

Farquhar J, Wing BA, McKeegan KD, Harris JW, Cartigny P, Thiemens MH (2002) Mass-Independent Sulfur of Inclusions in Diamond and Sulfur Recycling on Early Earth. Science 298(5602): 2369-2372 doi: 10.1126/science. 1078617

Filiberto J, Jackson C, Le L, Treiman AH (2009) Partitioning of Ni between olivine and an iron-rich basalt: Experiments, partition models, and planetary implications American Mineralogist 94, 2-3,256-261

Gasparik T, Hutchison MT (2000) Experimental evidence for the origin of two kinds of inclusions in diamonds from the deep mantle. Earth and Planetary Science Letters 181(1-2): 103-114 doi: 10.1016/s0012-821x(00)00179-5

Greaux S, Nishiyama N, Kono Y, Gautron L, Ohfuji H, Kunimoto T, Menguy N, Irifune T (2011) Phase transformations of $Ca_3Al_2Si_3O_{12}$ grossular garnet to the depths of the Earth's mantle transition zone. Physics of the Earth and Planetary Interiors 185(3-4): 89-99 doi: 10.1016/j. pepi. 2011.02.001

Griffin WL, Shee SR, Ryan CG, Win TT, Wyatt BA (1999) Harzburgite to lherzolite and back again: metasomatic processes in ultramafic xenoliths from the Wesselton kimberlite, Kimberley, South Africa. Contributions to Mineralogy and Petrology 134(2-3): 232-250 doi: 10.1007/s004100050481

Hart, S. R. and Davis, K. E. (1978) Nickel partitioning between olivine and silicate melt. Earth and Planetary Science Letters, 40, 203–219

Harte B, Kirkley MB (1997) Partitioning of trace elements between clinopyroxene and garnet: Data from mantle eclogites. Chemical Geology 136(1-2): 1-24 doi: 10.1016/s0009-2541(96)00127-1

Hazen RM, Finger LW (1979) Bulk modulus-volume relationship for cation-anion polyhedra. Journal of Geophysical Research 84(NB12): 6723-6728 doi: 10.1029/JB084iB12p06723

Heinrich CA, Pettke T, Halter WE, Aigner-Torres M, Audetat A, Gunther D, Hattendorf B, Bleiner D, Guillong M, Horn I (2003) Quantitative multi-element analysis of minerals, fluid and melt inclusions by laser-ablation inductively-coupled-plasma mass-spectrometry. Geochimica et Cosmochimica Acta 67(18): 3473-3497 doi: 10.1016/s0016-7037(03)00084-x

Hellstrom J, Paton C, Woodhead J, Hergt J Iolite: software for spatially resolved LA-(quad and MC) ICPMS analysis. (2008) Mineralogical Association of Canada short course series 40: 343-348

Hoal KEO, Hoal BG, Erlank AJ, Shimizu N (1994) Metasomatism of the mantle lithosphere recorded by rare-earth elements in garnets. Earth and Planetary Science Letters 126(4): 303-313 doi: 10.1016/0012-821x(94)90114-7

Irifune T (1994) Absence of an aluminous phase in the upper part of the Earths lower mantle. Nature 370(6485): 131-133 doi: 10.1038/370131a0

Irifune T, Koizumi T, Ando JI (1996) An experimental study of the garnet-perovskite transformation in the system $MgSiO_3$-$Mg_3Al_2Si_3O_{12}$. Physics of the Earth and Planetary Interiors 96(2-3): 147-157 doi: 10.1016/0031-9201(96)03147-0

Ito E, Kubo A, Katsura T, Walter MJ (2004) Melting experiments of mantle materials under lower mantle conditions with implications for magma ocean differentiation. Physics of the Earth and Planetary Interiors 143: 397-406 doi: 10.1016/j. pepi. 2003.09.016

Kamber BS (2009) Geochemical fingerprinting: 40 years of analytical development and real world applications. Applied Geochemistry 24(6): 1074-1086 doi: 10.1016/j. apgeochem. 2009.02.012

Keller J, Zaitsev AN (2006) Calciocarbonatite dykes at Oldoinyo Lengai, Tanzania: The fate of natrocarbonatite. Canadian Mineralogist 44: 857-876

Kesson SE, Fitz Gerald JD, Shelley JM (1998) Mineralogy and dynamics of a pyrolite lower mantle. Nature 393(6682): 252-255 doi: 10.1038/30466

Latourrette T, Hervig RL, Holloway JR (1995) Trace-element partitioning between amphibole, phlogopite, and basanite melt. Earth and Planetary Science Letters 135(1-4): 13-30 doi: 10.1016/0012-821x(95)00146-4

Matsuzaki T, Shinoda K (2004) A method for digitizing the X-ray diraction pattern on X-ray film by Gandolfi camera. Journal of Geosciences 47: 1-8

Oguri K, Funamori N, Uchida T, Miyajima N, Yagi T, Fujino K (2000) Post-garnet transition in a natural pyrope: a multi-anvil study based on in situ X-ray diffraction and transmission electron microscopy. Physics of the Earth and Planetary Interiors 122(3-4): 175-186 doi: 10.1016/s0031-9201(00)00178-3

Oneill B, Jeanloz R (1990) Experimental petrology of the lower mantle - a natural peridotite taken to 54 gpa. Geophysical Research Letters 17(10): 1477-1480 doi: 10.1029/GL017i010p01477

Onuma N, Higuchi H, Wakita H, Nagasawa H (1968) Trace element partition between 2 pyroxenes and host lava. Earth and Planetary Science Letters 5(1): 47-51 doi: 10.1016/s0012-821x(68)80010-x

Petrus JA, Ross KC, McDonald AM (2011) DIIS: A cross-platform program for the reduction of X-ray diffraction data from a cylindrical area detector. Computers and Geosciences 1(1): 1 - 2

Petrus JA and Kamber BS (2012) VizualAge: a novel approach to LA-ICP-MS U-Pb geochronology data reduction. Geostandards and Geoanalytical Research, In press, doi: 10.1111/j. 1751-908X. 2012.00158. x

Quartieri S, Boscherini F, Chaboy J, Dalconi MC, Oberti R, Zanetti A (2002) Characterization of trace Nd and Ce site preference and coordination in natural melanites: a combined X-ray diffraction and high-energy XAFS study. Physics and Chemistry of Minerals 29(7): 495-502 doi: 10.1007/s00269-002-0251-9

Ringwood AE, Major A (1971) Synthesis of majorite and other high-pressure garnets and perovskites. Earth and Planetary Science Letters 12(4): 411-418 doi: 10.1016/0012-821x(71)90026-4

Ross KC, Kamber BS (2012) An empirical test of the crystal lattice strain model for rare-earth element partitioning into clinopyroxene. Chemical Geology (in press).

Schulze DJ (2003) A classification scheme for mantle-derived garnets in kimberlite: a tool for investigating the mantle and exploring for diamonds. Lithos 71(2-4): 195-213 doi: 10.1016/s0024-4937(03)00113-0

Shimizu N, Richardson SH (1987) Trace-element abundance patterns of garnet inclusions in peridotite-suite diamonds. Geochimica et Cosmochimica Acta 51(3): 755-758 doi: 10.1016/0016-7037(87)90085-8

Shimizu N, Sobolev NV (1995) Young peridotitic diamonds from the Mir kimberlite pipe. Nature 375(6530): 394-397 doi: 10.1038/375394a0

Sobolev NV, Lavrente'ev YuG, Pokhilenko NP, Usova LV (1973) Chrome-Rich Garnets from the Kimberlites of Yakutia and Their Parageneses. Contributions to Mineralogy and Petrology 40(1): 39-52 doi: 10.1007/bf00371762

Stachel T, Aulbach S, Brey GP, Harris JW, Leost I, Tappert R, Viljoen KS (2004) The trace element composition of silicate inclusions in diamonds: a review. Lithos 77(1-4): 1-19 doi: 10.1016/j. lithos. 2004.03.027

Stachel T, Viljoen KS, Brey G, Harris JW (1998) Metasomatic processes in lherzolitic and harzburgitic domains of diamondiferous lithospheric mantle: REE in garnets from xenoliths and inclusions in diamonds. Earth and Planetary Science Letters 159(1-2): 1-12 doi: 10.1016/s0012-821x(98)00064-8

Ulrich T, Kamber BS, Jugo PJ, Tinkham DK (2009) Imaging element-distribution patterns in minerals by laser ablation - inductively coupled plasma - mass spectrometry (LA-ICP-MS). Canadian Mineralogist 47(5): 1001-1012 doi: 10.3749/canmin. 47.5. 1001

Van Orman JA, Grove TL, Shimizu N, Layne GD (2002) Rare earth element diffusion in a natural pyrope single crystal at 2.8 GPa. Contributions to Mineralogy and Petrology 142(4): 416-424

van Westrenen W, Blundy J, Wood B (1999) Crystal-chemical controls on trace element partitioning between garnet and anhydrous silicate melt. American Mineralogist 84(5-6): 838-847

van Westrenen W, Blundy JD, Wood BJ (2000) Effect of Fe^{2+} on garnet-melt trace element partitioning: experiments in FCMAS and quantification of crystal-chemical controls in natural systems. Lithos 53(3-4): 189-201

van Westrenen W, Draper DS (2007) Quantifying garnet-melt trace element partitioning using lattice-strain theory: new crystal-chemical and thermodynamic constraints. Contributions to Mineralogy and Petrology 154(6): 717-730 doi: 10.1007/s00410-007-0222-8

van Westrenen W, Wood BJ, Blundy JD (2001) A predictive thermodynamic model of garnet-melt trace element partitioning. Contributions to Mineralogy and Petrology 142(2): 219-234

Veksler IV, Petibon C, Jenner GA, Dorfman AM, Dingwell DB (1998) Trace element partitioning in immiscible silicate-carbonate liquid systems: An initial experimental study using a centrifuge autoclave. Journal of Petrology 39 11-12: 2095-2104 doi: 10.1093/petrology/39.11.2095

Wang WY, Sueno S, Takahashi E, Yurimoto H, Gasparik T (2000) Enrichment processes at the base of the Archean lithospheric mantle: observations from trace element characteristics of pyropic garnet inclusions in diamonds. Contributions to Mineralogy and Petrology 139(6): 720-733 doi: 10.1007/s004100000163

Wood BJ (2000) Phase transformations and partitioning relations in peridotite under lower mantle conditions. Earth and Planetary Science Letters 174(3-4): 341-354 doi: 10.1016/s0012-821x(99)00273-3

Yusa H, Yagi T, Shimobayashi N (1995) A new unquenchable high-pressure polymorph of $Ca_3Al_2Si_3O_{12}$. Physics of the Earth and Planetary Interiors 92(1-2): 25-31 doi: 10.1016/0031-9201(95)03057-4

Zack T, Foley SF, Jenner GA (1997) A consistent partition coefficient set for clinopyroxene, amphibole and garnet from laser ablation microprobe analysis of garnet pyroxenites from Kakanui, New Zealand. Neues Jahrbuch Fur Mineralogie-Abhandlungen 172(1): 23-41

Figure captions

Figure 1: 1a shows a normal garnet REE pattern with a maximum Ln normalized concentration (NC) among the HREE and a smooth decline in with decreasing atomic number. 1b shows REE NC data for 1435_5_33 an intermediate garnet with incipient development of a sinusoidal segment giving rise to a clear peak between Nd and Gd followed by a trough around Tm - Yb. 1c shows a genuinely sinusoidal garnet (039_6_129) with a clear apex around Nd, a trough around Er and steeply enriched HREE. All data CI normalized (McDonough and Sun, 1995).

Figure 2: Scanning electron microscope (SEM) images of etched garnets. 2a: higher magnification image of garnet 1335_28_70 surface clearly showing cavities excavated by HF vapour with apparent etched grain cavities that vary from an orientation in the plane of the polished surface to cavities dipping deeply into the grain. 2b shows a lower magnification image of garnet 1435_5_33 after HF vapour etching.

Figure 3: Graphical representation of 255 individual EMP spot analyses across grain 1435_1_14. Elemental counting times were 20 s for Si, Al, Mg, Fe. 30 s for Cr and Ca, 40 s for Mn and 60 s for Na and Ti using a probe current of 20 nA with a spot size of 5 µm. Based on the size of the etch pits shown in figure 2, any compositional variation attributable to an included phase should have been detected.

Figure 4: XRD pattern acquired from garnet 039_6_129 where compositional data are given in table 1. The calculated garnet structure is shown in blue and the calculated background in green while observed data is shown in red. Peaks at d-spacing of 2.67 and 1.98 Å of 14 and 10% relative intensity respectively cannot be indexed on the cubic garnet unit cell.

Figure 5: Trace element map for Sm (red), Gd (peak height) and Sr (blue). Laser traverses were from obtained left to right with an 8 µm beam size at a rate of 2 µm/s. Image is approximately

250x250 µm. Areas appearing as lightly shaded represent localized Gd/Sm enrichment. Note that Sr rich areas are not coincident with MREE enriched areas.

Figure 6: 6a: TEM electron diffraction image of the garnet [111] zone axis. All diffraction spots are indexed on a garnet unit cell. 6b: cartoon of the garnet structure with the same orientation as in 6a.

Figure 7: Diagrams illustrating the effect of equilibration with melts differing in composition. Shown are three garnet REE patterns including a normal garnet, a normal garnet equilibrated with a highly fractionated carbonatite melt (Keller and Zaitsev, 2006. Sample O. L. 327 dyke II) and a garnet with sinusoidal REE. Although there is appreciable deflection from a normal garnet pattern in the carbonate normalized garnet in the region of Gd and Tb, the carbonate normalized pattern does not resemble the garnet with sinusoidal REE, which is shown for comparison. These values were derived by multiplying the experimental D's from Zack et al. by the REE concentrations of Klaudius and Keller (2006) then normalized by CI (McDonough and Sun, 1995).

Figure 8: Zr/Hf vs. Y/Ho for the garnets analyzed here after Bau (1996). Field **a** represents the area typically occupied by elements that conform to charge and radius controlled (CHARAC) behaviour. Solid black circle shows chondritic ratios. Field **b** shows the region of Zr/Hf – Y/Ho space typically occupied by hydrogenous Fe-Mn crusts. It is important to note the data represented by the megacryst ellipse, which have undergone no metasomatic enrichment, occupy a similar space to the majority of the lherzolite and harzburgite grains. Evidence presented by Bau (1996) shows that modification of the Y/Ho – Zr/Hf signature by felsic melts (regardless of an aqueous component) will cause observed ratios to migrate in a trend parallel to that shown for the hydrothermal vein signature.

Figure 9: 9a: Plot of measured apparent D vs. atomic number for garnet and cpx from this study normalized to CI chondrite (McDonough and Sun, 1996). 9b: Onuma diagram of garnet and cpx from 9a showing the smooth parabolic decrease in D with increasing difference in radii from Ro, given by the apex of the Onuma diagram. Since the site on which trace elements substitute in garnet is as small as or smaller than the smallest REE (Lu, 0.977 Å, Shannon, 1976), only the left limb of the Onuma diagram is apparent. Apices of the Onuma diagrams are indicated by shaded vertical rectangle. 9c: Parameterized fit to the Onuma diagram formalized by Brice (1975) given

as equation 1. Informally referred to here as a Brice diagram, the intercept represents the Ln of the maximum D (Do) while the slope is proportional to the elasticity of the polyhedra. Notice that the slope in 9c corresponding to cpx is greater than that for garnet, indicating that the garnet X-site has limbs in the Onuma diagram that slope more gently showing greater elasticity than the cpx M2-site.

Figure 10: 10a: M2-cpx (open squares) and X-site garnet (solid circles) Onuma diagrams showing the distribution coefficients characteristic for the REE in these two minerals. 10b: Brice diagrams for garnet (solid circles) and cpx (open squares), garnet and cpx are of peridotitic paragenesis and are therefore considered directly comparable in absolute trace element concentration. 10c: A pattern representing a mixture of 10% cpx in garnet shows the development of an apex around Sm. 10d: Similar to 10c, but representing 20% cpx in garnet. Lines are as in 10c and show the development of a weak trough around Eu.

Figure 11: 11a: Onuma diagram for Ca silicate perovskite (CaPv) showing Ro (vertical grey rectangle) of 1.116 Å after Corgne et al., (2005). 11a inset shows a Brice diagram for CaPv. 11b: Onuma diagram for Mg silicate perovskite (MgPv, Corgne et al., 2005). 11b inset shows a Brice diagram for MgPv. Note: Owing to their exceedingly low concentration, La, Ce and Pr were not used in the fitting of the Brice diagram. 11c: additive Onuma diagram of 15% CaPv in MgPv. The combined pattern (red crosses) shows a sinus located approximately over Pr with a positive slope among Sm, Eu, Gd and Tb followed by very steep negative HREE. 11d: A typical sinusoidal garnet modelled by the crystal lattice strain model (CLSM) as two Onuma diagrams with the apices of the large site (LS) and small site (SS) around Nd and between Sc and Lu, (but closer to Sc) respectively.

Figure 1

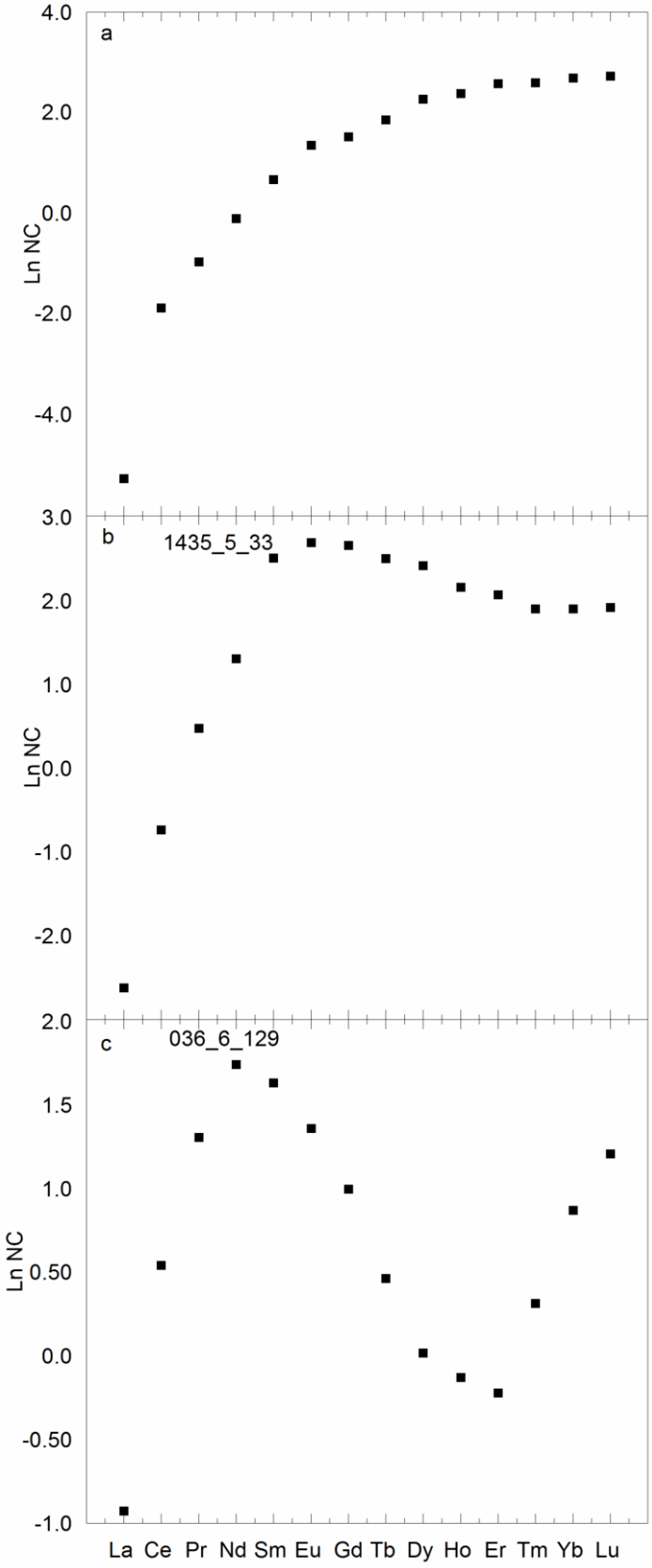
a
b
1435_5_33
c
036_6_129
Ln NC
Ln NC
Ln NC
4.0
2.0
0.0
-2.0
-4.0
3.0
2.0
1.0
0.0
-1.0
-2.0
2.0
1.5
1.0
0.50
0.0
-0.50
-1.0
La Ce Pr Nd Sm Eu Gd Tb Dy Ho Er Tm Yb Lu

Figure 2

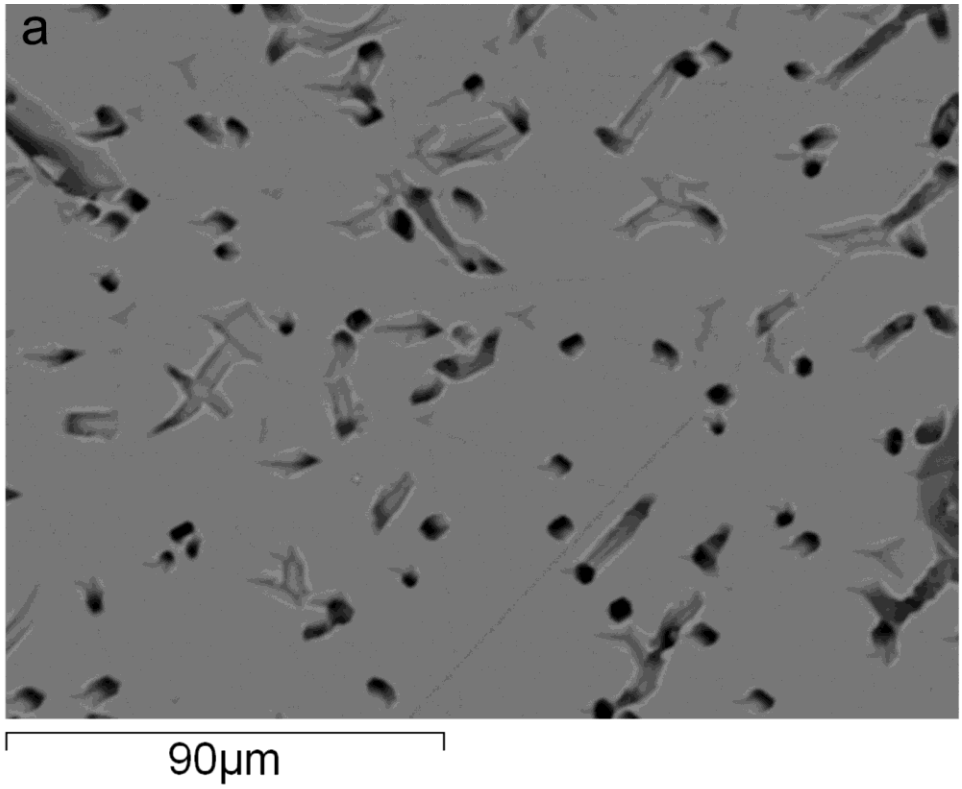

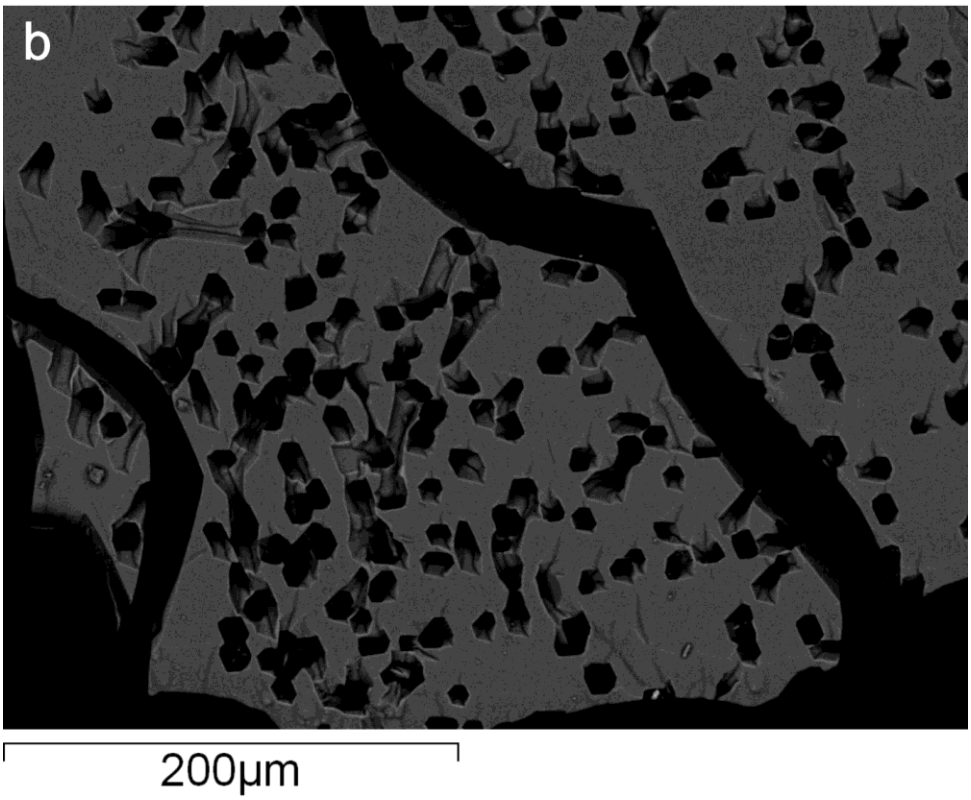

Figure 3

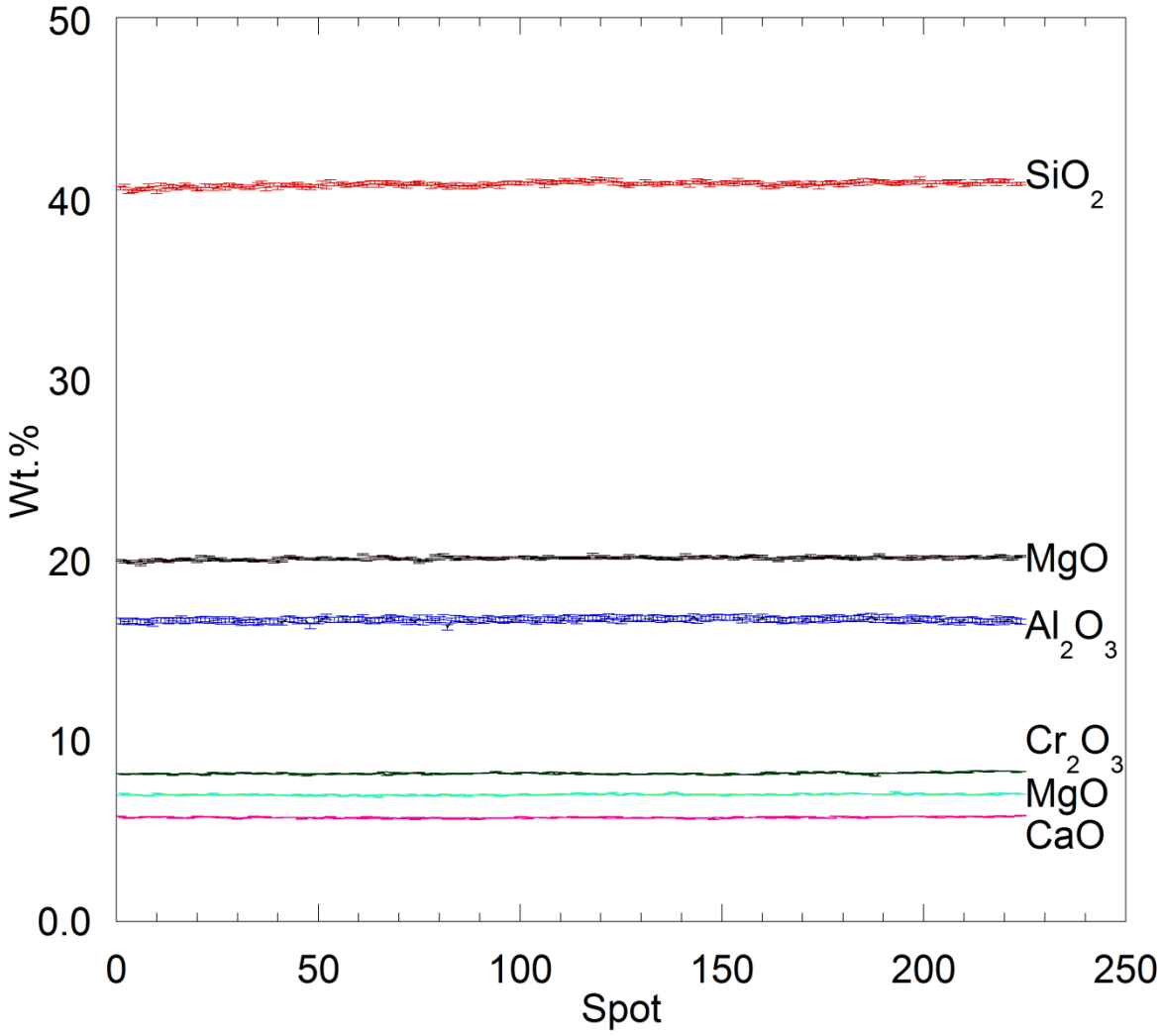
50
40
30
20
10
0.0
Wt.%
0
50
100
150
200
250
Spot
SiO2
MgO
Al2O3
Cr2O3
MgO
CaO

Figure 4

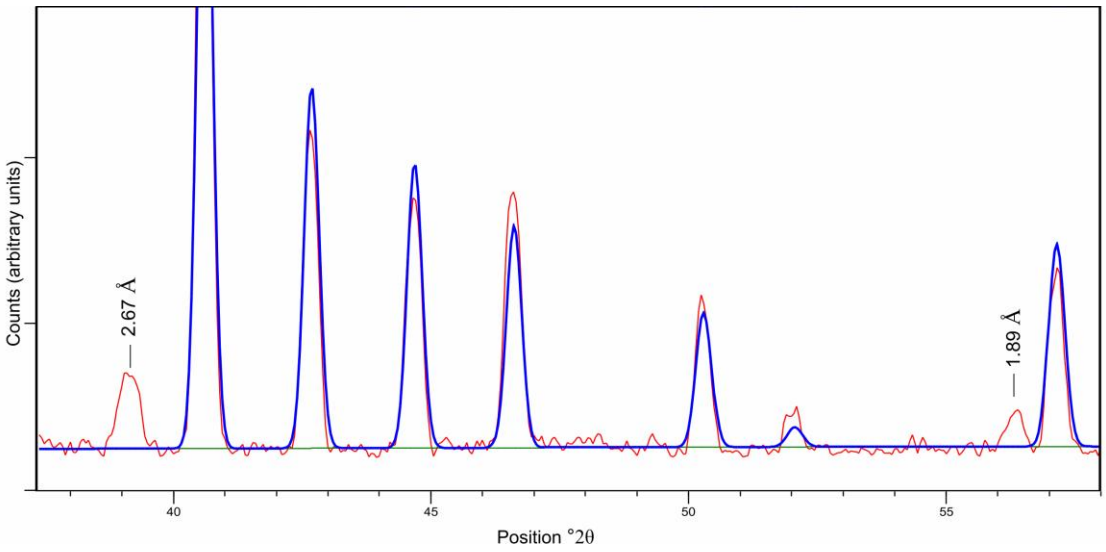

Figure 5

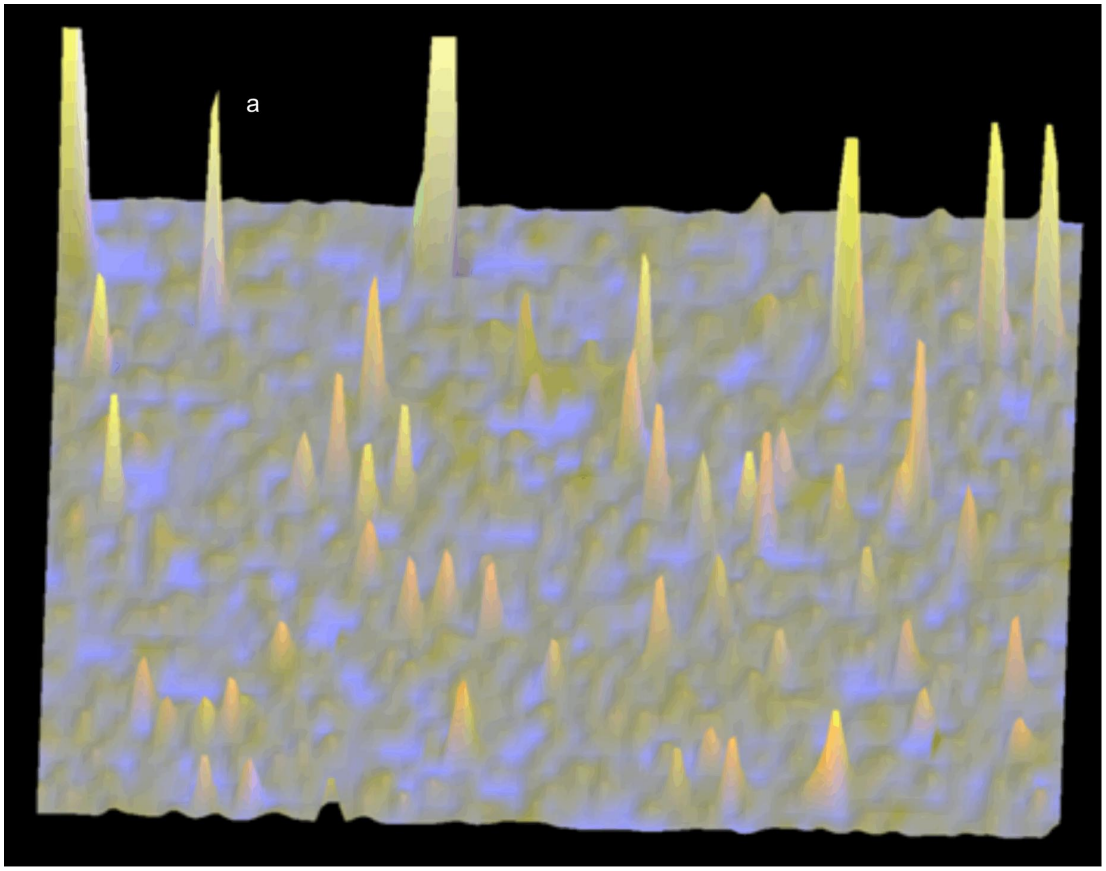

Figure 6

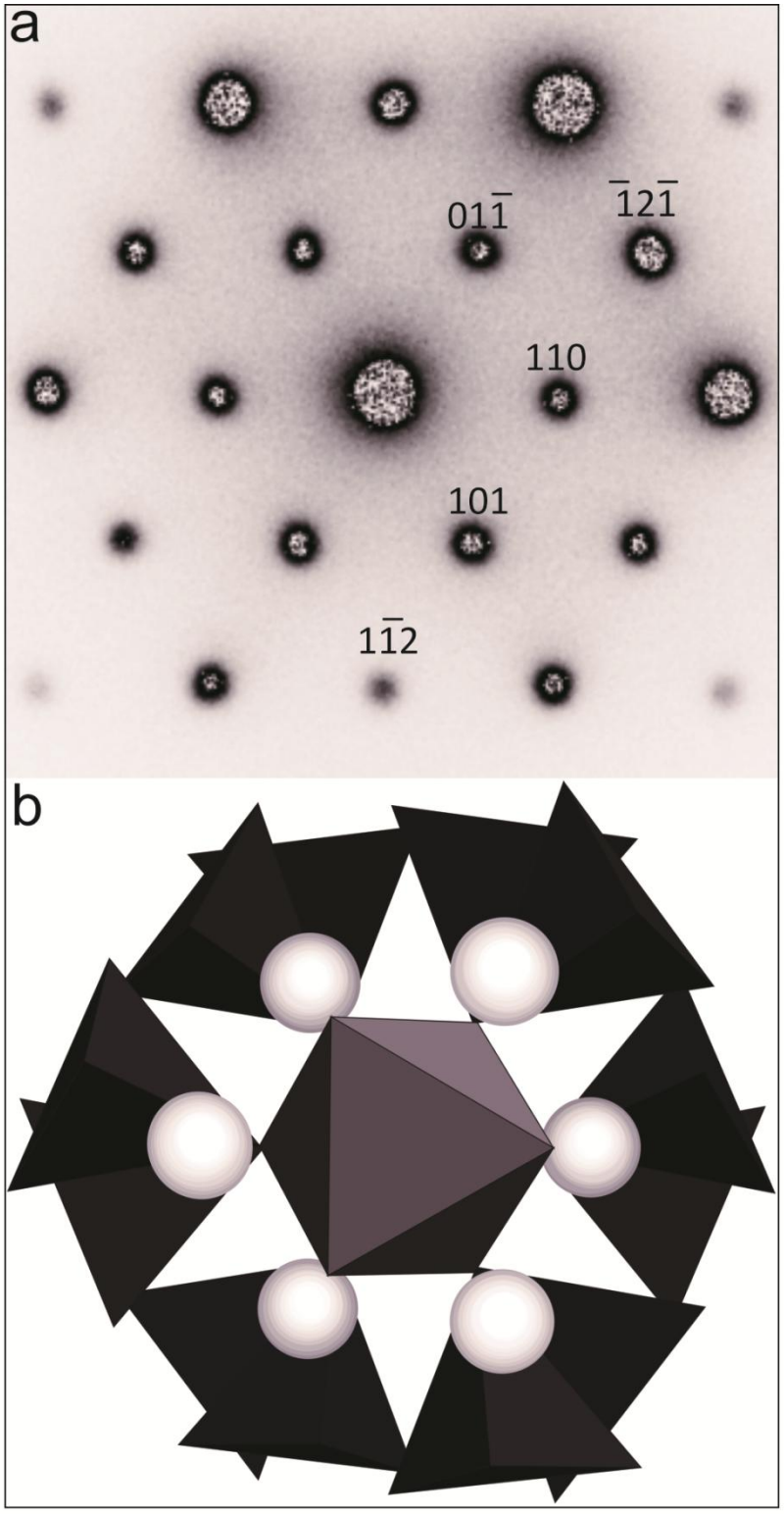

Figure 7

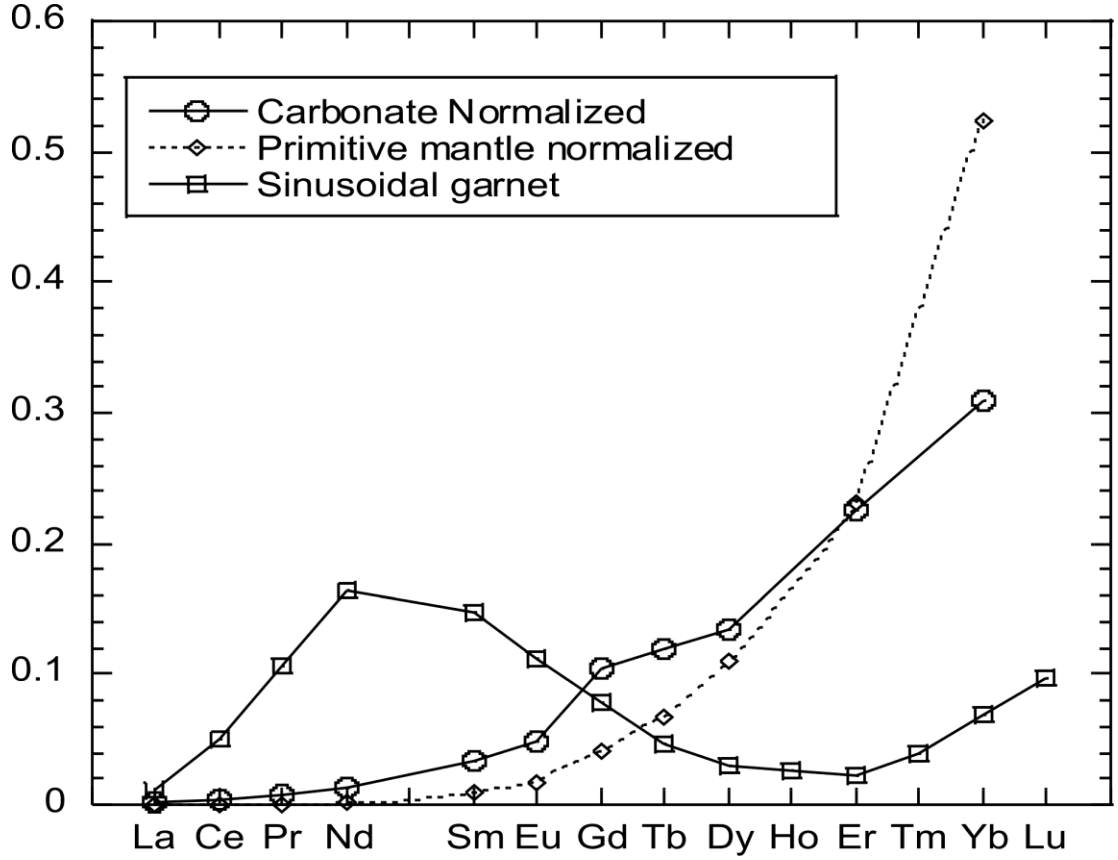
0.6
0.5
0.4
0.3
0.2
0.1
0
Carbonate Normalized
Primitive mantle normalized
Sinusoidal garnet
La Ce Pr Nd Sm Eu Gd Tb Dy Ho Er Tm Yb Lu

Figure 8

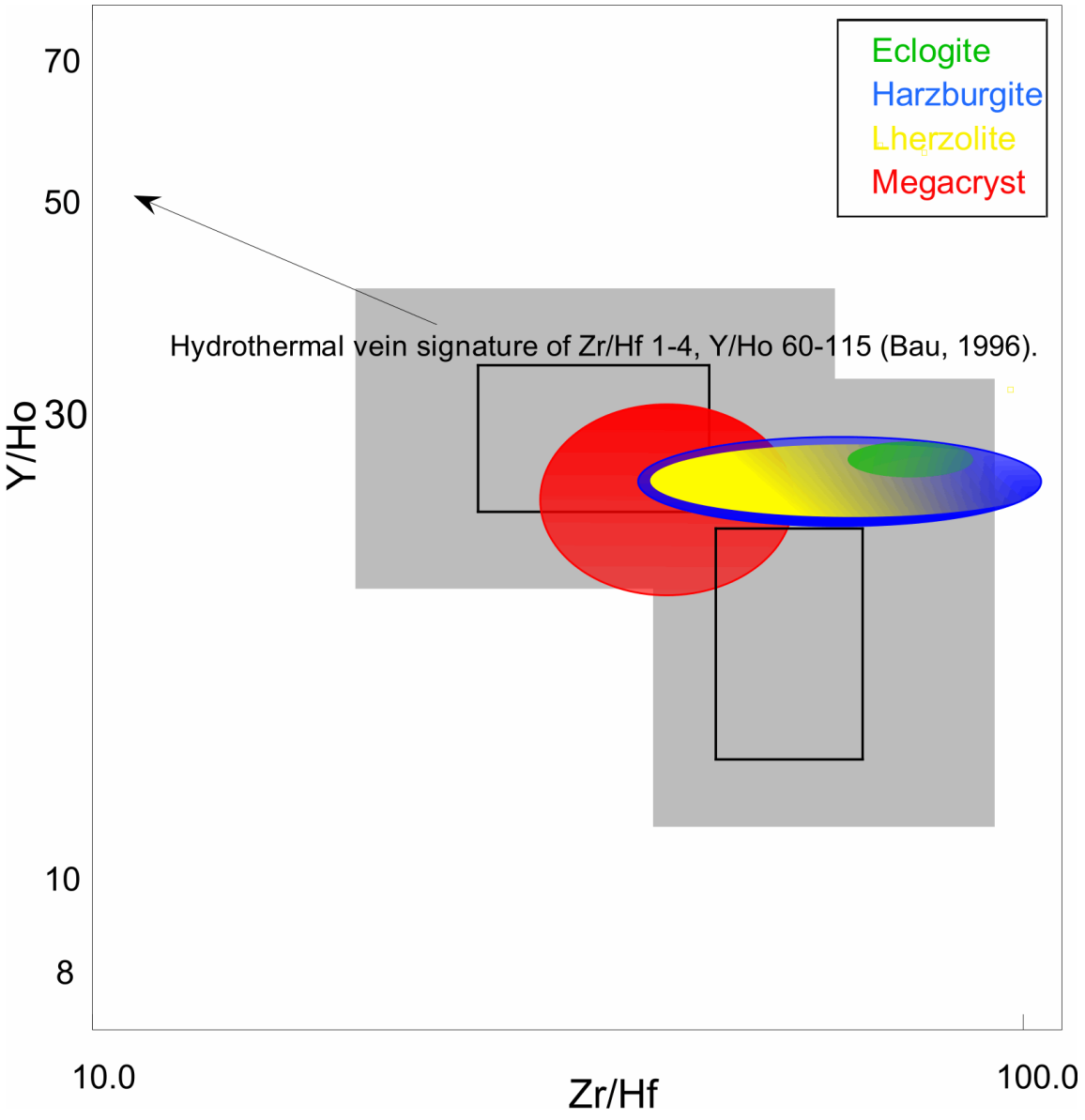
Eclogite
Harzburgite
Lherzolite
Megacryst
Hydrothermal vein signature of Zr/Hf 1-4, Y/Ho 60-115 (Bau, 1996).
70
50
30
10
8
Y/Ho
10.0
100.0
Zr/Hf

Figure 9

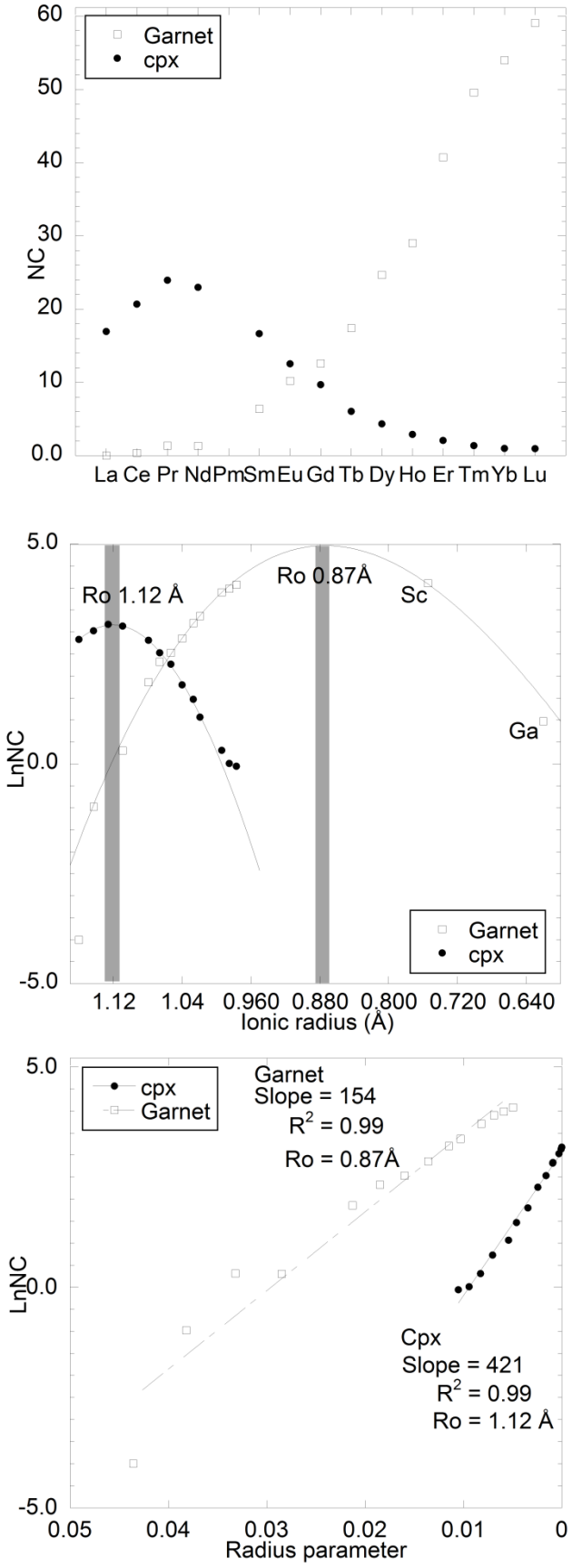
Garnet
cpx
NC
60
50
40
30
20
10
0.0
La Ce Pr Nd Pm Sm Eu Gd Tb Dy Ho Er Tm Yb Lu
Ro 1.12 Å
Ro 0.87Å
Sc
Ga
LnNC
5.0
0.0
-5.0
1.12 1.04 0.960 0.880 0.800 0.720 0.640
Ionic radius (Å)
cpx
Garnet
Garnet
Slope = 154
R2 = 0.99
Ro = 0.87Å
Cpx
Slope = 421
R2 = 0.99
Ro = 1.12 Å
0.05 0.04 0.03 0.02 0.01 0
Radius parameter

Figure 10

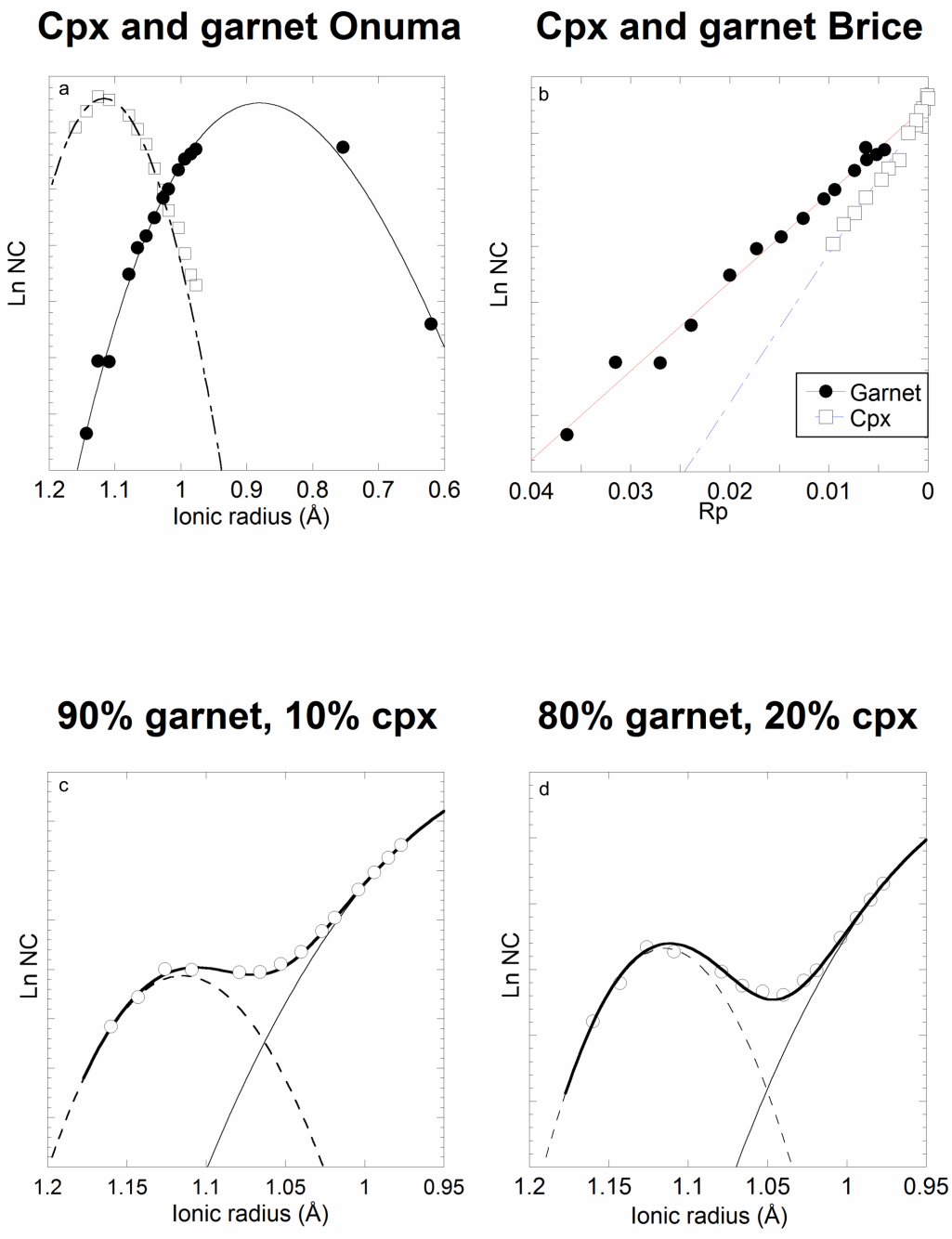
Cpx and garnet Onuma
a
Ln NC
1.2 1.1 1 0.9 0.8 0.7 0.6
Ionic radius (Å)
Cpx and garnet Brice
b
Ln NC
0.04 0.03 0.02 0.01 0
Rp
Garnet
Cpx
90% garnet, 10% cpx
c
Ln NC
1.2 1.15 1.1 1.05 1 0.95
Ionic radius (Å)
80% garnet, 20% cpx
d
Ln NC
1.2 1.15 1.1 1.05 1 0.95
Ionic radius (Å)

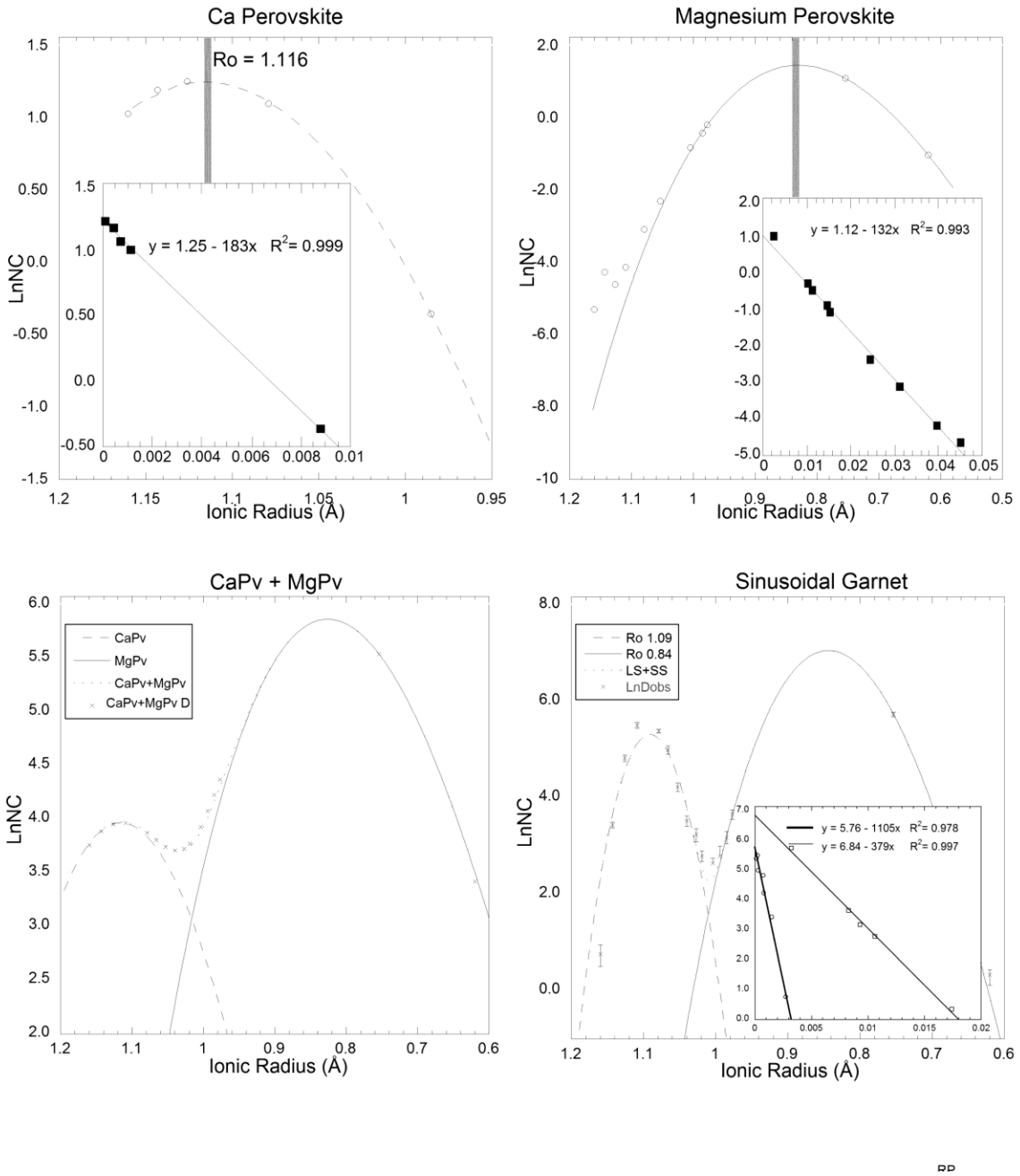
Ca Perovskite
Ro = 1.116
y = 1.25 - 183x R²= 0.999
LnNC
Ionic Radius (Å)
Magnesium Perovskite
y = 1.12 - 132x R²= 0.993
LnNC
Ionic Radius (Å)
CaPv + MgPv
CaPv
MgPv
CaPv+MgPv
CaPv+MgPv D
LnNC
Ionic Radius (Å)
Sinusoidal Garnet
Ro 1.09
Ro 0.84
LS+SS
LnDobs
y = 5.76 - 1105x R²= 0.978
y = 6.84 - 379x R²= 0.997
LnNC
Ionic Radius (Å)

Figure 11

Table 1

Major and trace element composition of garnets with sinusoidal REE patterns

wt%	1335_28_70		1435_1_14		1435_5_ 33		039 _6 _129		039_ 6 _141		039_ 6 _152	
SiO_2	42.21		41.36		41.19		40.76		41.76		41.56	
TiO_2	0.49		b.d.		0.21		0.07		b.d.		b.d.	
Al_2O_3	16.83		20.58		17.7		17.08		21.19		21.15	
Cr_2O_3	8.32		3.57		7.94		8.71		3.87		3.46	
FeO	7.65		7.88		7.46		7.36		8.12		7.95	
MnO	0.16		0.37		0.36		0.32		0.51		0.52	
MgO	19.41		20.57		20.25		18.49		20.72		20.15	
CaO	**5.72**		4.54		5.95		7.28		4.29		5.36	
Na_2O	0.09		0.02		0.04		0.02		0.01		b.d.	
ppm												
Sc	124	(6)	164	(12)	163	(5)	180	(6)	199	(6)	226	(7)
Ga	n.a.		n.a.		n.a.	(0.38)	5.81	(0.35)	1.38	(0.15)	1.39	(0.17)
Sr	4.78	(0.04)	0.68	(0.05)	0.40	(0.04)	0.39	(0.08)	0.54	(0.04)	0.50	(0.04)
Y	6.32	(0.20)	1.95	(0.31)	11.63	(0.11)	1.10	(0.45)	2.63	(0.17)	2.79	(0.21)
Zr	19.00	(1.47)	26.9	(2.4)	79.14	(0.60)	9.48	(0.80)	16.13	(0.83)	7.95	(0.34)
Nb	0.09	(0.05)	0.17	(0.03)	0.38	(0.06)	0.41	(0.05)	0.15	(0.04)	0.28	(0.05)
La	0.04	(0.01)	0.05	(0.02)	0.02	(0.02)	0.09	(0.01)	0.05	(0.01)	0.04	(0.01)
Ce	0.20	(0.05)	0.70	(0.11)	0.29	(0.05)	1.04	(0.03)	2.02	(0.12)	0.84	(0.05)
Pr	0.08	(0.03)	0.36	(0.06)	0.14	(0.03)	0.33	(0.01)	1.19	(0.08)	0.32	(0.03)
Nd	0.71	(0.29)	5.22	(0.70)	1.68	(0.22)	2.58	(0.06)	12.01	(0.74)	2.63	(0.13)
Sm	0.54	(0.10)	4.60	(0.60)	1.82	(0.07)	0.75	(0.03)	3.45	(0.12)	1.54	(0.09)
Eu	0.30	(0.11)	1.11	(0.18)	0.83	(0.03)	0.22	(0.03)	0.89	(0.08)	0.63	(0.06)
Gd	0.97	(0.15)	1.99	(0.33)	2.84	(0.08)	0.53	(0.09)	1.45	(0.13)	1.59	(0.15)
Tb	0.20	(0.02)	0.18	(0.03)	0.45	(0.01)	0.06	(0.02)	0.13	(0.01)	0.20	(0.02)
Dy	1.23	(0.06)	0.67	(0.16)	2.75	(0.03)	0.25	(0.13)	0.66	(0.09)	0.92	(0.08)
Ho	0.25	(0.01)	0.08	(0.02)	0.48	(0.01)	0.05	(0.02)	0.10	(0.01)	0.11	(0.01)
Er	0.71	(0.03)	0.21	(0.09)	1.27	(0.03)	0.13	(0.07)	0.24	(0.03)	0.20	(0.03)
Tm	0.11	(0.01)	0.04	(0.01)	0.16	(0.01)	0.03	(0.01)	0.04	(0.01)	0.02	(0.01)
Yb	0.68	(0.07)	0.34	(0.10)	1.10	(0.05)	0.39	(0.10)	0.42	(0.05)	0.24	(0.04)
Lu	0.11	(0.01)	0.09	(0.05)	0.17	(0.01)	0.08	(0.02)	0.10	(0.01)	0.07	(0.01)
Hf	0.42	(0.05)	0.29	(0.15)	1.49	(0.07)	0.25	(0.05)	0.22	(0.06)	b.d.	

Major elements in wt.%. Trace elements in ppm. Superscript on trace elements denotes mass measured. b. d. is below detection, n.a. is not analysed. Values in parenthesis are 2σ on concentration measurements.

Chapter 4 appendix

Trace element maps

Selected garnets exhibiting sinusoidal REE patterns were later revisited with a high efficiency Resonetics M-50 Excimer LA system. Traverses of 2 cm length using a 10 µm spot size and a speed of 2µm/s were carried out. The repetition rate was 5 Hz, meaning that each region along the traverse was sampled by 12-13 laser pulses. The analytes were restricted to key masses, namely Ce, Sm, Gd, Dy, Er, and Yb to define the REE pattern with the least number of those analytes with best counting statistics. The very small spot size of the laser beam coupled with the sub-ppm detection limits of the system revealed that MREE are not homogenous across a grain but that <10 µm areas are encountered with significant relative MREE enrichment. This observation suggests either heterogeneity in REE chemistry in otherwise chemically homogenous garnet or the current- or past-presence of MREE-enriched inclusions. Etching experiments revealed the presence of <5 µm inclusions that more readily dissolve in HF vapour than the host garnet (chapter 4, §3.3), favouring the second hypothesis. However, spatial correlation between the etch pits and MREE enrichment was not established.

Figure 4A1

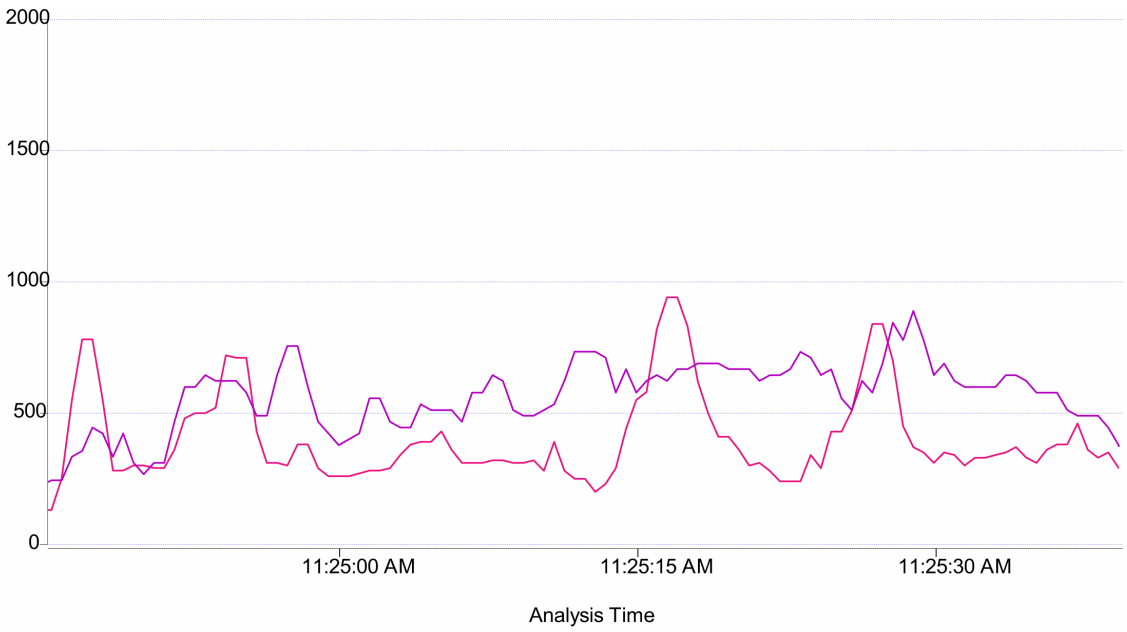

Figure 4A1, Chart of analysis time vs. raw signal intensity (counts per second) for Sr (pink) and Sm (purple).

Figure 4A2

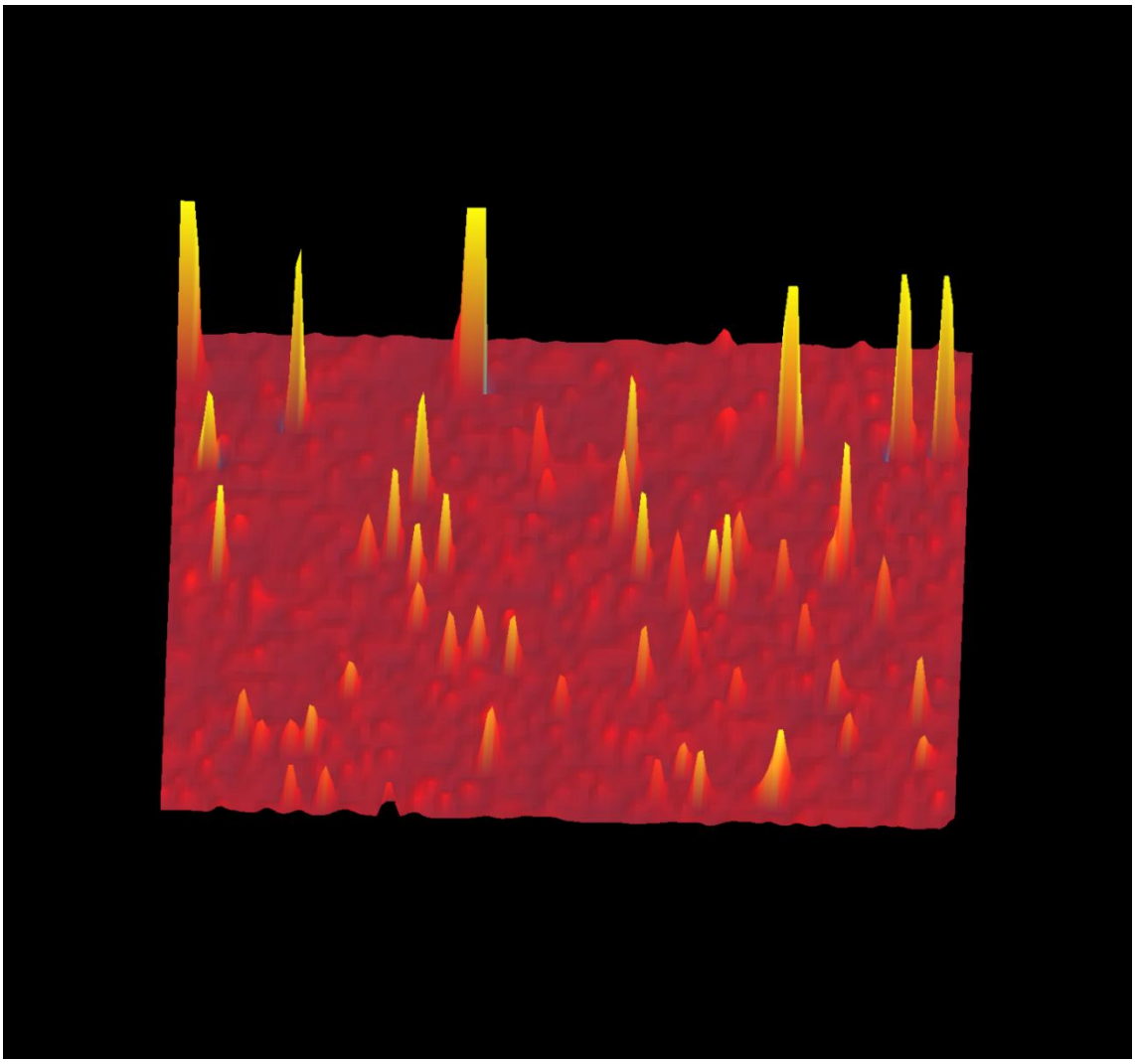

Figure 4A2 is a 3-dimensional map of relative signal intensities showing the correlation between Gd (yellow) and Sm (peak-height) for garnet 1435_5_33. Note that not all Gd highs (yellow and orange colors) correspond to Sm highs (peak-height) whereas all Sm highs seem to also correspond to Gd highs. Laser traverses were from left to right with an 8 µm beam size at a rate of 2 µm/s. Image is approximately 250 x 250 µm.

Table 4A1, Laser map detection limits

Element	Mass	Background cps	ppm	3 RSD background CPS	ppm LOD
Sr	88	107	2.3	13.74	0.292
Y	89	19.75	1	12.24	0.618
Sm	147	1.14	0	1.43	0.01
Dy	163	0	0	1.5	0
Gd	157	0.55	0	0.65	0
Er	166	0	0	1.5	0.13
Yb	172	0	0	1.5	0.17

Sensitivity	average CPS	PPM in 612	CPS/ppm	
Sr	26786	78	342	Map
Y	12555	38	330	Map
Sm	15812	38	415	Line
Dy	14934	36	415	Line
Gd	16656	37	454	Map
Er	16055	38	422	Line
Yb	16126	39	411	Line

Leach experiments

Two experiments were designed. First, ca. 100 µg grains of sinusoidal garnet fragments (sample 152) were ground in agate and the resulting powder was subjected to a 2 hour leach in cold 50% HF. The acid was transferred to a separate vessel and the remaining garnet digested at high P and T with full strength HF and HNO_3. Both fractions were analyzed separately by solution ICP-MS according to the procedure detailed in Ross and Kamber (2012, Chapter 3). Second, a polished garnet (sample 76) was placed face down in 50% warm HF for 20 minutes and the resulting acid was then dried down, converted and analyzed. A separate aliquot of the garnet was powdered and digested.

Neither of the leachates yielded absolute concentrations because the mass of leached material could not be determined therefore no dilution factor could be calculated. Instead, the dilution factors were guessed such that the MREE and HREE contents of the leachate and the residue (sample 152) and whole garnet (sample 76) had the same concentrations (listed in Table 4A2). This was done to aid the comparison of the shape of the normalized REE patterns. In both cases, the REE pattern for MREE and HREE of the leachate was exactly identical to those obtained by LA-ICP-MS and from the residue and bulk garnet, respectively. There are two important observations. First, the patterns of the leachate also have the very strong HREE enrichment of the bulk garnet. Second, they have exactly identical sinusoidal MREE enrichment. These data strongly indicate the MREE enrichment is not stronger in the leachate than in the bulk garnet. Consequently, it is very likely that the HF leached REE from the garnet itself and that no significant REE concentrations were released from the material less resistant to HF than garnet. The only difference is that the LREE appear slightly enriched in the leachates. This is very likely

the result of insufficient blank correction. It was not possible to conceive an appropriate blank experiment and therefore, a pure digestion blank was used for correction. However, the leaching experiments required a fair bit of manual handling, which may have introduced additional blank. Furthermore, because the dilution factor was unknown it was not possible to assign a proper dilution factor to the digestion blank either. Finally, the total signal intensities for the LREE were close to the detection limits, introducing further uncertainty. For these collective reasons, no significance should be attributed to the small upswings in LREE in the leachates.

Table 4A2 Leach experiments

Concentration in ppb

	Garnet 152	Leachate from garnet 152	Garnet 76	Leachate from garnet 76
La	75.58	621.41	29.62	324.34
Ce	314.73	1178.36	156.71	497.69
Pr	103.46	160.64	90.90	133.75
Nd	1090.98	1140.25	1556.90	1666.70
Sm	960.39	874.26	2146.50	2185.02
Eu	449.72	421.15	1156.00	1169.83
Gd	340.49	312.89	557.24	558.31
Tb	1577.28	1439.38	4330.49	4314.61
Dy	2128.47	1977.80	1152.35	1160.87
Ho	419.02	385.02	116.92	126.58
Er	1044.75	961.03	324.65	323.72
Tm	148.15	139.68	63.48	67.48
Yb	936.39	858.13	559.87	617.64
Lu	150.61	142.62	120.88	124.28

D values (CI normalized)

	Garnet 152	Leachate from garnet 152	Garnet 76	Leachate from garnet 76
La	0.32	2.62	0.12	1.37
Ce	0.51	1.93	0.26	0.81
Pr	1.09	1.69	0.96	1.41
Nd	2.34	2.44	3.33	3.57
Sm	6.28	5.71	14.03	14.28
Eu	7.75	7.26	19.93	20.17
Gd	7.68	7.00	21.07	21.00
Tb	9.10	8.37	14.90	14.93
Dy	8.38	7.79	4.54	4.57
Ho	7.40	6.80	2.07	2.24
Er	6.31	5.81	1.96	1.96
Tm	5.81	5.48	2.49	2.65
Yb	5.51	5.05	3.29	3.63
Lu	5.93	5.62	4.76	4.89

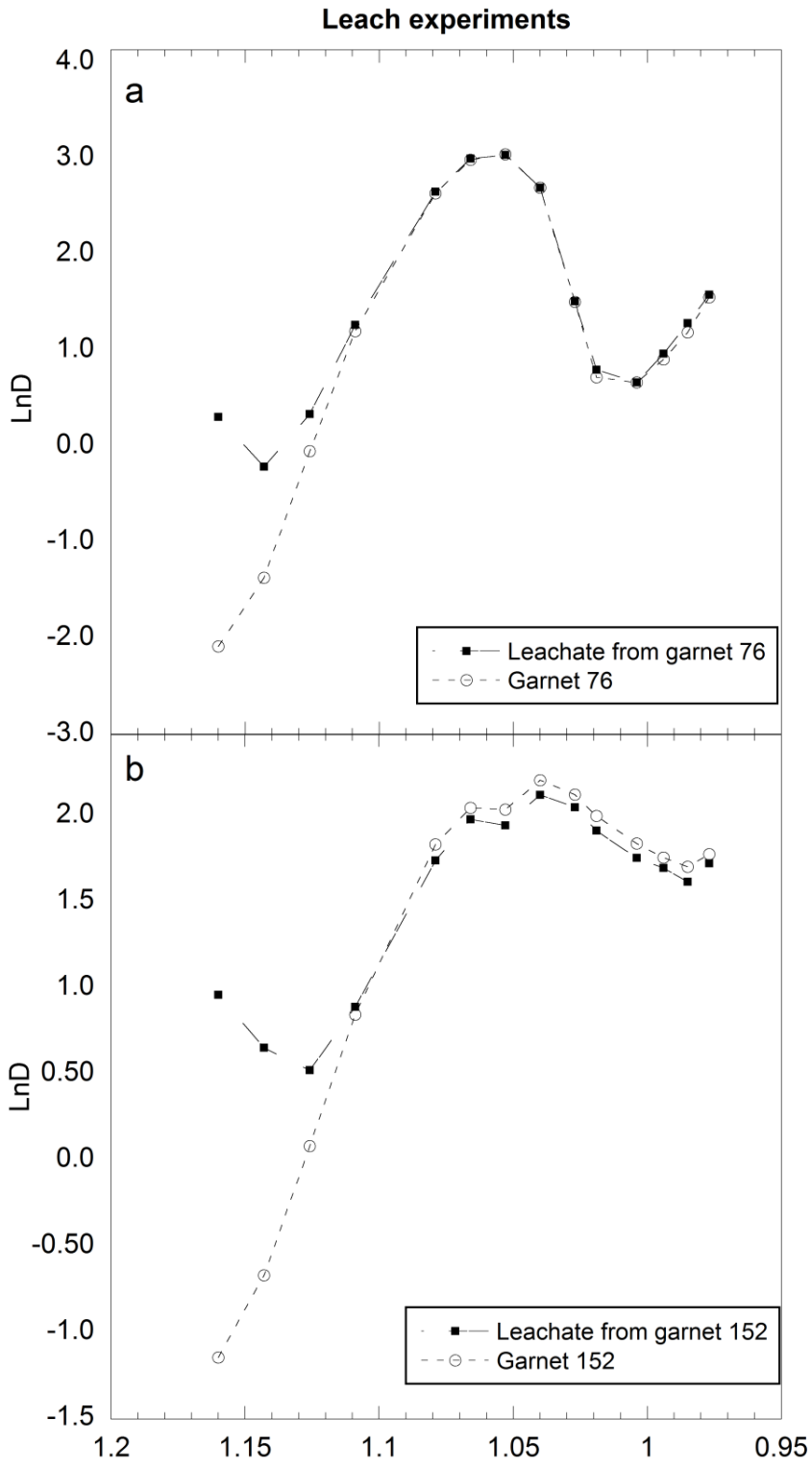

Figure 4A3 shows leach and residual analyses for sinusoidal garnet grains 76 and 152. Pre- and post-leach analyses are nearly identical with exception of the LREE.

Chapter 5

1. Summary and conclusions

This thesis contains data that are relevant for the explanation of sinusoidal garnet REE patterns observed in peridotitic garnets associated with kimberlite deposits. First, structural characterization was conducted on a 114.6 mm Gandolfi camera. It has been shown that the Gandolfi technique used here is capable of providing a full profile digital diffractogram amenable to Rietveld structural refinement (chapter 2). This method permits the detection of a simulated powder diffractogram from a monocrystalline grain fragment enabling the measurement of XRD data and trace elements of the very same mineral fragments. Using this XRD technique, it was shown in chapter 3 that there is a strong correlation between the crystallographic parameters given from the XRD data and those determined from the trace element distribution as determined using the Brice formalization and the CLSM. Focused on cpx, the study presented in chapter 3 substantiates the CLSM by not only showing a strong correlation among crystallographic parameters for the M2 site, but also the M1. Interestingly, the data presented in chapter 3 also suggest that given the known structure of a mineral and measured trace element distribution, an equilibration melt composition can be calculated based on the known shape of the Onuma diagram.

Finally, the technique developed in chapter 2 combined with implications derived from chapter 3 enabled in-depth re-investigation of kimberlite –derived peridotitic garnets that exhibit a sinusoidal REE pattern. It was shown in chapter 4 that mantle metasomatism re-enrichment, the widely accepted theory for sinusoidal garnets, is not likely the cause of the sinuous REE patterns. Additionally, the XRD technique outlined in chapter 2 enabled

investigation into the presence of an included phase as the source of the anomalous REE pattern. No included phase was detected in significant quantities to give such a REE pattern. Since neither of these possibilities adequately explains the sinusoidal REE patterns, we concluded that the sinuous REE pattern reflects the unique parageneses of these garnets.

Questions that were not addressed by the present contribution include: what was the cause of the etch pits? Why were zones of MREE- and Sr-enrichment not correlated? Can positive proof be provided for the presence of a perovskitic phase in these peridotitic-garnets?

The surface of a polished puck containing sinusoidal garnets was exposed to boiling 50% HF vapour. This left many small (2-20 μm) euhedral cavities with low apparent symmetry randomly dispersed on the grain surface (chapter 4, figure 4). Consideration of causes for such pits are discussed in chapter 4, section 3.3, where it was shown that such pits are likely the result of an included silicate phase preferentially dissolved by the HF vapour. Observation of the etch pits initiated a compositional investigation the nature of which has never before been reported for sinusoidal garnets. Outlined in the chapter 4 appendix are the details and results of the mapping experiment. Figure 5.1 is a compositional map showing the concentration (ppm) of Gd in yellow and Sm as height. Good correlation is indicated by peak height with increasing yellow component indicating that MREE enrichment occurs in localized areas rather than homogenous distribution within the garnet. It is somewhat surprising that simultaneous measurement of Sr also showed localized enrichment, but the Sr did not correlate to the areas of MREE

enrichment. Thus, correlation between the material excavated and REE enrichment has not been established.

In addition to the anomalous localized spatial trace element distribution, positive identification must be made of phases included within the garnet grain. Although the peaks observed correspond to the characteristic peaks of an orthorhombic perovskite, subsequent analysis must be performed to conclusively show the precise nature of this material. Such investigations were attempted with a HORIBA micro-raman apparatus with manual stage control. In light of the manual nature of the stage movement combined with the micron-scale nature of the observed inclusions, no shift was observed associated with any phase other than garnet. With the addition of automated stage control combined with mapping software, valuable data can be obtained as to the chemistry and bonding nature of material exposed at or near the grain surface. Although difficult with regards to sample preparation, electron back scatter diffraction (EBSD) shows great promise mapping *in-situ* diffraction data from the surface of a polished grain mount.

The objective of this thesis was to explain the relative MREE enrichment observed in peridotitic garnets associated with kimberlite deposits. Initially, we were working under the premise that these unusual REE patterns were the direct result of crystalline material included in the host garnet. After extensive investigations using LA-ICPMS, EMP, SEM-EDS, XRD and HF etching experiments, it became clear these unusual REE patterns were not the result of any easily detectible included material that shows unique major-element composition or crystallography. Upon deep consideration of the exact shape of the sinuous garnet patterns, combined with a new appreciation of the exact relationship between crystallography and REE distribution in a mineral, it became clear that such

patterns were representative of the REE distribution characteristics of a phase other than garnet. Considering the extensive investigations for the presence of inclusions revealed no other phase for the majority of the grains studied, I posit that these garnets originally crystallized in the perovskite stability zone where they recorded the trace element distribution of perovskitic phases. Subsequent exhumation to shallower depths in the mantle resulted in the retrogressive subsolidus transformation from perovskite to a phase stable at relatively low pressure and temperature (i.e. garnet).

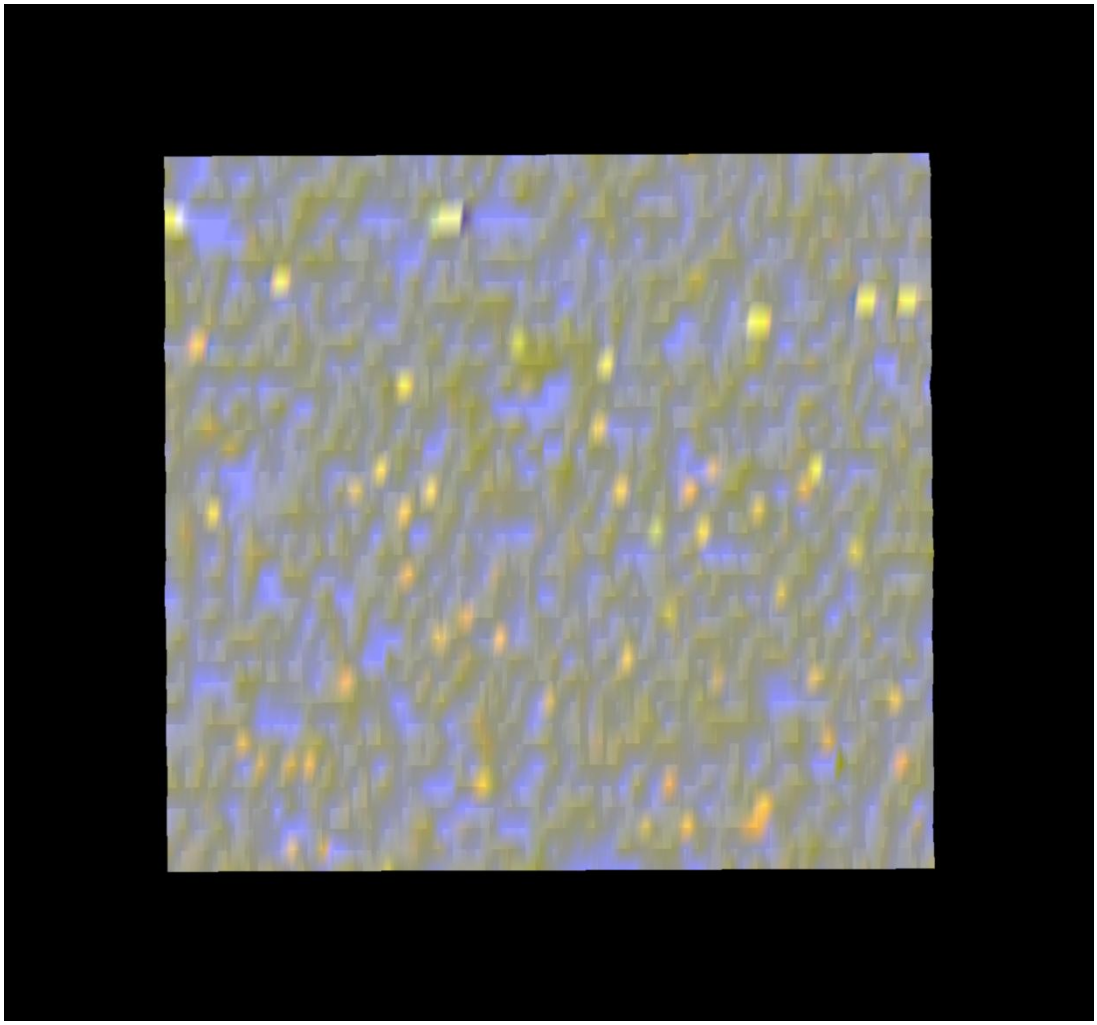

Figure 5.1 shows a compositional map of Gd (red) Sm (green) and Sr (blue) for garnet 1335_28_70. Light spotted areas show localized Gd/Sm enrichment. Note that Sr rich areas (blue) are not coincident with MREE enriched areas.